Title
Three-Dimensional Imaging of the Local Structure of Materials at Atomic Resolution by Electron Tomography

Author
Zhu, Chun

Publication Date
2013

Peer reviewed|Thesis/dissertation

UNIVERSITY OF CALIFORNIA

Los Angeles

Three-Dimensional Imaging of the Local Structure of Materials at Atomic Resolution by Electron Tomography

A dissertation submitted in partial satisfaction of the requirements for the degree Doctor of Philosophy in Physics

by

Chun Zhu

2013

ABSTRACT OF THE DISSERTATION

Three-Dimensional Imaging of the Local Structure of Materials
at Atomic Resolution by Electron Tomography

by

Chun Zhu
Doctor of Philosophy in Physics
University of California, Los Angeles, 2013
Professor Jianwei Miao, Chair

Electron tomography was originally developed in 1968, and has been primarily applied to determine the three-dimensional (3D) structure of biological systems. In the last decade, the application of electron tomography in materials science and nanoscience has revived due to the utilization of scanning transmission electron microscopy (STEM) in the high-angle annular dark-field (HAADF) mode, and a highest resolution of ~1 nm^3 has been achieved. However, improving the resolution from ~1 nm^3 to the atomic level remains a challenging task, which requires new tomographic reconstruction algorithms, better projection alignment methods, state-of-the-art STEM instruments, and more accurate data-acquisition procedures. In this thesis, important progress has been made in all these four areas. First, a novel tomographic method, termed equally sloped tomography (EST), was developed and allows the 3D image reconstruction of tilt series with a limited number projections and a "missing wedge" (*i.e.* specimens cannot usually be tilted beyond $\pm 70^\circ$). Second, an alignment method which can be

used to align the projections of a tilt series at atomic-level resolution was developed based on center of mass. Finally, by using a Titan 80-300 STEM instrument at the California NanoSystems Institute, UCLA, more accurate data acquisition procedures were developed and a number of tomographic tilt series of atomic resolution projections from different nanoparticles have been obtained. With all these combinations, the 3D structure of a 10 nm gold nanoparticle was determined at 2.4 Å resolution, the highest resolution ever achieved in any general tomography method. More recently, this novel electron tomography method has been applied to observe nearly all the atoms in a Pt nanoparticle, and imaged for the first time the 3D core structure of edge and screw dislocations at atomic resolution. Furthermore, through numerical simulations the feasibility of determining the 3D atomic structure of amorphous materials by the Electron Tomography method has been demonstrated.

The dissertation of Chun Zhu is approved.

Brian C. Regan

Kang L. Wang

Jianwei Miao, Committee Chair

University of California, Los Angeles

2013

In dedication to my Mom and Dad.

TABLE OF CONTENTS

LIST OF FIGURES

LIST OF TABLES

ACKNOWLEGMENTS

The most rewarding time of my life is probably the last six years. During my Ph.D studies in the Department of Physics at UCLA, I have experienced high quality education and great research experience. I believe the accomplishment that I am going to achieve would not be possible without the help of people around me. First and foremost, I would like to thank my supervisor, Prof. Jianwei Miao, for mentoring me all the way in electron tomography and nanoscale material research. His guidance, encouragement and support is the basis of the completeness of this thesis research. And I owe my gratitude to my outstanding PhD committee members, Prof. Brian C. Regan, Prof. Stuart Brown, and Prof. Kang Wang, for their valuable suggestions, generous support throughout the dissertation process and honoring me by serving on my committee.

A portion of this work stated in Chapter 3 is a version of the article "Electron tomography at 2.4-ångström resolution" published in *Nature*. I would like to express my thanks to the co-authors for their contributions: M. C. Scott, Chien-Chun Chen, Matthew Mecklenburg, Rui Xu, Peter Ercius, Ulrich Dahmen, B. C. Regan and Jianwei Miao.

A portion of this work stated in Chapter 4 is a version of the article "Three-dimensional imaging of dislocations in a nanoparticle at atomic resolution" published in *Nature*. I would like to express my thanks to the co-authors for their contributions: Chien-Chun Chen, Edward R. White, Chin-Yi Chiu, M. C. Scott, B. C. Regan, Laurence D. Marks, Yu Huang and Jianwei Miao.

A portion of this work stated in Chapter 5 is a version of the article "Towards three-dimensional structural determination of amorphous materials at atomic resolution" published in *Phys. Rev. B.*

I would like to express my thanks to the co-authors for their contributions: Chien-Chun Chen, Jincheng Du, Michael R. Sawaya, M. C. Scott, Peter Ercius, James Ciston and Jianwei Miao.

I would also like to thank my colleagues of the Coherent Imaging Group in department of Physics at UCLA for all the continuous encouragement and help.

Finally, I would like to extend my heartfelt thanks to my parents and my boyfriend Xin. Without their unconditional love and spiritual support I would never be able to complete the Ph.D research study.

VITA

2003-2007	Bachelor of Science in Physics
	University of Science and Technology of China
	Hefei, Anhui, China
2007-2009	Master of Science in Physics
	University of California, Los Angeles
	Los Angeles, California, USA
2008-2011	Teaching Assistant
	Department of Physics
	University of California, Los Angeles
2012-2013	Lead Teaching Assistant
	Department of Physics
	University of California, Los Angeles
2009-2013	Graduate Student Researcher
	Coherent Imaging Group
	Department of Physics and Astronomy
	University of California, Los Angeles

PUBLICATIONS AND PRESENTATIONS

- **Chun Zhu**, Chien-Chun Chen, Jincheng Du, Michael Sawaya, Jianwei Miao. "Towards Three-Dimensional Structural Determination of Amorphous Materials at Atomic Resolution", *Phys. Rev. B.* 88, 100201 (2013).

- Chien-Chun Chen*, **Chun Zhu***, Edward R. White, Chin-Yi Chiu, Mary C. Scott, Chris Regan, Laurence D. Marks, Yu Huang & Jianwei Miao. "Three-dimensional Imaging of Dislocations in Nanoparticles at Atomic Resolution", *Nature* 496, 74-77 (2013). (***Co-first authors**)
  [Highlighted by *Nature* News&Views,"3D imaging of crystal defects", *Nature*, 496, 37-38 (2013)]

- Benjamin P. Fahimian, Yunzhe Zhao, Zhifeng Huang, Russell Fung, Yu Mao, **Chun Zhu**, Maryam Khatonabadi, John J. DeMarco, Stanley J. Osher, Michael F. McNitt-Gray & Jianwei Miao. "Radiation dose reduction in medical x-ray CT via Fourier-based iterative reconstruction", *Med. Phys.*40, 031914 (2013).

- Mary C. Scott, Chien-Chun Chen, Matthew Mecklenburg, **Chun Zhu**, Rui Xu, Peter Ercius, Ulrich Dahmen, Chris Regan & Jianwei Miao. "Electron Tomography at 2.4 Å Resolution", *Nature* 483, 444–447 (2012).
  [Highlighted in *Nature Nanotech.* 7, 275 (2012)]

- **Chun Zhu**, Chien-Chun Chen, Edward R. White, Chin-Yi Chiu, Mary C. Scott, Chris Regan, Laurence D. Marks, Yu Huang & Jianwei Miao, "Three-dimensional Imaging of Dislocations in Nanoparticles at Atomic Resolution", Southern California Society for Microscopy & Microanalysis Full-Day Symposium, UCLA (March, 2013)

- **Chun Zhu**, Mary C. Scott, Chien-Chun Chen, Matthew Mecklenburg, Rui Xu, Peter Ercius, Ulrich Dahmen, Chris. Regan & Jianwei Miao, "Atomic Scale Resolution Electron Tomography: Experimental Procedure and Data Acquisition", Microscopy & Microanalysis 2012 Meeting , Phoenix, AZ (July, 2011).

CHAPTER 1

Introduction

Visualization and analysis of three-dimensional (3D) local structural information at atomic level, which attributes to many characteristic properties of materials such as mechanical, optical, electronic and magnetic behavior, has played an important role in the evolution of modern science and technology. Knowing the knowledge of atomic arrangement inside the material is the prerequisite to further theoretical understanding of the material's properties. For example, intentionally doping introduces impurities into the extremely pure semiconductor and modulates its electrical properties which are essential to the semiconductor performance[1]; Defects inside metals move and absorb energy so that metals will not fracture under a force; the amorphous glass exhibits a unique glass-liquid transition while the origin is still unknown[2]. All these examples illustrate one fact: accurate knowledge of local structure is critical to the understanding of material properties and also their potential applications. Therefore the problem emerges: How can we determine the atomic positions inside materials at atomic resolution?

Nowadays several techniques have been developed to visualize atomic structure of materials, such as X-ray crystallography, high-resolution electron microscopy, scanning tunneling microscopy and atom force microscopy. X-ray crystallography is generally the most widely used method to determine the global-averaged atomic and molecular structure of a crystal[3]. By measuring the angles and intensities of diffracted beams the 3D electron density of the crystals can be produced. The electron density map is then used to determine the mean atomic positions

in the crystals, as well as their chemical bonds and various other information. X-ray crystallography is fundamental in the development of many scientific fields, including physics, material science and biology. However, a local atomic structure is difficult to be determined by applying X-ray scattering to amorphous samples or dislocations due to weak diffracted signals and the average effect. Scanning / Transmission Electron Microscopy (S/TEM) has been revolutionized over the past few years. With the introduction of aberration-corrected electron lenses, both the spatial resolution and the image quality in transmission electron microscopy have been significantly improved and resolution below 0.5 Å has been demonstrated[4-6]. However, TEM images record the exit wave of the electron beam after a specimen, which represents a 2D projection of a 3D object. Interpreting the structure of the 3D object from its 2D projection is an ambiguous process as some information is invariably lost. Scanning tunneling and atomic force microscopy demonstrated resolution on the order of fractions of a nanometer, but atomic structures are only imaged at the surface[7-8]. Although these techniques have made tremendous impacts in material science, biology and nanoscience, they have their own limitations and a general 3D atomic-resolution imaging technique is needed.

In this dissertation, a general electron tomography method for determining 3D local structures at atomic resolution is discussed and demonstrated. Electron tomography (ET) is one of the most promising and rapidly developing techniques to provide detailed 3D information with atomic resolution by a tilt series of projections taken in TEM or STEM[9-12]. Different from electron crystallography, electron tomography does not need to analyze spatial Fourier Transform and thus can resolve the truly unique 3D morphologies. The first application of ET started with three seminal papers in 1968[13-15]. The first paper described the determination of the structure of a biological macromolecule with helical symmetry from a single projection[13]. The second paper

showed the possibility to reconstruct asymmetrical objects from a sufficient number of projections[14]. The third paper demonstrated how to improve signal-to-noise ratio in a projection by averaging re-projected images from a tilt series of images[15]. Since then, the revolution of computation speeds, together with the improvements in mechanical performance of microscopes, makes S/TEM tomography a promising tool for 3D atomic structure revelation. However, the resolution of electron tomography was previously limited to approximately 1nm[11, 12] in 3D for several reasons: First, aligning the projections of a tomographic tilt series to a common axis with atomic level precision is technically challenging. Second, radiation damage limits the number of projections that can be acquired from a single object[16, 17]. Thirdly, specimens cannot usually be tilted beyond ±79°, preventing acquisition of data from the 'missing wedge'[9-12, 18]. Last, vibration of membrane at large tilt angles prevents high quality projections and affects the resolution of reconstruction. To overcome these limitations, I and my colleagues proposed a new method of low-exposure data acquisition of tomographic tilt series combined with a novel alignment approach and an iterative tomographic reconstruction method – Equally Sloped Tomography (EST)[19]. By applying this method, the 3D structure of an approximately 10 nanometer gold nanoparticle was determined at 2.4 Å resolution for the first time[20]. Moreover, we further developed a 3D Fourier filtering method to improve signal-to-noise ratio in the reconstruction and achieved 3D imaging of a number of structural dislocations at atomic resolution inside a multiply twinned platinum nanoparticle[21]. We observed atomic steps at 3D twin boundaries and produced what I believe are the first images of the 3D core structure of edge and screw dislocations at atomic resolution. These dislocations and the atomic steps at the twin boundaries, which appear to be stress-relief mechanisms, are not visible in conventional two-dimensional projections.

Definitely, our ultimate goal is to solve a long-standing problem in the physical sciences: determining the 3D atomic structure of disordered materials. Disordered materials such as glasses are ubiquitous in our daily life. Although the history of glassmaking can be traced back to 3,500 BC in Mesopotamia, the 3D atomic structure of glasses and other disordered materials has defied any direct experimental determination for more than 80 years due to its lack of long-range translational and orientational order. Electron tomography is a very promising technique to overcome this barrier. Through numerical experiments, we demonstrate an electron tomography method for 3D structural determination of amorphous materials at atomic resolution. By combining multislice simulations[22] of an aberration-corrected scanning transmission electron microscope with equally sloped tomography, we have determined the 3D atomic structure of a simulated glass particle, consisting of 334 Si and 668 O atoms, from a tilt series of 55 noisy projections[23]. An atomic model refinement method has been implemented to locate the positions of the Si and O atoms in the reconstruction. This study demonstrates the feasibility of directly imaging 3D atomic structure of disordered materials through electron tomography. We expect that the development of this general method will find applications across several disciplines in the physical sciences.

References

1. Koenraad, P. M. & Flatté, M. E. Single dopants in semiconductors. *Nature Materials* **10**, 91–100 (2011).
2. Debenedetti, P. G. & Stillinger, F. H. Supercooled liquids and the glass transition. *Nature* **410**, 259-267 (2001).
3. Giacovazzo, C. *et al*. *Fundamentals of Crystallography* 2nd edition. (Oxford University Press, USA, 2002).
4. Batson, P. E., Dellby, N. & Krivanek, O. L. Sub-ångstrom resolution using aberration corrected electron optics. *Nature* **418**, 617–620 (2002).
5. Haider, M. *et al*. Electron microscopy image enhanced. *Nature* **392**, 768–769 (1998).
6. Erni, R., Rossell, M. D., Kisielowski, C.& Dahmen, U. Atomic-resolution imaging with a sub-50-pm electron probe. *Phys. Rev. Lett*. **102**, 096101 (2009).
7. Chen, C. J. *Introduction to Scanning Tunneling Microscopy*. 2nd ed. (Oxford University Press, 2008).
8. Giessibl, F. J. Advances in atomic force microscopy. *Rev. Mod. Phys.* **75**, 949-983 (2003).
9. Frank, J. *Electron Tomography* (Plenum, New York, 1992).
10. Lučić, V., Förster, F. & Baumeister, W**.** Structural studies by electron tomography: from cells to molecules. *Annu. Rev. Biochem.* **74**, 833-865 (2005).
11. Midgley, P. A. & Dunin-Borkowski, R. E. Electron tomography and holography in materials science. *Nature Materials* **8**, 271-280 (2009).
12. Arslan, I., Yates, T. J. V., Browning, N. D. & Midgley, P. A. Embedded nanostructures revealed in three dimensions. *Science* **309**, 2195-2198 (2005).

13. de Rosier, D.J. & Klug, A. Reconstruction of three dimensional structures from electron micrographs. *Nature* **217**, 130-134 (1968).
14. Hoppe, W., Langer, R., Knesch, & Poppe, G. C. Protein-Kristallstrukturanalyse mit Elektronenstrahlen. *Naturwissenschaften* **55**, 333-336 (1968).
15. Hart, R.G. Electron microscopy of unstained biological material: the polytropic montage. *Science* **159**, 1464-1467 (1968).
16. Marks, L. D. Experimental studies of small particle structures. *Rep. Prog. Phys*. **57**, 603-649 (1994).
17. Bovin, J. -O., Wallenberg, R. & Smith, D. J. Imaging of atomic clouds outside the surfaces of gold crystals by electron microscopy. *Nature* **317**, 47-49 (1985).
18. Midgley, P. A. & Weyland, M. 3D electron microscopy in the physical sciences: the development of Z-contrast and EFTEM tomography. *Ultramicroscopy* **96**, 413–431 (2003).
19. Miao, J., Föster, F. & Levi, O. Equally sloped tomography with oversampling reconstruction. *Phys. Rev. B* **72**, 052103 (2005).
20. Scott, C. M. *et al.* Electron tomography at 2.4-ångström. *Nature* **483**, 444-447 (2012).
21. Chen, C. C. *et al.* Three-dimensional imaging of dislocations in a nanoparticle at atomic resolution. *Nature* **496**, 74-77 (2013).
22. Kirkland, E. J. *Advanced Computing in Electron Microscopy* (Springer, New York, 2010).
23. Zhu, C. *et al.* Towards three-dimensional structural determination of amorphous materials at atomic resolution. *Phys. Rev. B* **88**, 100201 (2013).

CHAPTER 2

Electron Tomography

2.1 Basic principle

The mathematical foundation underlying tomography was developed by the Austrian mathematician Johann Radon in his work 'On the Determination of Functions from their Integrals along Certain Manifolds'[1]. He rigorously proved the feasibility of reconstructing the object from its tilted series of projections by both Radon Transform and Inverse Radon Transform. The Radon Transform maps a real-space object $f(x, y)$ by its projections, where the projection is considered to be the line integral through $f(x, y)$along all possible lines. The structure of the object $f(x, y)$ is then able to be reconstructed from projections by the inverse form of Radon Transform. All reconstruction algorithms in tomography are the approximations of the Inverse Radon Transform. Given the nature of Radon Transform, a prerequisite known as projection requirement must be fulfilled in order to reconstruct the structure in practice: the intensity recorded in a projection is a monotonic function of the physical property of the object[2]. At the very least, the recorded signal must vary strict monotonically with mass thickness. For example, in X-ray CT, the recorded signal represents the total attenuation of X-rays as it travels in a straight line through the object[3]. At this point, to which extend the images taken in TEM or STEM can be considered as projections will be discussed in Section 2.3.

An alternate way to understand the relation between 2D projections and the 3D object is to use projection-slice theorem or central-slice theorem. The theorem links the projections to the object

by Fourier Transform[4]. It states that the Fourier Transform of the 2D projection is equivalent to the corresponding central slice of the 3D Fourier Transform of the object. A schematic figure representing the reconstruction by Fourier-slice theorem is depicted in Fig. 2.1. If we have sufficiently large number of 2D projections of the object taken over all angles, and then Fourier transform them into Fourier space, the 3D Fourier space can be filled up. So the object is able to be reconstructed by 3D inverse Fourier Transform. This is the most intuitive idea, although many practical issues need to be addressed. For example, experimental data are always sampled at discrete angles and interpolation is required to fill the 'gap' in the Fourier space; the measured data are distributed unevenly in Fourier space, dense around the center but sparse in high-frequency domains; no direct and exact fast Fourier transform exists between the polar and Cartesian grids; etc. These problems will be discussed in the next section.

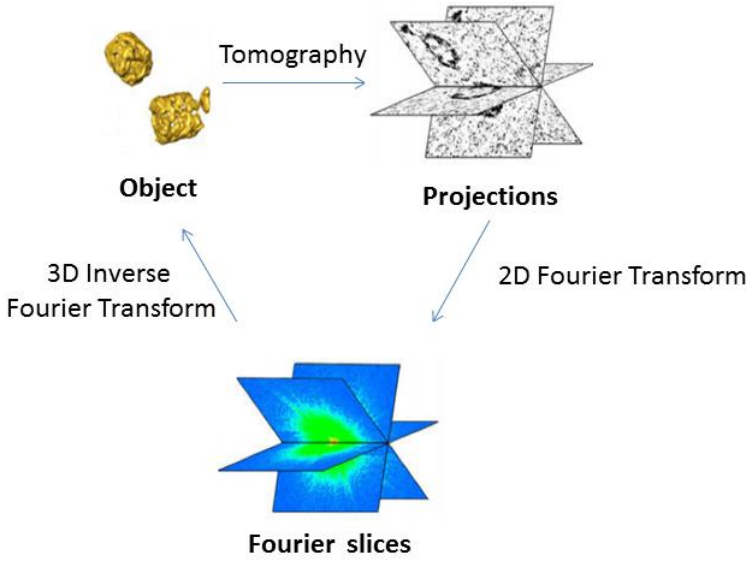

Figure 2.1. Schematic diagram of reconstruction by Fourier-slice theorem.

2.2 Equally Sloped Tomography

Conventional tomography reconstructs a 3D object from a tilt-series of projections with constant angular increments. Since the set of projections are on a polar grid and the object on a Cartesian grid, interpolations have to be performed during the reconstruction process[5, 6]. This is because no direct and exact fast Fourier transform exists between the polar and Cartesian grids[7]. While a number of iterative algorithms exists such as the algebraic reconstruction technique (ART), the simultaneous algebraic reconstruction technique (SART) and the simultaneous iterative reconstruction technique (SIRT)[5, 6, 8], presently the most popular 3D image reconstruction method in electron tomography remains weighted back projection (WBP)[9-11], in which interpolations are performed in real space. In 2005, the EST method was developed to alleviate the difficulties in conventional tomographic reconstruction[12]. For tilt series with a limited number of projections and missing wedge, the EST reconstruction exhibits higher image quality and higher resolution than WBP, ART and SART[13, 14]. In this section, we will present the principle of the EST.

When the projections of a tilt series use equal slope increments, it has been shown that a direct fast Fourier transform, the pseudopolar fast Fourier transform (PPFFT)[15], exists between a pseudopolar grid and a Cartesian grid. Fig. 2.2 shows a pseudopolar grid and the PPFFT. For an $N \times N$ Cartesian grid, the corresponding pseudopolar grid is defined by a set of 2N lines, each line consisting of 2N grid points mapped out on N concentric squares. The 2N lines are subdivided into a horizontal group (in blue) defined by $y = sx$, where s is the slope and$|s| \leq 1$, and a vertical group (in red) defined by $x = sy$, where $|s| \leq 1$; the horizontal and vertical groups are symmetric under the interchange of x and y, and $\Delta s = 2/N$. When these conditions are met,

the PPFFT and its inverse algorithm are mathematically faithful[15]. Note that the PPFFT and its inverse algorithm were originally developed to interpolate tomographic projections from a polar to a Cartesian grid in reciprocal space. The idea of acquiring tomographic tilt-series at equal slope increments and then combining the PPFFT with iterative algorithms for 3D image reconstructions was first suggested in 2005[12].

Compared to other data acquisition approaches, such as the Saxton scheme[16], the EST data acquisition approach is different in that it acquires projections with equal slope increments in order to use the PPFFT. Although the PPFFT and its inverse provide an algebraically faithful way to do the fast Fourier transform between the Cartesian and pseudopolar grids, three difficulties limit its direct application to electron tomography. First, the tilt range has to be from $-90°$ to $90°$. Second, the number of projections in a tilt series needs to be $2N$ for an $N \times N$ object. Third, the grid points past the resolution circle (dashed circle in Fig. 2.2) cannot be experimentally determined. We overcame these limitations by combining the PPFFT with an iterative process[12-14, 17, 18]. Fig. 2.3 shows the schematic layout of the iterative EST method. We first convert the electron micrograph projections to Fourier slices in the pseudopolar grid. As illustrated in Fig. 2.2, the distance between the sampling points on the individual 2N lines of the pseudopolar grid varies from line to line. In order to calculate the Fourier slices from the projections, the fractional Fourier transform is used to vary the output sampling distance of the Fourier slices[19]. By applying the inverse PPFFT, we obtain a 3D image in real space. A 3D support is defined to separate the object from a zero region where the size of the zero region is proportional to the oversampling of the projections[20]. The negative-valued voxels inside the support and the voxel values outside the support are set to zero, and a new3Dimage is obtained. The forward PPFFT is applied to the new image and a set of calculated Fourier slices is obtained.

We then replace the corresponding calculated Fourier slices with the measured ones, and the remaining slices are kept unchanged. The iterative process is then repeated with each iteration monitored by an R factor, defined as the difference between the measured Fourier slices and the calculated ones. . The algorithm is terminated after reaching a maximum number of iterations. Compared to phase retrieval in coherent X-ray/electron diffraction imaging[18, 21-23], the EST method aims to solve the missing data by combining an iteration process with the PPFFT algorithm.

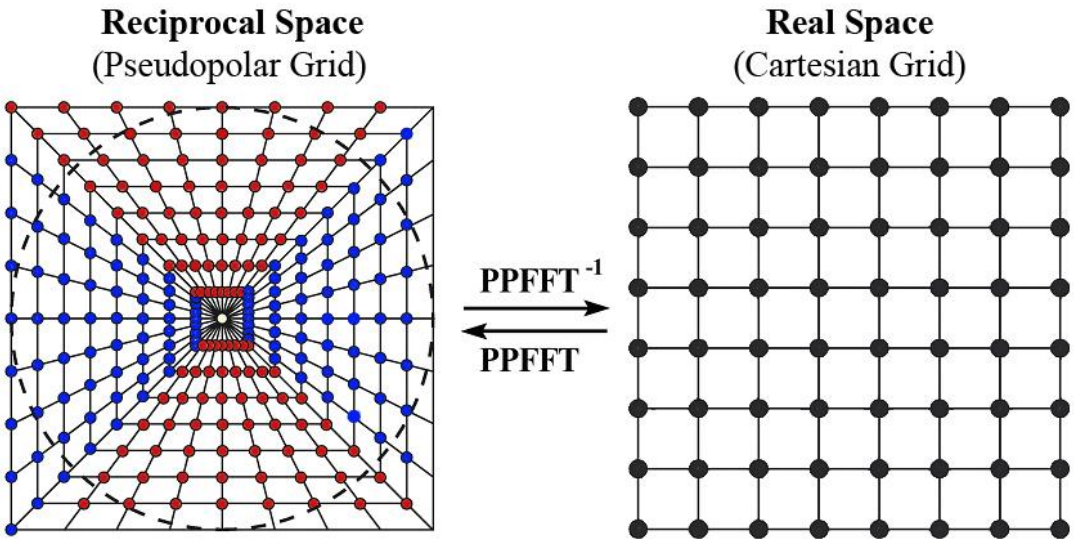

Figure 2.2. Geometrical relationship between a pseudopolar and a Cartesian grid. For an $N \times N$ Cartesian grid, the corresponding pseudopolar grid is defined by a set of $2N$ lines, each line consisting of $2N$ grid points mapped out on N concentric squares (left) with $N = 8$ in this example. The $2N$ lines are subdivided into a horizontal group (in blue) defined by $y = sx$, where $|s| \leq 1$, and a vertical group (in red) defined by $x = sy$, where $|s| \leq 1$. The horizontal and vertical groups are symmetric under the interchange of x and y, and $\Delta s = 2/N$. The dashed circle on the pseudopolar grid represents the resolution circle. The grid points outside of the resolution circle cannot be obtained by applying the Fourier transform to the experimental projections.

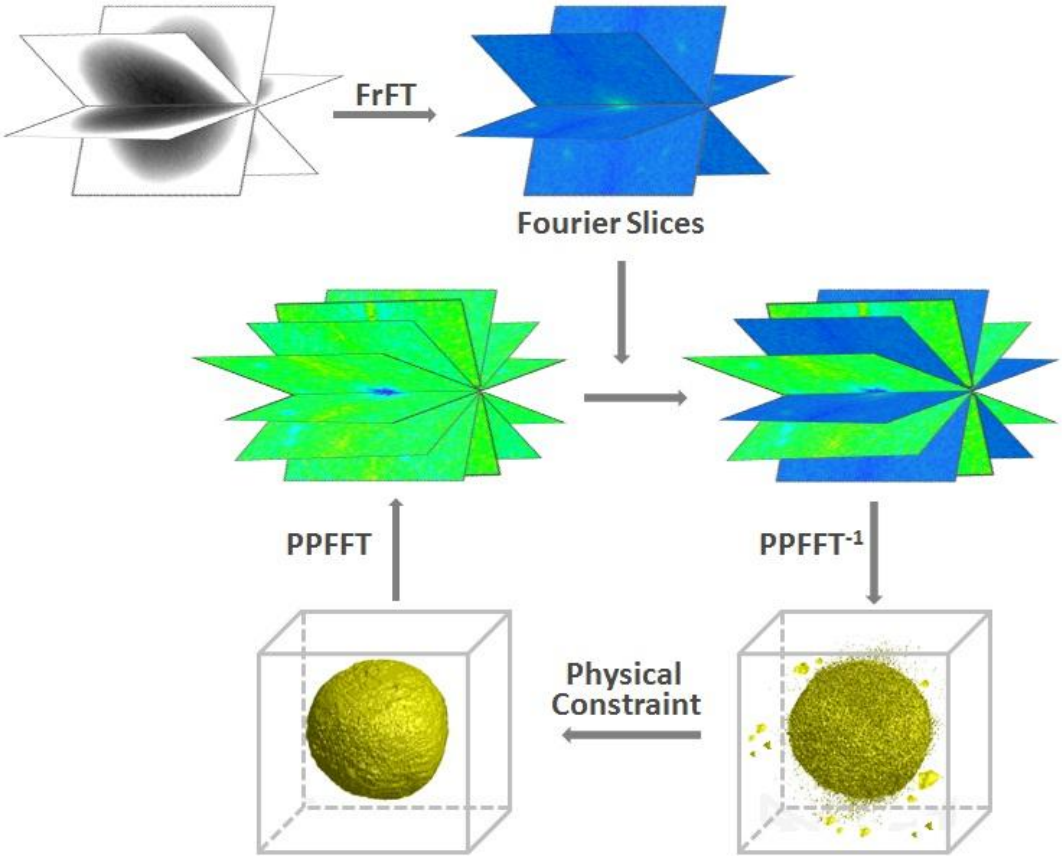

Figure 2.3. Schematic layout of the iterative EST method. The measured projections are first converted to the Fourier slices by the fractional Fourier transform (FrFT)33. The algorithm iterates back and forth between real and reciprocal space using the PPFFT and its inversion (Supplementary Fig. 1). Our recent work has shown that the inverse PPFFT can be replaced by the adjoint PPFFT, allowing for faster convergence without compromising the accuracy19. In real space, the negative-valued voxels inside the support and the voxel values outside the support are set to zero (that is, constraints are applied). In reciprocal space, the corresponding calculated slices are updated with the measured ones (in blue) and the remaining slices (in green) are unchanged. The algorithm is terminated after reaching a maximum number of iterations.

2.3 Imaging modes for electron tomography

Transmission Electron Microscopy (TEM) has been a primary imaging tool for high-resolution characterization of materials. As the name suggested, TEM uses electrons transmitted through the object to form the image. Because of the strong interaction between electrons and matter, electrons can only transmit through very thin material, usually much less than 1 micron. This is the requirement of all specimen studied in TEM. Nowadays, TEM employs a number of different modes to probe the sample. The most commonly used imaging modes are the bright-field TEM, Annual Dark Field Scanning TEM (ADF STEM) and High Angle Annual Dark Field Scanning TEM (HAADF STEM)[24, 25]. Figure 2.4 shows the principle beam paths for both bright-field TEM and ADF STEM imaging modes. In bright-field TEM, the sample is illuminated by parallel electron beams. With higher mass thickness of the sample, more of the incident electrons are scattered away and removed by the objective aperture, resulting in darker image at the thicker part (Fig. 2.4c). Generally the bright-field TEM image satisfies the projection requirement: the intensity of the projection varies monotonically with the mass thickness of the sample. However, if the sample is crystalline and electron beam direction happens to be close to the zone axis, the dominant contrast in the image would be diffraction contrast and the projection requirement is not satisfied. Another violation of the projection requirement in BF TEM is caused by the TEM phase contrast, which is tunable by defocusing. These practical issues limit the use of BF TEM in electron tomography[27, 28].

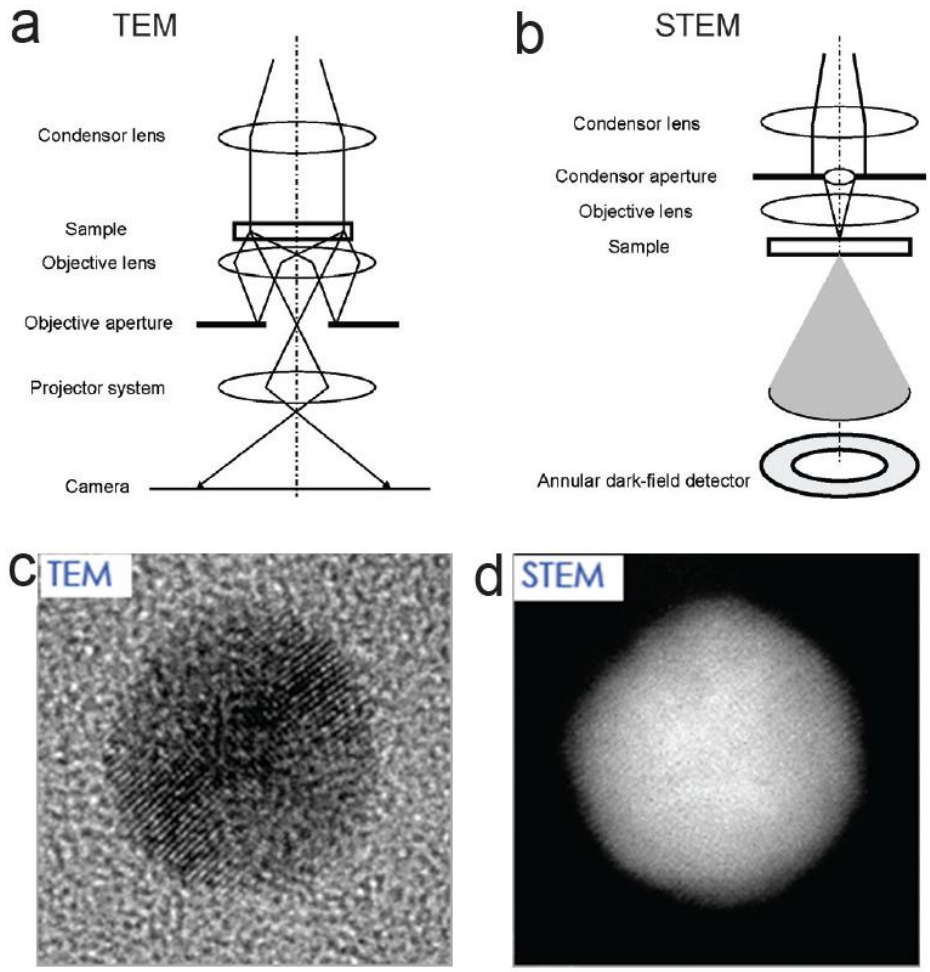

Figure 2.4. Ray diagrams in Bright-Field TEM mode (**a**) and Annual Dark Field STEM mode (**b**). **c** and **d** show the same Au particle imaged in BF TEM and ADF STEM modes. Revised from Ref. [26].

Unlike the conventional TEM, where the specimen is illuminated simultaneously by parallel electron beams, in STEM a focused electron probe is rastered point-by-point across the specimen (Fig. 2.4b). At each point, the incident electrons interact strongly with the specimen, resulting in different kinds of scattered electrons[24], like Figure 2.5 illustrated. In ADF and HAADF STEM

imaging modes, the ring detector collects scattered electrons in certain angle ranges at each rastered point and forms the image (Fig. 2.4b). This imaging scheme leads to brighter images at higher mass thickness, contrary to BF TEM images (Fig. 2.4d). Here HAADF imaging mode only collects elastically scattered electrons with scattered angle larger than 50mrad, while in ADF imaging mode the angular range for collected electrons is usually between 10 to 50 mrad (Fig. 2.6).

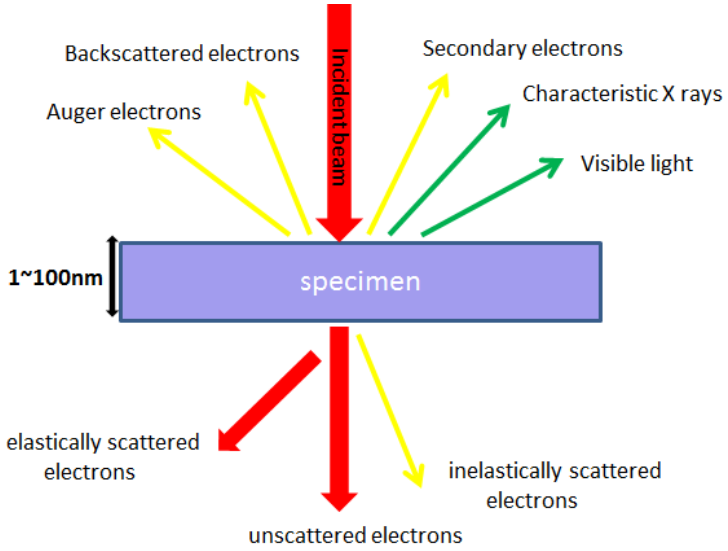

Figure 2.5. Electron-specimen interaction

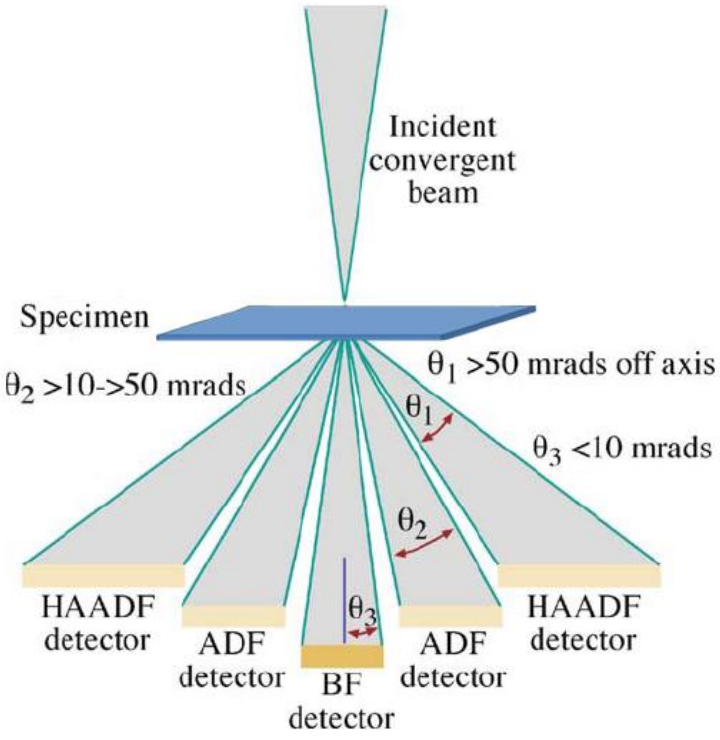

Figure 2.6. Angular ranges of scattered electrons collected by detectors in different STEM imaging modes. Revised from Ref. [24].

HAADF images are also known as Z-contrast images, showing that the recorded intensity is very sensitive to the atomic weight or chemical composition of the sample. Jennycook, *et al*[29] has theoretically proved this point by deriving the scattering cross-section $\sigma_{\theta_1,\theta_2}$ using the integral of Rutherford scattering intensity from θ_1 to θ_2:

$$\sigma_{\theta_1,\theta_2} = \left(\frac{m}{m_0}\right)\frac{Z^2\lambda^4}{4\pi^3 a_0^2}\left(\frac{1}{\theta_1^2+\theta_0^2} - \frac{1}{\theta_2^2+\theta_0^2}\right) \qquad (Eq.\,2.1)$$

Here m is the mass of the incident electron, m_0 is the rest mass of an electron, which is $9.1091 \times 10^{-31}\ kg$, Z is the atomic number, λ is the wavelength of the electron, a_0 is the Bohr radius, which is 0.529 Å; θ_0 is the characteristic angle of elastic scattering.

Suppose n_0 electrons are initially incident on the specimen with thickness t, where t is small compared to the mean free path of the specimen. The number of scattered electrons n collected by the HAADF detector with the inner angle θ_1 and outer angle θ_2 should be

$$n = \sigma_{\theta_1,\theta_2} \cdot n_0 N t \qquad (Eq. 2.2)$$

Here N is the number of atoms per unit volume in the sample.

The two equations above show that the intensity of the HAADF image is almost proportional to the product of Z^2 and sample thickness. Besides, HAADF imaging is almost incoherent because the scattering is almost entirely thermally diffuse[30], thus eliminating diffraction and phase contrast which are the nightmare for BFTEM tomography. The projection requirement is satisfied, leaving HAADF images easy to interpret. All these properties make HAADF STEM ideal for electron tomography[27]. It also provides an indirect way to determine the chemical composition of the sample based on the Z dependence of the signal. The earliest application of HAADF STEM tomography was in the study of heterogeneous catalysts, where the metallic nanoparticles were able to be discriminated from the highly porous siliceous and carbonaceous support by HAADF signals[31]. Since then, HAADF tomography was applied to the study of faceting and crystal morphology[32-35]. It was also widely used in material science and life science to study structures at the interface[36, 37].

Although HAADF imaging has many advantages for tomographic applications, it is not a universal method for all samples. One drawback is the electron channeling effect. For crystalline samples, if the major zone axes coincide with the beam direction, the incident electrons may propagate preferentially down the atom cores, scattering stronger to large angles and make the image much brighter. To avoid channeling effect, we can remove overly bright images from the tilt series. Usually the number is small and removal won't significantly affect the tomographic resolution or fidelity.

At the end of this section I'd like to particularly mention about ADF imaging. Because the normal ADF detector only collects low-angle elastically scattered electrons, sometimes Bragg scattered electrons also fall in the angular range and contribute to the ADF image intensity for crystalline samples, resulting in somewhat unwanted diffraction contrast. However, ADF imaging is still considered as Z-contrast imaging to some extent. Meanwhile, ADF signal is much stronger than HAADF signal, which can significantly improve Signal-to-Noise Ratio (SNR) in the image. So ADF imaging is also a good choice for electron tomography. In the next chapter, the feasibility of high resolution ADF STEM tomography will be demonstrated by numerical simulations, and 2.4 Å resolution is achieved experimentally[38].

2.4 Limitations of electron tomography

Over decades, S/TEM has been revolutionized, leading to the broad applications of electron tomography in the areas of biology, life science and material science[24, 25]. The 3D resolution in electron tomography also significantly increased to approximately $1nm$[39, 40]. However, more difficulties arised to increase the resolution from nanometer scale to atomic scale. In order to

achieve 3D atomic resolution, several limitations must be overcome: missing wedge[39], radiation damage[24] and projection alignment in atomic precision. These limitations are crucial to the ET resolution and deserve some discussion of their origins.

2.4.1 Missing wedge

Missing wedge is a long-lasting problem in electron tomography. Generally speaking, missing wedge means that the tilt angles cannot cover the whole range from $-90°$ to $90°$, resulting in some missing information in the 3D Fourier space, see Figure 2.7. This inherent problem lies in the design of rotation system in transmission electron microscopes. In principle the specimen is tilted about the eucentric axis of the specimen holder rod and should be able to cover the whole angle range, from $-90°$ to $90°$. However the limited space between the objective lens pole pieces and the finite thickness of the specimen holder limits the tilt range to approximate $-70°$ to $70°$. About one third information is lost in the Fourier Space.

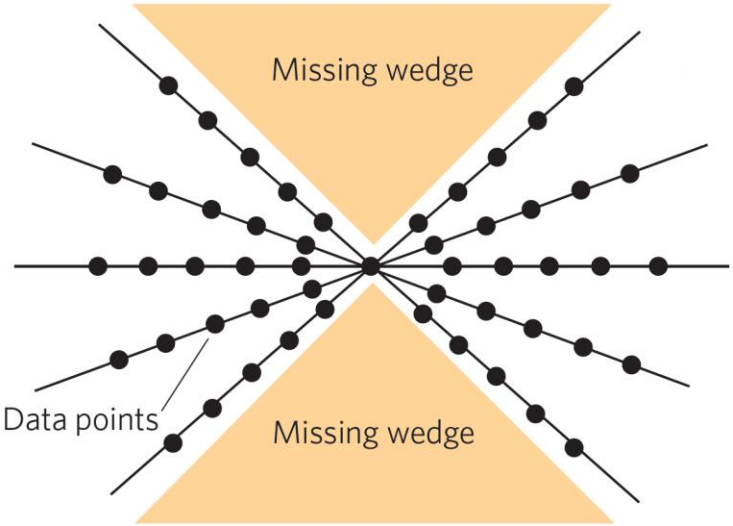

Figure 2.7. Missing wedge in the Fourier space.

Various techniques has been proposed and implemented to reduce the missing wedge. The most popular solution is dual-axis tilting[39], where a second tilt series about an axis perpendicular to the first is recorded and applied in the reconstruction. Furthermore, a unique holder geometry that allows for a 'needle' sample to be rotated $\pm 90°$ was designed for TEAM 1.0 transmission electron microscope in Lawrence Berkeley National Lab, completely eliminating the missing wedge artifacts. In my research, a general tomographic reconstruction method, termed equally sloped tomography (EST) was implemented to alleviate missing wedge effect. A detailed discussion is in Chapter 2.2.

2.4.2 Radiation damage

Electron-specimen interaction provides various useful signals for S/TEM to detect, forming the foundation of all the modern electron microscopes[24]. However, an unfortunate side effect, called radiation damage, is also brought with the interaction. Radiation damage changes the structure and/or the chemistry of the sample and in the worst case, renders the tomographic reconstruction meaningless. In William and Carter's book[24], radiation damage takes one of the three principle forms:

- Radiolysis: Inelastic scattering (mainly electron-electron interactions such as ionization) breaks the chemical bonds of certain materials such as polymers and alkali halides.
- Knock-on damage or sputtering: Knock-on damage is the displacement of atoms from the crystal lattice and creates point defects. If atoms are ejected from the specimen surface we call it sputtering. These processes are ubiquitous if the beam energy (E_0) is high enough.

- Heating: Phonons heat your specimen and heat is a major source of damage to polymers and biological tissue.

The majority of the materials studied in my project were metals. So the primary damage is knock-on collision and sputtering. This damage is directly related to the beam energy. It is also associated with electron dose. In TEM electron dose is defined as the charge density (C/m^2) hitting the specimen. It can be easily converted to the number of electrons per unit area (usually e/nm^2 or $e/\mathring{A}^2$) knowing that $e = 1.6 \times 10^{-19}\ C$. Usually radiation damage is worse with increased beam energy and higher electron dose. Fortunately for most metals the electron threshold energy for displacement of atoms is higher than 400keV[24] - the maximum beam energy for most commercial TEMs. So the electron dose control is the real concern in data acquisition for electron tomography here. Typically, the electron dose in HAADF imaging is much less than TEM images but it is still quite a big number. To make things worse, with the popularization of aberration corrections, more electron currents are focused into even smaller beams, leading to even larger dose exposure. Consequently, the number of projections that can be acquired from a single object has to be limited, affecting the resolution in the tomographic reconstruction. To reduce the radiation dose to the object of interest, a low-dose data acquisition scheme was developed in my research, see Chapter 3.3.3. In addition, the EST is a good solution to this problem. Even with a limited number of projections EST is still able to obtain a reconstruction with high resolution.

A side effect of radiation damage comes in the form of contamination. According to Reimer[25], contamination is a carbon-rich, polymerized film formed by radiation damage of adsorbed hydrocarbon molecules on the specimen surface, and the film grows on electron-irradiated areas

of the specimen by cross-linking. This layer adversely affects the resolution, and can significantly reduce the image quality. For a uniform illumination of a large sample area, the contamination is proportional to the beam current and exposure time. However, when the beam is focused to a probe, contamination builds up much faster[25]. The hydrocarbon originates either from the sample, microscope or the sample holder. Precautions must be taken to avoid contamination, like the special handlings of the specimen, maintaining a clean vacuum system and specimen storage environment, avoiding the frequent use of grease, etc.

2.4.3 Projection alignment

To achieve an atomic scale resolution reconstruction, the projections in a tilt series have to be aligned to a common axis (not necessarily the true tilt axis) with atomic level precision in both the x and y axes, where the y axis represents the tilt axis and the z axis the beam direction. Projection misalignment in electron tomography usually originates in translational movement of the stage when sample is tilted between images to make sure the object of interest is still in the view. Currently, there are two methods used to perform tomographic alignments. The first is based on the cross-correlation between two neighboring projections[9], and the other relies on fiducial markers such as gold beads in the projections[41]. Although both methods have been used in cryo-EM, to our knowledge neither alignment method can achieve atomic-level precision. To overcome this limitation, we have developed a method based on the center of mass, which is able to align the projections of a tilt series at atomic-level accuracy even with noise. See Chapter 3.1 for detailed discussion of the center-of-mass method.

References

1. Radon, J., Ber. Verh. K. Sachs. Ges. Wiss. Leipzig. *Math. Phys. Kl.* **69**, 262 (1917).
2. Hawkes, P. W. *The Electron Microscope as a Structure Projector in Electron Tomogaphy: Three-Dimensional Imaging with the Transmission Electron Microscope.* (ed. Frank, J.), 17-39 Plenum (1992)
3. Buzug, T. *Computed Tomography*. (Springer, 2008).
4. Deans, S. R. *The Radon Transform and Some of Its Applications*. (John Wiley & Sons, New York, 1983).
5. Kak, A. C. & Slaney, M. *Principles of Computerized Tomographic Imaging*. (SIAM, Philadelphia, 2001).
6. Herman, G. T. *Image Reconstruction from Projections: The Fundamentals of Computerized Tomography*. (Academic, New York, 1980).
7. Briggs, W. L. & Henson, V. E. *The DFT: An Owner's Manual for the Discrete Fourier Transform.* (SIAM, Philadelphia, 1995).
8. Natterer, F. & Wubbeling, F. *Mathematical Methods in Image Reconstruction*. (SIAM, Philadelphia, 2001).
9. Frank, J. *Electron Tomography.* (Plenum, New York, 1992).
10. Radermacher, M. Weighted Back-Projection Methods in: Frank, J. (Ed.), *Electron Tomography.* (Plenum, New York, 1992, pp. 91-115).
11. Harauz, G. & van Heel, M. Exact filters for general geometry three dimensional reconstruction. *Optik* **73**, 146-156 (1986).
12. Miao, J., Foster, F. & Levi, O. equally sloped tomography with oversampling reconstruction. *Phy. Rev. B* **72**, 052103 (2005).

13. Lee, E. *et al.* Radiation dose reduction and image enhancement in biological imaging through equally sloped tomography. *J. Struct. Biol.* **164**, 221–227 (2008).

14. Fahimian, B. P., Mao, Y., Cloetens, P. & Miao, J. Low dose X-ray phase-contrast and absorption ct using equally-sloped tomograph. *Phys. Med. Bio.* **55**, 5383-5400 (2010).

15. Averbuch, A., Coifman, R. R., Donoho, D. L., Israeli, M. & Shkolnisky, Y. A framework for discrete integral transformations I—the pseudopolar Fourier transform. *SIAM J. Sci. Comput.* **30**, 785–803 (2008).

16. Saxton, W. O., Baumeister, W. & Hahn, M. Three-dimensional reconstruction of imperfect two-dimensional crystals. *Ultramicroscopy* **13**, 57–70 (1984).

17. Mao, Y., Fahimian, B. P., Osher, S. J. & Miao, J. Development and optimization of regularized tomographic reconstruction algorithms utilizing equally-sloped tomography. *IEEE Trans. Image Process*. **19**, 1259–1268 (2010).

18. Jiang, H. et al. Quantitative 3D imaging of whole, unstained cells by using X-ray diffraction microscopy. *Proc. Natl Acad. Sci. USA* **107**, 11234–11239 (2010).

19. Bailey, D. H. & Swarztrauber, P. N. The fractional Fourier transform and applications. *SIAM Rev*. **33**, 389–404 (1991).

20. Miao, J., Sayre, D. & Chapman, H. N. Phase retrieval from the magnitude of the Fourier transform of non-periodic objects. *J. Opt. Soc. Am. A* **15**, 1662–1669 (1998).

21. Miao, J., Charalambous, P., Kirz, J. & Sayre, D. Extending the methodology of X-ray crystallography to allow imaging of micrometre-sized non-crystalline specimens. *Nature* **400**, 342–344 (1999).

22. Miao, J., Ohsuna, T., Terasaki, O., Hodgson, K. O. & O'Keefe, M. A. Atomic resolution three-dimensional electron diffraction microscopy. *Phys. Rev. Lett*. **89**, 155502 (2002).

23. Zuo, J. M., Vartanyants, I., Gao, M., Zhang, R. & Nagahara, L. A. Atomic resolution imaging of a carbon nanotube from diffraction intensities. *Science* **300**, 1419–1421 (2003).

24. Williams, D. B. & Carter, C. B. *Transmission Electron Microscopy: A Textbook for Materials Science* (2nd Ed., Springer, 2009).

25. Reimer, L. & Kohl, H. *Transmission Electron Microscopy: Physics of Image Formation* (5th Ed., Springer, 2008).

26. Friedrich, H. *Quantitative Electron Tomography for Nanostructured Materials*. Ph.D thesis. (Utrecht University, Nederland, 2009)

27. Midgley, P. A. & Weyland, M. 3D electron microscopy in the physical sciences: the development of Z-contrast and EFTEM tomography. *Ultramicroscopy* **96**, 413-431 (2003).

28. Thomas, J. M. *et al.* The chemical application of high-resolution electron tomography: bright field or dark field? *Angew. Chem., Int. Ed.* **43**, 6745-6747 (2004).

29. Pennycook, S. J., Berger, S. D. & Culberston, R. J. Elemental mapping with elastically scattered electrons. *J. Microscopy*, **144**, 229-249 (1986).

30. Muller, D. A. Structure and bonding at the atomic scale by scanning transmission electron microscopy. *Nature Mater*. **8**, 263-270 (2009)

31. Midgley, P. A., Weyland, M., Thomas, J. M. & Johnson, B. F. G. Z-Contrast tomography: a technique in three-dimensional nanostructural analysis based on Rutherford scattering. *Chem. Commun*. **10**, 907–908 (2001).

32. Weyland, M., Yates, T. J. V., Dunin-Borkowski, R. E., Laffont, L. & Midgley, P. A. Nanoscale analysis of three-dimensional structures by electron tomography. *Scripta Mater*. **55**, 29–33 (2006).

33. Buseck, P. R. *et al*. Magnetite morphology and life on Mars. *Proc. Natl Acad. Sci. USA* **98**, 13490–13495 (2001).

34. De Jong, K. P. & Koster, A. J. Three-dimensional electron microscopy of mesoporous materials - recent strides towards spatial imaging at the nanometer scale. *ChemPhysChem* **3**, 776–780 (2002).

35. Yates, T. J. V. *et al.* Three-dimensional real-space crystallography of MCM-48 mesoporous silica revealed by scanning transmission electron tomography. *Chem. Phys. Lett*. **418**, 540–543 (2006).

36. Porter, A. E. *et al*. Direct imaging of single-walled carbon nanotubes in human cells. *Nature Nanotechnol*. **2**, 713–717 (2007).

37. Midgley, P. A., Weyland, M. & Stegmann, H. in Advanced Tomographic Methods in Materials Research and Engineering (ed. Banhart, J.) 335–373 (Oxford Univ. Press, 2008).

38. Scott, C. M. *et al.* Electron tomography at 2.4-ångström. *Nature* **483**, 444-447 (2012).

39. Midgley, P. A. & Dunin-Borkowski, R. E. Electron tomography and holography in materials science. *Nature Materials* **8**, 271-280 (2009).

40. Arslan, I., Yates, T. J. V., Browning, N. D. & Midgley, P. A. Embedded nanostructures revealed in three dimensions. *Science* **309**, 2195-2198 (2005).

41. Lučić, V., Förster, F. & Baumeister, W. Structural studies by electron tomography: from cells to molecules. *Annu. Rev. Biochem.* **74**, 833-865 (2005).

CHAPTER 3

Determining Three-Dimensional Structure of a Gold Nanoparticle at 2.4-Ångström Resolution by Electron Tomography

Since its introduction in 1968, electron tomography has been primarily used to determine the 3D structure of biological samples [1, 2]. In the past decade, electron tomography has been increasingly applied in materials science and nanoscience through the use of scanning transmission electron microscopy (STEM) [3, 4, 5]. The highest resolution at present achieved by STEM tomography is around 1nm in three dimensions [4, 5], although slightly higher resolution has been obtained in a study of fullerene-like nanostructures with bright-field electron tomography[6]. A general electron tomography method with atomic scale resolution, however, has not been demonstrated for several reasons. First, aligning the projections of a tomographic tilt series to a common axis with atomic level precision is technically challenging. Second, radiation damage limits the number of projections that can be acquired from a single object [7, 8]. Last, specimens cannot usually be tilted beyond ±79°, preventing acquisition of data from the 'missing wedge' [1-5]. Here we demonstrate that these limitations can be overcome or alleviated by applying a novel alignment approach based on center of mass and EST reconstruction method (See section) to a tilt series obtained via annular dark field (ADF)-STEM [9, 10].

Nanoparticles are an important class of materials with properties different from either molecules or bulk solids[7, 11, 12], and nano-gold is among the most widely studied of this class of material due to its broad applications in chemistry, biology, materials science, nanoscience and

nanotechnology[13]. In this study, we imaged gold particles with a diameter of ~10 nm as smaller particles are not as stable under an electron beam[7, 8]. The 3D structure of a gold nanoparticle has been determined with 2.4 Å resolution[14].

3.1 The center-of-mass alignment method

To achieve an atomic scale resolution reconstruction, the projections in a tilt series have to be aligned to a common axis (not necessarily the true tilt axis) with atomic level precision in both the x and y axes, where the y axis represents the tilt axis and the z axis the beam direction. To align the tilt series along the y axis, the projections were first projected onto the y axis and a set of 1D curves was generated. We then chose a 1D curve at $0°$ as a reference, and aligned the remaining curves to the reference. To align the projections along the x axis, we developed a method based on the center of mass. When a 3D object is tilted around the y axis from $0°$ to $360°$, the center-of-mass of the object forms a circle. However, in the special geometry where the center of mass coincides with the origin of the x axis, this circle becomes a point. To determine the center of mass in this special geometry, we projected each 2D projection onto the x axis, chose a pixel as the origin and calculated the center of mass (CM) along the x axis,

$$x_{CM} = \frac{\sum_i x_i \rho(x_i)}{\sum_i \rho(x_i)} \qquad (Eq. 3.1)$$

where $\rho(x_i)$ is the Coulomb potential at position x_i. We then shifted this projection to set x_{CM} as the new origin of the x axis. Through repeating this process for all projections, we aligned the tilt series to the common axis that coincides with the new origin. Later it will be shown that both our

simulation and experimental results indicate that the center-of-mass alignment is a general method and can align the projections of a tilt series at atomic level accuracy, even with relatively high noise and the nonlinear effects (Figure 3.2, 3.4 and 3.9, and Table 3.1).

3.2 Simulations

3.2.1 Multislice simulation

The most important requirement for specimen imaged in S/TEM is that the specimen needs to be thin enough so that multiple scattering is not dominant. However, the electron usually scatters more than once as it travels through the specimen as thin as 10Å. This multiple scattering, also known as dynamic effect, may result in some unwanted signal distortion and make the image not represent the true specimen structures any more. To study how the dynamic effect as well as other nonlinear effects will principally influence the image quality and tomographic reconstruction, multislice simulations are performed on different nanoparticle models as a best way to represent the imaging process in the real S/TEM environment.

The basic idea of multislice simulation is to slice the specimen into many thin layers. The electron wave function is transmitted through one layer, experiencing a phase shift due to the atomic potential, and then propagates to the next layer. In general each layer is independent of other layers. After the electron wave function reaches the exit surface of the specimen, an image is formed by the selected imaging mode and detector conditions. For a detailed explanation, please refer to the book by Kirkland [15]. In this thesis, Kirkland's codes are used in multislice simulations.

3.2.2 Numerical simulations and results

To test the feasibility of achieving a high-resolution tomographic reconstruction by the center-of-mass and EST methods, we conducted numerical simulations on a ~5 nm gold nanoparticle with icosahedral symmetry and a total of 3871 atoms (Figure 3.1a, 3.2a, c, e). A tilt series of 55 projections was obtained from the particle using multislice STEM calculations[14] (energy, 300 keV; spherical aberration, 1.2 mm; illumination semi-angle, 7.98 mrad; defocus, 48.6 nm; detector inner and outer angles, 13 and 78 mrad). To minimize nonlinear intensity contributions caused by dynamical scattering and electron channelling[16], projections along zone axis orientations were avoided. The tilt angles range from $-72.6°$ to $+72.6°$ with equal slope increments. To more closely approximate realistic experimental conditions, several additional modifications were made to generate the simulated data. First, the tilt angles were continuously shifted from $0°$ to $0.5°$ over the process of the tilt series and the magnification of the images was continuously changed from 0 to 0.2%. Second, each projection in the tilt series was arbitrarily shifted along the x and y axes, where the electron beam direction is parallel to the z axis. Last, Poisson noise was added to the projections of the tilt series with a total electron dose of $6.1 \times 10^6 e\,\mathring{A}^{-2}$. Fig. 3.1 shows a linear projection of the model at $0°$ and the corresponding multislice STEM projection. The apparent increase of the atom size in the multislice projection was mainly caused by the nonlinear and diffraction effects in the nanoparticle.

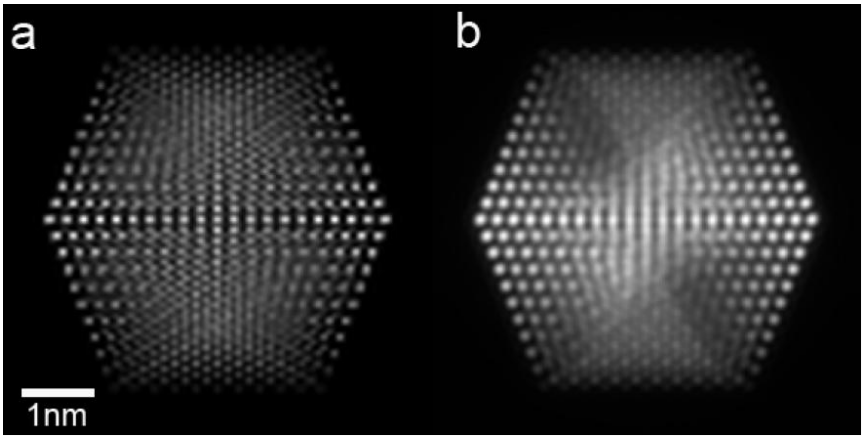

Figure 3.1. Multislice calculations of a ~5 nm simulated Au nanoparticle with ideal icosahedral symmetry and a total of 3871 atoms. **a,** Projected Coulomb potential at tilt angle 0 °. **b,** 0 ° projection calculated by multislice STEM simulations (energy: 300 keV, spherical aberration: 1.2 mm, illumination semi-angle: 7.98 mrad, defocus: 48.6 nm, detector inner and outer angles: 13 and 78 mrad, pixel size: 0.37 Å). The particle was rotated by 1 °each around the horizontal (X) and tilt (Y) axes to avoid the zone axis orientations and reduce the non-linear effects. The resolution in (**b**) was limited by the probe size (~1.5 Å), and the apparent increase of the atom size in the multislice projection was caused by diffraction and dynamical scattering effects in the nanoparticle.

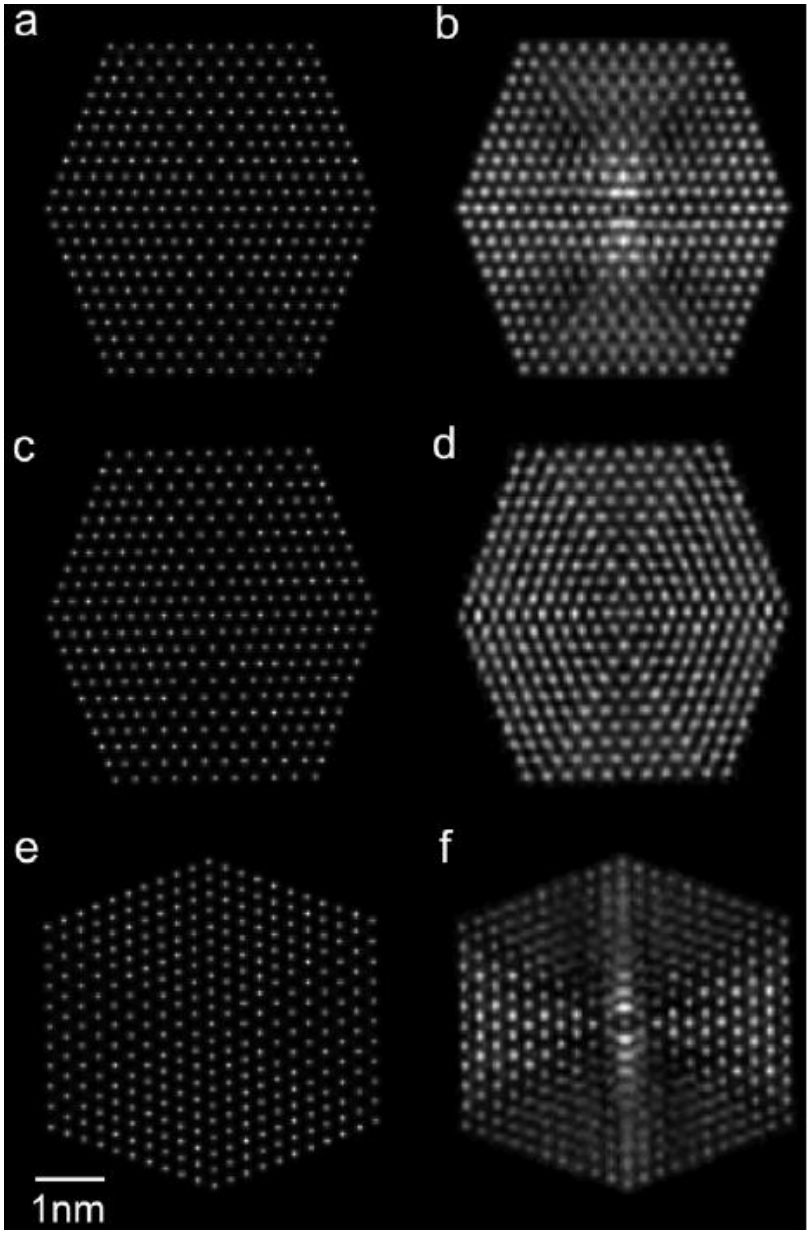

Figure 3.2. EST reconstructions of the simulated Au nanoparticle (~5 nm) from a tilt series, calculated by multislice STEM simulations (energy: 300 keV, spherical aberration: 1.2 mm, illumination semi-angle: 7.98 mrad, defocus: 48.6 nm, detector inner and outer angles: 13 and 78 mrad, pixel size: 0.5 Å). To avoid the zone axis orientations and reduce the non-linear effects, the nanoparticle was rotated by 1 °each around the horizontal (X) and tilt (Y) axes. The tilt series consists of 55 projections with a tilt range of ±72.6 °and equal slope increments. To simulate

experimental conditions, the tilt angles were continuously shifted from 0 °to 0.5 °over the process of the tilt series and the magnification of the images was continuously changed from 0 to 0.2%. The total dose of the tilt series is 6.1×10^{6} e/Å^{2} and Poisson noise was added to each projection. **a, c** and **e,** Three 2.5 Å thick central slices of the Coulomb potential of the simulated nanoparticle in the X-Y, Z-X and Z-Y planes, where the Z-axis is the beam direction. **b, d** and **f**, The corresponding 2.5 Å thick slices in the X-Y, Z-X and Z-Y planes reconstructed from 55 multislice STEM projections. Although the missing wedge problem is not completely solved (the top and bottom parts in (**f**)) and the size of the reconstructed atoms is increased due to the non-linear and diffraction effects, the overall atomic positions and grain boundaries in the 3D reconstruction are consistent with the model.

The 55 projections were aligned to a common tilt axis with the center-of-mass method, and were then reconstructed with the EST algorithm. Figure 3.2b, d, f shows three 2.5-Å-thick central slices of the 3D reconstruction in the $x-y$, $z-x$ and $z-y$ planes. Although the missing wedge problem is not completely solved (the top and bottom parts in Figure 3.2f) and the size of the reconstructed atoms is increased mainly due to the nonlinear and diffraction effects, the atomic positions and grain boundaries in the 3D reconstruction are consistent with the model. The simulation results indicate that the center-of-mass and EST methods can be used to achieve an atomic-scale resolution reconstruction from a tilt series of 55 projections with a missing wedge, nonlinear effects, Poisson noise and experimental errors.

In addition, to investigate the nonlinear effects in the experiment, we simulated a ~10 nm gold particle with icosahedral symmetry and performed multislice STEM calculations on an 11.5-Å-thick slab of the particle. Figure 3.3 shows a linear projection of an 11.5 Å thick slab through the

center of a ~10 nm simulated Au nanoparticle with ideal icosahedral symmetry and a total of 21127 atoms at 0° compared with the corresponding multislice STEM projection. We then calculated a tilt series for a 2.5-Å central slice using the multislice simulations. The tilt series consists of 69 projections with a tilt range of $\pm 72.6°$. Figure 3.4 shows the model and reconstructed slices. The atomic positions and the internal grain boundaries are resolved, except in a very few places owing to the nonlinear effects in the projections.

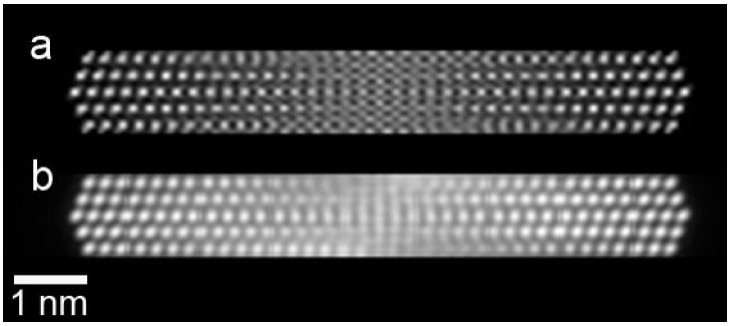

Figure 3.3. Multislice calculations for an 11.5 Å thick slab through the center of a ~10 nm simulated Au nanoparticle with ideal icosahedral symmetry and a total of 21127 atoms. **a,** Projected Coulomb potential at tilt angle 0 °. **b,** 0 °projection calculated by multislice STEM simulations (energy: 300 keV, spherical aberration: 1.2 mm, illumination semi-angle: 7.98 mrad, defocus: 48.6 nm, detector inner and outer angles: 13 and 78 mrad, pixel size: 0.37 Å). The particle was rotated by 1 °each around the horizontal (X) and tilt (Y) axes to avoid the zone axis orientations and reduce the non-linear effects. The resolution in (**b**) was limited by the probe size (~1.5 Å), and the apparent increase of the atom size in the multislice projection was caused by diffraction and dynamical scattering effects in the nanoparticle. As a proof of principle, we simulated only a 11.5 Å thick slab because calculating a full multislice STEM projection for a ~10 nm gold particle would take enormous computational power.

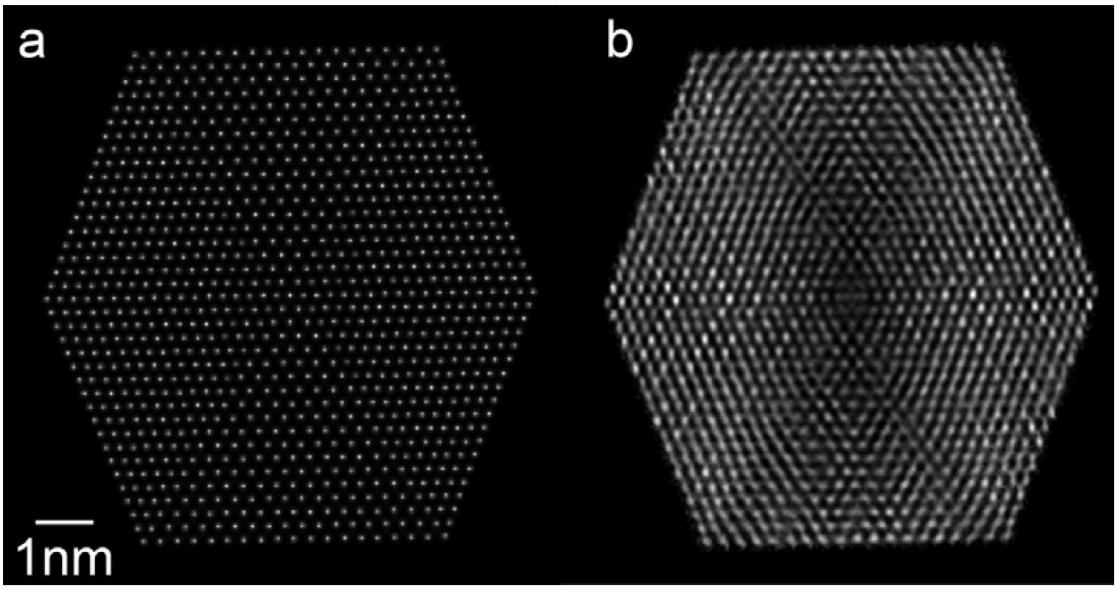

Figure 3.4. EST reconstruction of the ~10 nm simulated Au nanoparticle from a tilt series, calculated by multislice STEM simulations (energy: 300 keV, spherical aberration: 1.2 mm, illumination semi-angle: 7.98 mrad, defocus: 48.6 nm, detector inner and outer angles: 13 and 78 mrad, pixel size: 0.5 Å). The tilt series consists of 69 projections with a tilt range of $\pm 72.6°$ and equal slope increments. To avoid the zone axis orientations and reduce the non-linear effects, the nanoparticle was rotated by $1°$ each around the horizontal (X) and tilt (Y) axes. To simulate experimental conditions, the tilt angles were continuously shifted from $0°$ to $0.5°$ over the process of the tilt series and the magnification of the images was continuously changed from 0 to 0.2%. The total dose of the tilt series is 7.6×10^6 e/Å^2 and Poisson noise was added to each projection. **a,** A 2.5 Å thick central slice of the Coulomb potential in the X-Z plane, where the Z-axis is the beam direction. **b,** A 2.5 Å thick slice in the X-Z plane reconstructed from 69 multislice STEM projections. The atomic positions and the internal grain boundaries are resolved except in very few places (including the origin) owing to the non-linear effects in the projections. As a proof of principle, we only used a 2.5 Å thick slice to illustrate the EST reconstruction.

Calculating a full tilt series for the ~10 nm gold nanoparticle by multislice STEM simulations would take enormous computational power.

3.3 Experiments

3.3.1 Sample preparation

Gold nanoparticle solution with an average particle size of ~10 nm (Ted Pella) was sonicated for ~10min to prevent aggregation. Five-nm-thick Si membranes (TEMwindows.com) were used as the particle substrates in the experiment (Figure 3.5). The thin membrane, with a size of $100 \times 1500\ \mu m$, is supported on a 100- μm-thick Si frame, allowing for a maximum tilt range of $\pm 83°$. To avoid breaking the membrane, a micromanipulator was used to place a small drop of solution onto the outer frame of the Si grid. After gently moving the drop onto the membrane, it was removed and not allowed to dry and leave excessive gold particles and contaminants. The Si grids were cleaned pre-deposition in a Gatan Solarus plasma cleaner (Model 950) for 20 s using a standard H_2/O_2 recipe. To further ensure removal of contaminant sources, the sample holder (Fischione Model 2020) was plasma-cleaned for an hour before data acquisition using the same recipe.

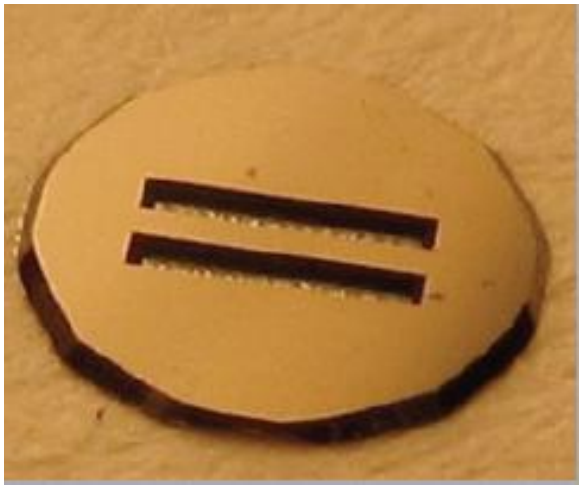

Figure 3.5. Grids for tomography. 5nm thick Si membrane is supported on a 100-μm-thick Si frame.

3.3.2 ADF-STEM

STEM images of gold nanoparticles were acquired on a FEI Titan 80-300 (energy, 300 keV; spherical aberration, 1.2 mm; illumination semi-angle, 7.98 mrad; and defocus, 48.6nm). The 70 pA electron beam was focused to a probe with a 50 mm probe-forming aperture (C2) and rastered over the sample. The scattered electrons were captured by a Fischione Model 3000 ADF detector with angles between 13 mrad and 78 mrad from the optical axis. The use of ADF angles was to improve the signal to noise ratio with a low current electron beam. The effects of nonlinear image intensities and diffraction contrast were carefully determined by multi-slice simulations. The maximum tilt angles were limited by the holder to $\pm 75°$.

3.3.3 Low- exposure acquisition of tomographic tilt series

In order to reduce vibration and drift during data acquisition, the sample holder was allowed to settle for one hour after insertion into the microscope, and also for several minutes after moving to each new angle. Tilt series were acquired by manually changing the angle with equal slope increments. The tilt angles(θ) were determined by[17,18] $\theta = -tan^{-1}[\frac{N+2-2n}{N}]$ for $n = 1, \cdots, N$ and $\theta = \frac{\pi}{2} - tan^{-1}[\frac{3N+2-2n}{N}]$ for $n = N+1, \cdots, 2N$ with N=32 or 64 in this experiment. To focus each projectional image during data acquisition, a nearby particle was used (rather than the particle of interest) to reduce the radiation dose to the particle. By using this low-exposure data acquisition scheme, we have obtained several tomographic tilt series. Figure 3.6 shows the tilt series used in this reconstruction with 69 projections and a tilt range of $\pm 72.6°$. A representative sinogram of the tilt series is shown in Figure 3.7.The probe current was ~70pA with a dwell time of 45 μs per pixel, and the magnification of each projection was 5.2×10^6. Since the pixel size in STEM mode can vary, a calibration image of the particle was taken in TEM mode, and the STEM pixel size was determined to be 0.42Å . The total electron dose of the tilt series was estimated to be $\sim 7.6 \times 10^6 eÅ^{-2}$. Figure 3.8 shows three 0° projections and their Fourier transforms measured during the acquisition of this tilt series to monitor the effects of radiation damage. While some minor shape changes occurred, the crystal lattice structure of the particle remained reasonably consistent throughout the experiment.

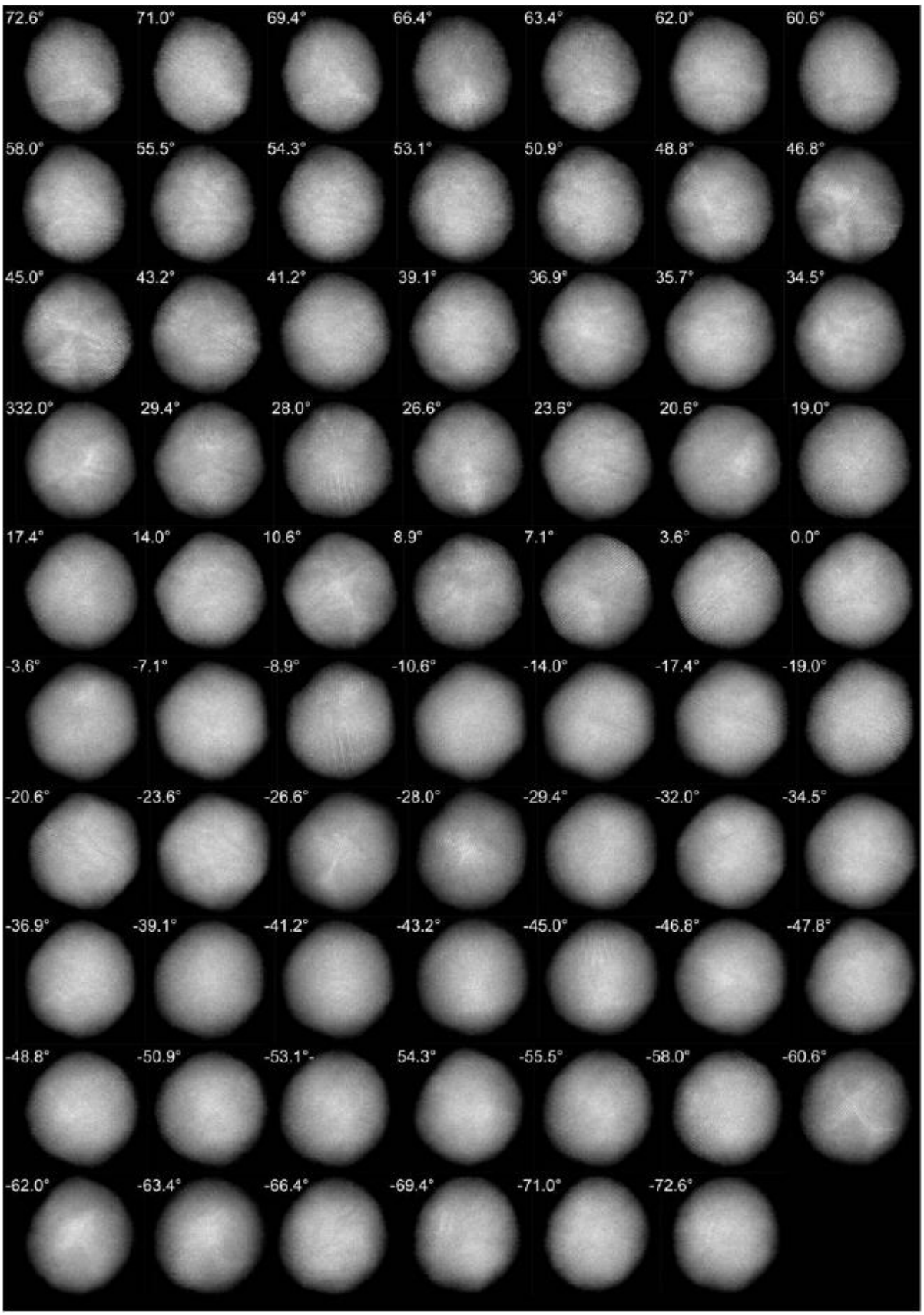
72.6° 71.0° 69.4° 66.4° 63.4° 62.0° 60.6°
58.0° 55.5° 54.3° 53.1° 50.9° 48.8° 46.8°
45.0° 43.2° 41.2° 39.1° 36.9° 35.7° 34.5°
332.0° 29.4° 28.0° 26.6° 23.6° 20.6° 19.0°
17.4° 14.0° 10.6° 8.9° 7.1° 3.6° 0.0°
-3.6° -7.1° -8.9° -10.6° -14.0° -17.4° -19.0°
-20.6° -23.6° -26.6° -28.0° -29.4° -32.0° -34.5°
-36.9° -39.1° -41.2° -43.2° -45.0° -46.8° -47.8°
-48.8° -50.9° -53.1°- 54.3° -55.5° -58.0° -60.6°
-62.0° -63.4° -66.4° -69.4° -71.0° -72.6°

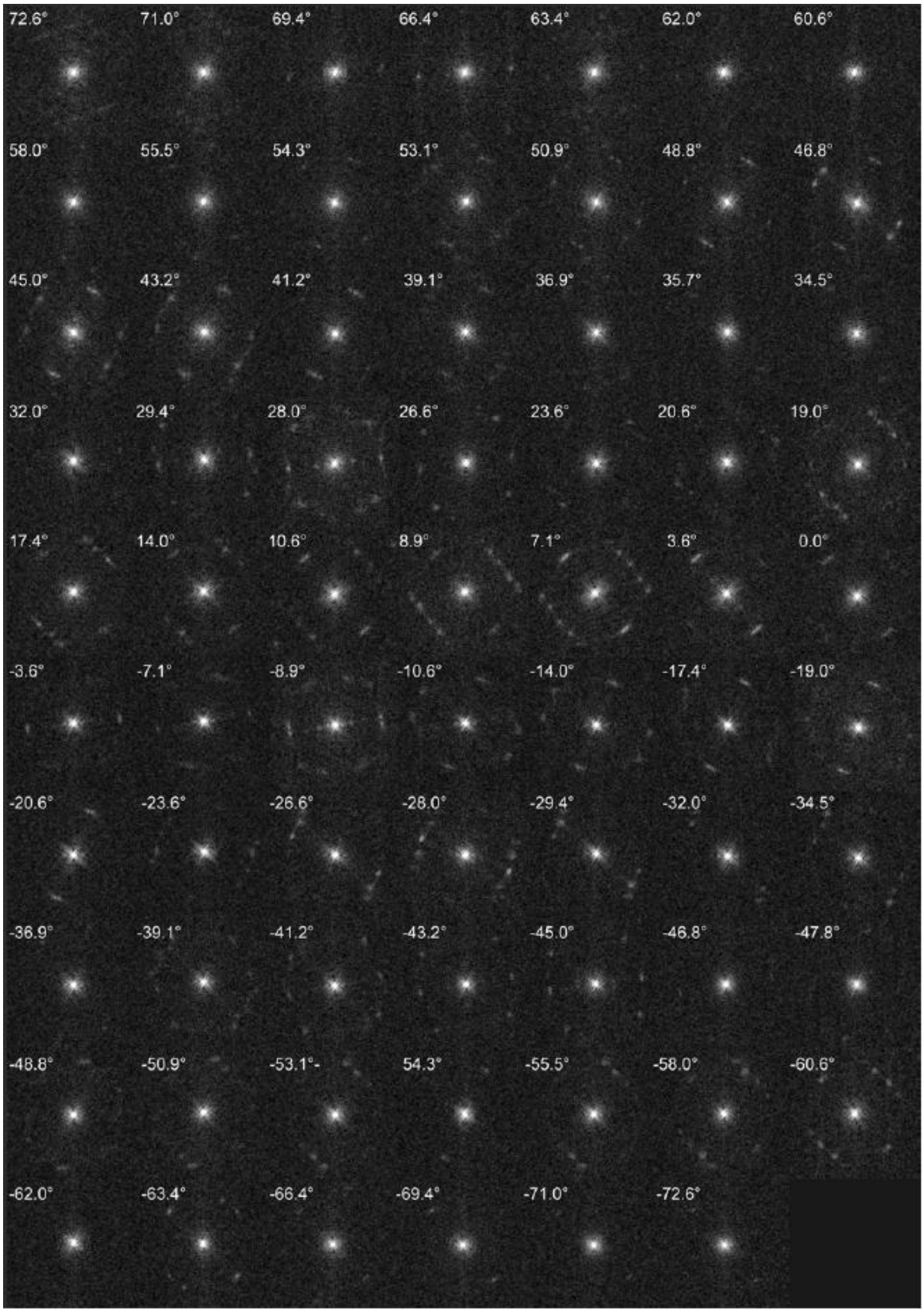
72.6° 71.0° 69.4° 66.4° 63.4° 62.0° 60.6°
58.0° 55.5° 54.3° 53.1° 50.9° 48.8° 46.8°
45.0° 43.2° 41.2° 39.1° 36.9° 35.7° 34.5°
32.0° 29.4° 28.0° 26.6° 23.6° 20.6° 19.0°
17.4° 14.0° 10.6° 8.9° 7.1° 3.6° 0.0°
-3.6° -7.1° -8.9° -10.6° -14.0° -17.4° -19.0°
-20.6° -23.6° -26.6° -28.0° -29.4° -32.0° -34.5°
-36.9° -39.1° -41.2° -43.2° -45.0° -46.8° -47.8°
-48.8° -50.9° -53.1°- 54.3° -55.5° -58.0° -60.6°
-62.0° -63.4° -66.4° -69.4° -71.0° -72.6°

Figure 3.6. Experimental tilt series of 69 projections and their Fourier transforms, acquired from a ~10 nm gold nanoparticle with the tilt axis along the vertical axis. Crystal lattices of the nanoparticle are visible in at least 58 projections. The projections were acquired on an FEI Titan 80-300. The 300 keV electron beam, at spot 8 with a 50 μm C2 aperture, was focused to a probe with a probe current of ~70 pA, and rastered over the nanoparticle with a dwell time of 45 μs per pixel. The scattered electrons were captured by a Fischione Model 3000 ADF detector with angles between 13 and 78 mrad from the optical axis. The electron dose of this tilt series was estimated to be ~7.6×10^6 e/Å^2. Among all the 69 projections, the one at 7.1 °is closest to a zone-axis orientation (about 17 mrad away from the 2-fold zone axis).

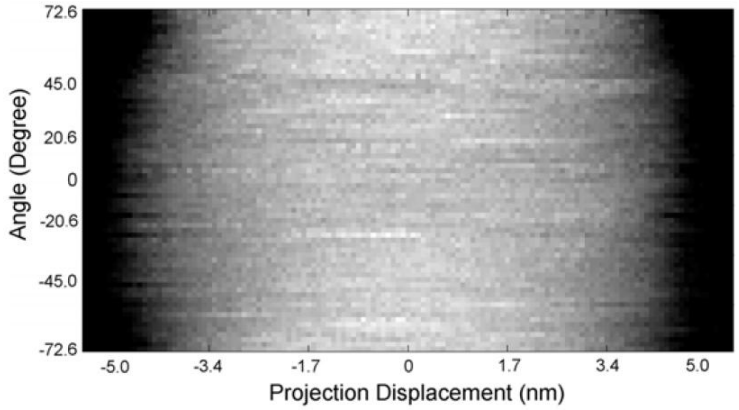

Figure 3.7. A representative sinogram for the experimental tilt series of 69 projections acquired from the ~10 nm Au nanoparticle. The X-axis shows the distance to the tilt axis and the Y-axis shows the tilt angles for the projections. Unlike conventional tomography, the angular increments in EST are not constant. Thus the angles along the Y-axis are not equally distributed and smooth transitions between different angles are not expected. The sudden horizontal intensity jumps are mainly due to the lattice structure in the projections, and the rough edge is likely caused by the background and noise in the projections.

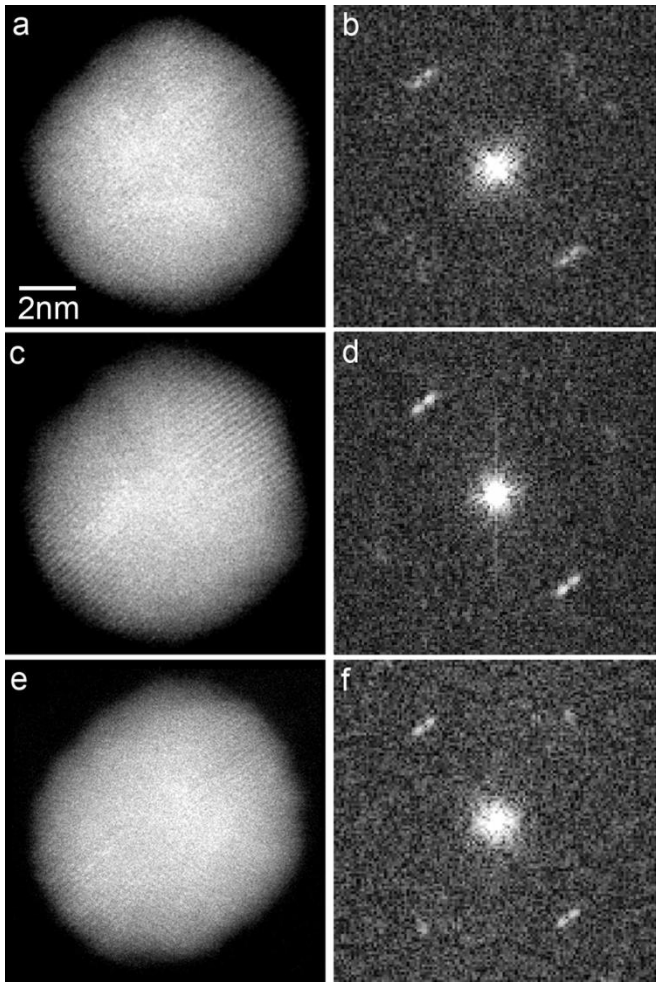

Figure 3.8. Three 0 °projections (**a**,**c**,**e**) and their Fourier transforms (**b**,**d**,**f**) measured during the acquisition of the tilt series (Figure 3.6) to monitor the effects of radiation damage. Although minor shape changes occurred, the overall crystal lattice structure of the gold nanoparticle remained consistent throughout the experiment. The minor shape change may contribute to a small degree of uncertainty in the overall shape of the reconstructed nanoparticle.

3.4 Methods for data analysis

3.4.1 Post Data Analysis

In order to apply the EST method, the background surrounding the nanoparticle in each projection has to be subtracted. To systematically eliminate the background, we first projected all the projections onto the tilt axis and obtained a set of 1D curves. We then determined the optimal cut-off value for background subtraction in each projection by maximizing the cross-correlation among these 1D curves. After background subtraction, we binned 2×2 pixels into1 pixel, which was used to enhance the signal to noise ratio in the projections and improve the EST reconstruction. The background subtracted and binned projections with pixel size of 0.84Å were aligned using the centre-of-mass approach and reconstructed with the EST method.

3.4.2 Mathematical implementation of the EST method

EST method begins with padding each projection with zeros (that is, embedding the experimental projection into a larger array of zeros) and calculating its oversampled Fourier slice on a pseudopolar grid (blue planes in Figure 2.3) using the fractional Fourier transform (FrFT)[19].The FrFt varies the output sampling distance of the Fourier transform and is defined in the 1D case by

$$F_{\alpha}(k) = \sum_{x=-N}^{N-1} f\,(x) \exp\left(-\frac{i\pi\alpha kx}{N}\right) \qquad (Eq.\,3.2)$$

Eq. (1) is equivalent to the standard 1D FFT but with an extra factor of α in the exponent. By choosing an appropriate value for α, the projection data can be mapped on to the grid points of

any line on the pseudopolar grid. The oversampling concept (that is, sampling the Fourier slice at a frequency finer than the Nyquist interval)[20] has been widely used to solve the phase problem in coherent diffraction imaging[21-24]. In the EST method, oversampling does not provide extra information about the object, but allows the use of iterative algorithms to extract the correlated information within the projections. In the first iteration, the grid points outside the resolution circle (dashed line in Fig. 2.2 left) and on the missing projections is set to zero. We also note that the reconstruction may be improved by supplying each missing projection with the average of its two neighboring projections as an initial input. Once this preprocessing step has occurred, the algorithm iterates back and forth between real and Fourier space, shown in Figure 2.3. The j[th] iteration consists of the following 5 steps:

i) Apply the inverse PPFFT to the Fourier-space slices $F_j(\vec{k})$, and obtain a real-space image, $f_j(\vec{r})$. Our recent work has shown that the inverse PPFFT can be replaced by the adjoint PPFFT, allowing for faster convergence without compromising the accuracy [19].

ii) A support (S) is determined based on the oversampling of the projections34.Outside the support, $f_j(\vec{r})$ is set to zero and inside the support, the negative values of $f_j(\vec{r})$ are set to zero. A new image, $f_j'(\vec{r})$, is obtained,

$$f_j'(\vec{r}) = \begin{cases} 0 & \text{if } \vec{r} \notin S \text{ or } f_j(\vec{r}) < 0 \\ f_j(\vec{r}) & \text{if } \vec{r} \in S \text{ or } f_j(\vec{r}) \geq 0 \end{cases} \qquad (Eq.\,3.3)$$

iii) Apply the PPFFT to $f_j'(\vec{r})$ and obtain new Fourier slices, $F_j'(\vec{k})$.

iv) Calculate the Fourier slices for the (j+1)[th] iteration,

$$F_{j+1}(\vec{k}) = \begin{cases} F_j'^{\emptyset}(\vec{k}) & \text{for the missing projection angles } (\emptyset) \\ F_m^{\theta}(\vec{k}) & \text{for the measured projection angles } (\theta) \end{cases} \qquad (Eq.\,3.4)$$

Where $F_j^{'\emptyset}(\vec{k})$ and $F_m^{\theta}(\vec{k})$ represent the missing and measured Fourier slices, and $\emptyset \cup \theta$ forms a complete set of angles on the pseudopolar grid.

v) An R_{recip} is calculated,

$$R_{recip} = \frac{\sum \left| |F_m^{\theta}(\vec{k})| - |F_j^{'\theta}(\vec{k})| \right|}{\sum |F_m^{\theta}(\vec{k})|} \qquad (Eq. 3.5)$$

Where $F_m^{\theta}(\vec{k})$ and $F_j^{'\theta}(\vec{k})$ represent the measured and jth calculated Fourier slices.

In our reconstructions, the algorithm is terminated after reaching a maximum number of iterations. To quantify the method, we project back the final 3D reconstruction to calculate a series of projections, which are quantified by an R_{real},

$$R_{real} = \frac{\sum \left| |f_c^i(x,y)| - |f_m^i(x,y)| \right|}{\sum |f_m^i(x,y)|} \qquad (Eq. 3.6)$$

where $f_c^i(x,y)$ and $f_m^i(x,y)$ represent the calculated and measured projections in real space at tilt angle i.

3.4.3 Identification of the major 3D grains inside the nanoparticle

The following procedures were used to determine the major 3D grains inside the gold nanoparticle. (1) Apply the 3D Fourier transform to the reconstructed nanoparticle and identify the Bragg peaks corresponding to a major grain. (2) Use small spheres with soft edges to select these Bragg peaks and set other values to zero. (3) Apply the 3D inverse Fourier transform to the selected Bragg peaks and obtain a 3D image. (4) Convolve the 3D image with a Gaussian filter and choose a cut-off value to determine the 3D shape of the grain. (5) Use the 3D shape to

identify the corresponding 3D grain in the reconstructed nanoparticle. (6) Repeat steps 1–5 to determine other major grains.

3.5 Results and discussions

After aligning the experimental tilt series of projections acquired from gold nanoparticles with CM method, EST was performed to reconstruct the 3D structure. To examine the quality of the reconstruction, we calculated 69 projections from the final 3D structure and found the average normalized discrepancy with the measured projections to be 6.7% (Mathematical implementation of the EST method and Table 3.1). Representatives measured and calculated projections at different particle orientations are shown in Figure 3.9 and Figure 3.10. While minor shape changes occurred in few areas, the overall shape and lattice structure agree well between measured and calculated projections. To more rigorously examine the accuracy of the reconstruction, an EST reconstruction was performed from 68 experimental projections by removing the 7.1 °projection. The 3D reconstruction was then projected back to calculate the projection at 7.1 °, which is reasonably consistent with the experimentally measured one (Figure 3.11).

Angles (°)	72.6	71.0	69.4	66.4	63.4	62.0	60.6
R_{real} (%)	7.1	6.2	6.4	10.8	10.2	5.9	6.2
Angles (°)	58.0	55.5	54.3	53.1	50.9	48.8	46.8
R_{real} (%)	5.8	6.0	6.5	6.1	6.5	6.8	11.6
Angles (°)	45.0	43.2	41.2	39.1	36.9	35.7	34.5
R_{real} (%)	14.0	11.4	8.0	5.8	6.1	6.9	6.4
Angles (°)	32.0	29.4	28.0	26.6	23.6	20.6	19.0
R_{real} (%)	7.3	6.5	6.8	6.6	5.7	7.6	5.9
Angles (°)	17.4	14.0	10.6	8.9	7.1	3.6	0
R_{real} (%)	5.6	5.0	7.4	7.7	10.5	5.7	5.3
Angles (°)	-3.6	-7.1	-8.9	-10.6	-14.0	-17.4	-19.0
R_{real} (%)	5.8	5.7	6.9	5.1	5.5	5.3	6.9
Angles (°)	-20.6	-23.6	-26.6	-28.0	-29.4	-32.0	-34.5
R_{real} (%)	5.4	6.1	6.9	8.6	5.6	5.0	4.8
Angles (°)	-36.9	-39.1	-41.2	-43.2	-45.0	-46.8	-47.8
R_{real} (%)	4.7	4.9	5.9	6.1	5.6	6.5	6.0
Angles (°)	-48.8	-50.9	-53.1	-54.3	-55.5	-58.0	-60.6
R_{real} (%)	7.4	6.7	5.9	6.5	6.0	6.6	7.2
Angles (°)	-62.0	-63.4	-66.4	-69.4	-71.0	-72.6	Average
R_{real} (%)	6.9	7.8	5.6	6.6	5.5	6.6	6.7

Table 3.1. To examine the reconstruction quality, we projected back the reconstructed 3D structure at the same experimental tilt angles to calculate 69 projections. An R_{real} (*Eq*.3.6) was calculated for each tilt angle. The average R_{real} for all tilt angles is 6.7%.

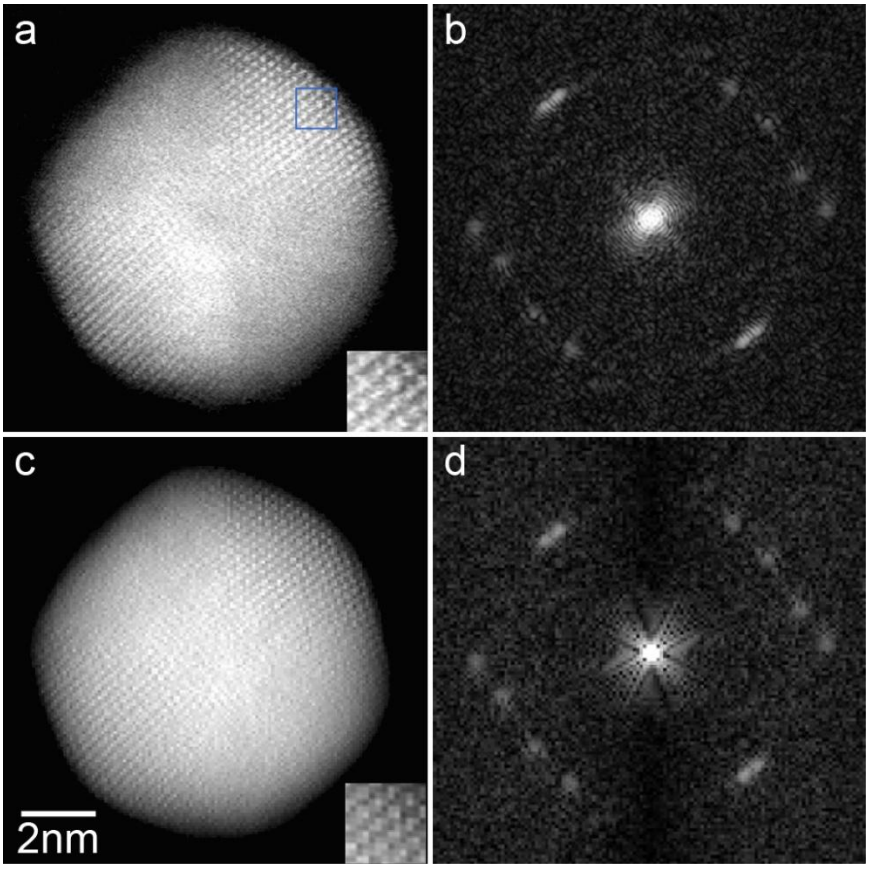

Figure 3.9. Evaluation of the 3D reconstruction quality. **a**-**d**, Representative measured (**a**) and calculated (**c**) projections and their Fourier transforms (respectively **b**, **d**) at tilt angle 7.1 °. Insets in **a** and **c** show the projected atomic positions inside the blue square in the main panel. The overall shape of the nanoparticle and the location of the Bragg peaks agree well, indicating a good quality 3D reconstruction.

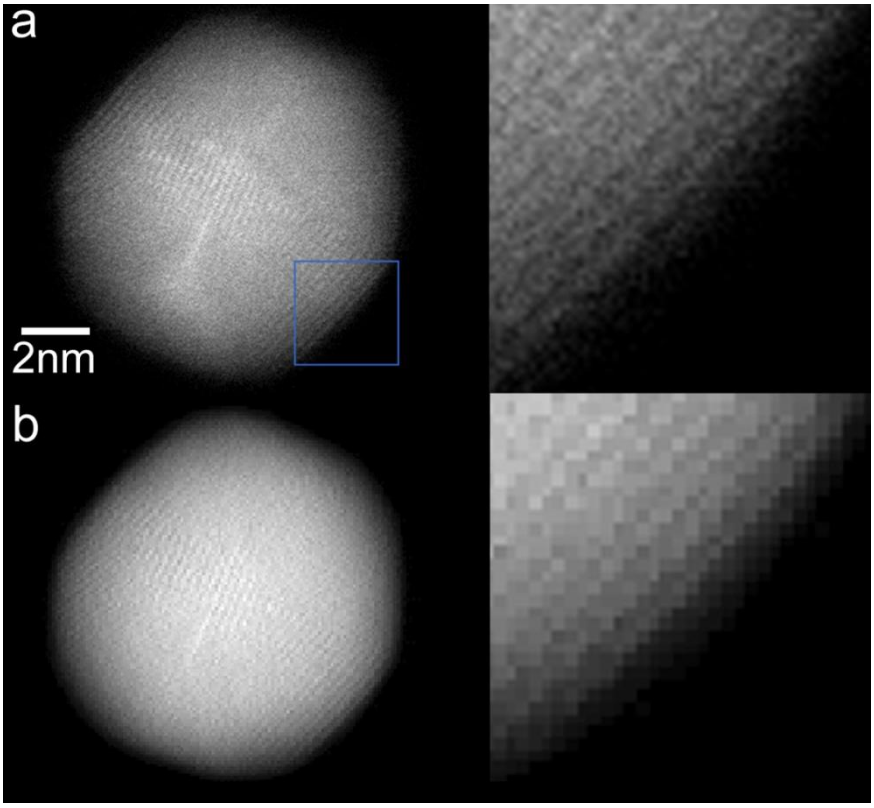

Figure 3.10. Measured (**a**) and calculated (**b**) projections at -26.6 °for the ~10 nm gold nanoparticle. The calculated projection was re-projected from the 3D reconstruction of 69 projections. The zoomed images indicate that, while there are some very minor differences between the two projections, the overall shape and lattice structure agree well.

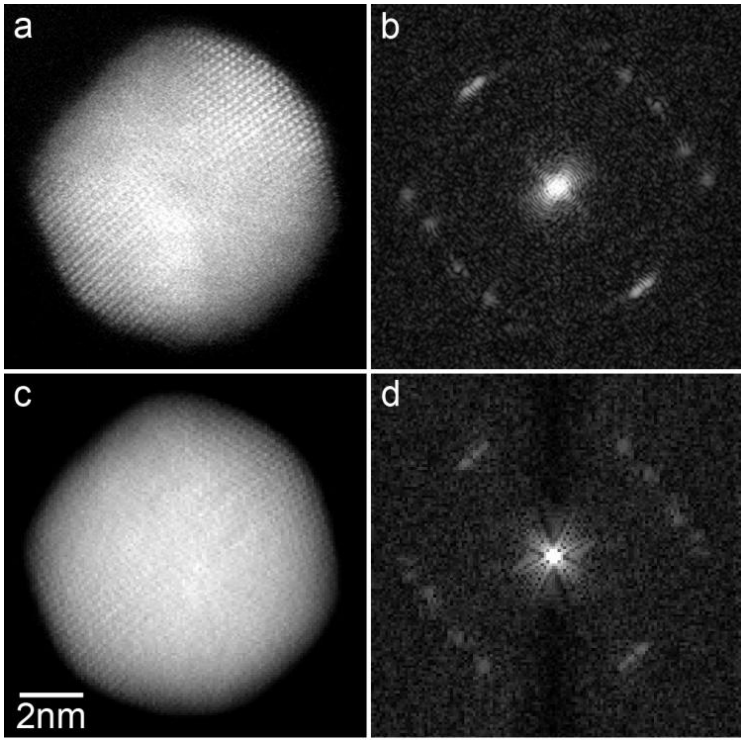

Figure 3.11. Measured (**a**) and calculated (**c**) projections and their Fourier transforms (**b, d**) at 7.1 °, where the calculated projection (**b**) was re-projected from a 3D reconstruction without using the measured projection (**a**). While the contrast of the lattice fringes and the Bragg peak intensity are slightly different between (**a**), (**b**) and (**c**), (**d**), the overall shape and the lattice structure are in good agreement. In the reconstruction, the average of two neighboring projections at 3.6 °and 8.9 °was input as an initial guess for the projection at 7.1 °, but was not used as a constraint in each iteration.

To estimate the resolution achieved in the reconstruction, we chose a 3.36 Å thick central slice in the XY plane. Figure 3.12a and b show the slice and its Fourier transform in which the distance between two neighboring atom columns and the location of the Bragg peaks indicate that a resolution of 2.4 Å was achieved in the X and Y directions. To estimate the resolution along the

Z-axis (beam direction), we selected a 3.36 Å thick slice with the horizontal axis along the Z-axis (Figure 3.12c and d). The resolution close to the Z-axis was determined to be 2.4 Å. Individual atoms are visible in some regions of the slices, but not all atoms can be identified in the slices. Figure 3.13 shows two 3.36 Å thick slices in a different orientation, exhibiting crystal lattice structure not visible in Figure 3.12. The apparent flattening of the particle along the beam axis was also observed in the 3D reconstructions (Figure 3.12), and was likely caused by the interaction between the nanoparticle and the Si substrate.

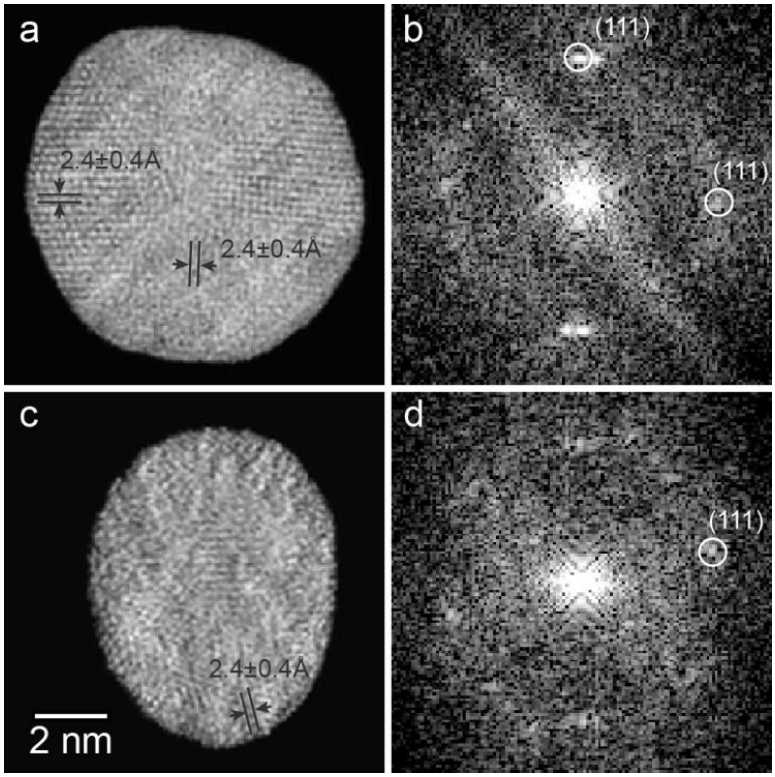

Figure 3.12. Estimation of the 3D resolution of the reconstruction of the gold nanoparticle. **a**, **b**, A-3.36-Å thick central slice in the *x*–*y* plane (**a**) and its Fourier transform (**b**), indicating that a resolution of 2.4Å corresponding to the gold (111) lattice was achieved along the x and y axes. **c**,

d, A 3.36-Å-thick slice in the *z–y* plane (**c**) and its Fourier transform (**d**) where the horizontal axis is along the z axis (beam direction). The resolution in the z axis was estimated to be 2.4Å. Individual atoms are visible in some regions of the slices, but not all atoms can be identified in the slices.

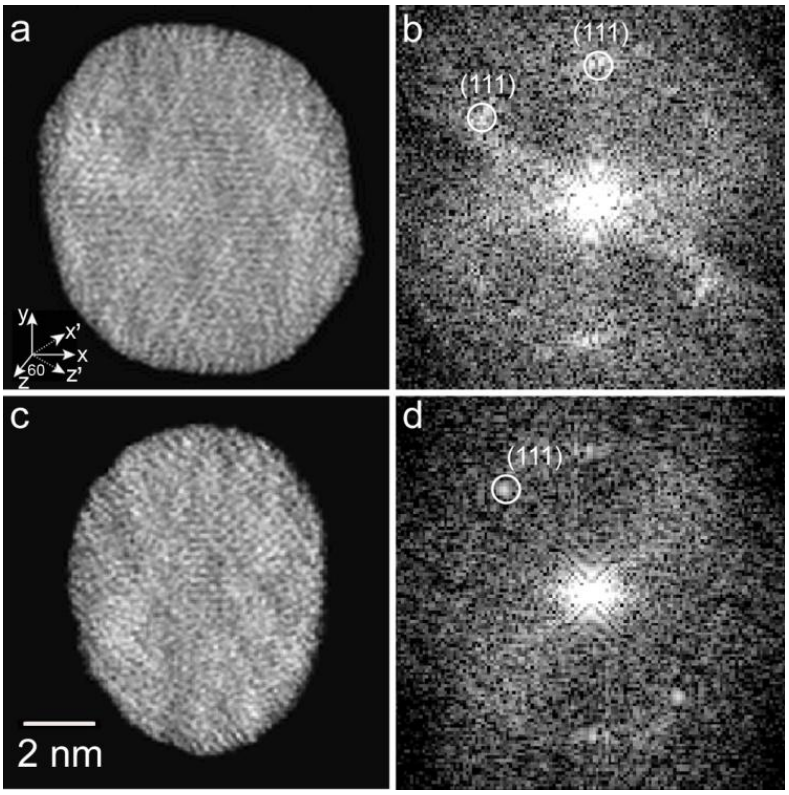

Figure 3.13. **a** and **b**, A 3.36 Å slice in the X′-Y plane and its Fourier transform, obtained from the experimentally reconstructed Au nanoparticle. **c** and **d**, A 3.36 Å slice in the *Z′-Y* plane and its Fourier transform. The inset shows the direction of the X, Y, Z and X′, and *Z′* axes, and the angle between planes Z-Y and *Z′*-Y is ~60 °, whereas the slices shown in Figure 3.12a and c are in the X-Y and Z-Y planes, respectively. The crystal lattice structure is visible in the top and bottom areas in (**a**) and the top-right area in (**c**), but is not present in Figure 3.12a and c.

To visualize the internal structure and the morphology of the gold nanoparticle, we generated 3D volume and iso-surface renderings of the reconstruction, in which both surface and internal lattice structures are visible. Figure 3.14a and b show volume renderings of the nanoparticle and their Fourier transforms (insets) at the 2- and 3-fold symmetry orientations. The corresponding iso-surface renderings at the same orientations are shown in Figure 3.14c and d. The overall 3D shape and facets of the nanoparticle are consistent with an icosahedron (insets in Figure 3.14c and d). To identify internal 3D grains, we applied the 3D Fourier transform to the reconstruction. By identifying the Bragg peaks of each major grain and applying the 3D inverse Fourier transform to the selected Bragg peaks, we determined four major 3D grains inside the gold nanoparticle (Section 3.4.3). Figure 3.15 show a volume rendering of the four 3D grains at atomic scale resolution, in which grains 1, 2 and grains 3, 4 are related by mirror-reflection across the horizontal interfaces marked by dotted lines. The angle enclosed by close-packed planes across these interfaces was measured to be 69.9 °±0.8 °between grains 1 and 2, and 71.3 °±0.8 °between grains 3 and 4, both of which are consistent with the angle for an fcc twin boundary (70.53 °). By applying the same method to some other Bragg peaks, we identified 3D grains in the top and bottom parts of the particle (Figure 3.16). The surface morphology (facets) and the internal atomic structures (grains) suggest that this is a distorted icosahedral multiply-twinned particle, typically found for nano-gold in the size range above 10 nm[25].

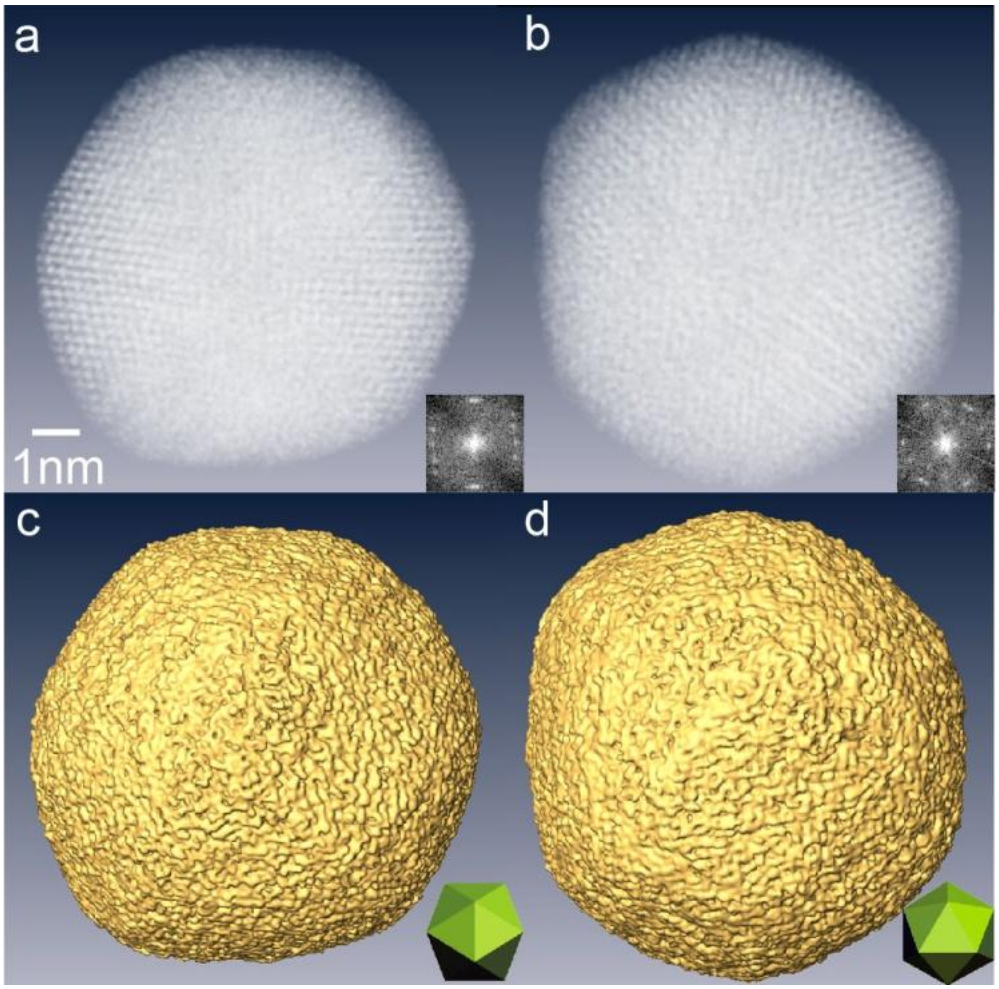

Figure 3.14. 3D structure of the reconstructed gold nanoparticle. **a**, **b**, 3D volume renderings of the nanoparticle and their Fourier transforms (insets) at the two-fold (**a**) and three-fold (**b**) symmetry orientations. c, d, Iso-surface renderings of the nanoparticle at the two-fold (**c**) and three-fold (**d**) symmetry orientations. Insets show a model icosahedron at the same orientations.

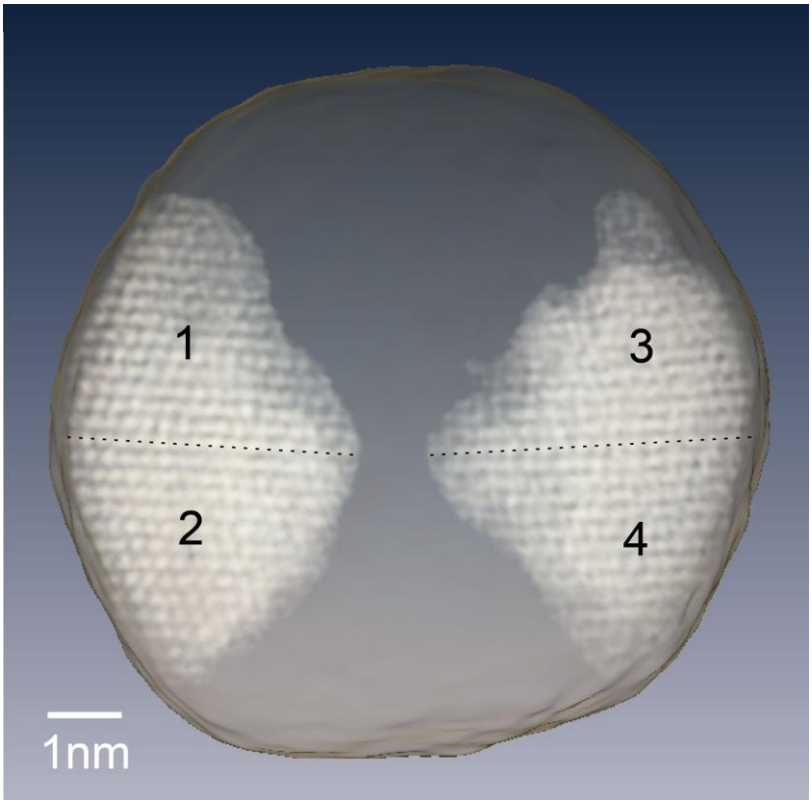

Figure 3.15. Identification of four major grains inside the gold nanoparticle in three dimensions. Grains 1, 2 and grains 3, 4 are related by mirror-reflection across the horizontal interfaces marked by dotted lines. The angle enclosed by close-packed planes across these interfaces was measured to be 69.9 °±0.8 °between grains 1 and 2, and 71.3 °±0.8 °between grains 3 and 4, both of which are consistent with the angle for a face-centered cubic twin boundary (70.53 °).

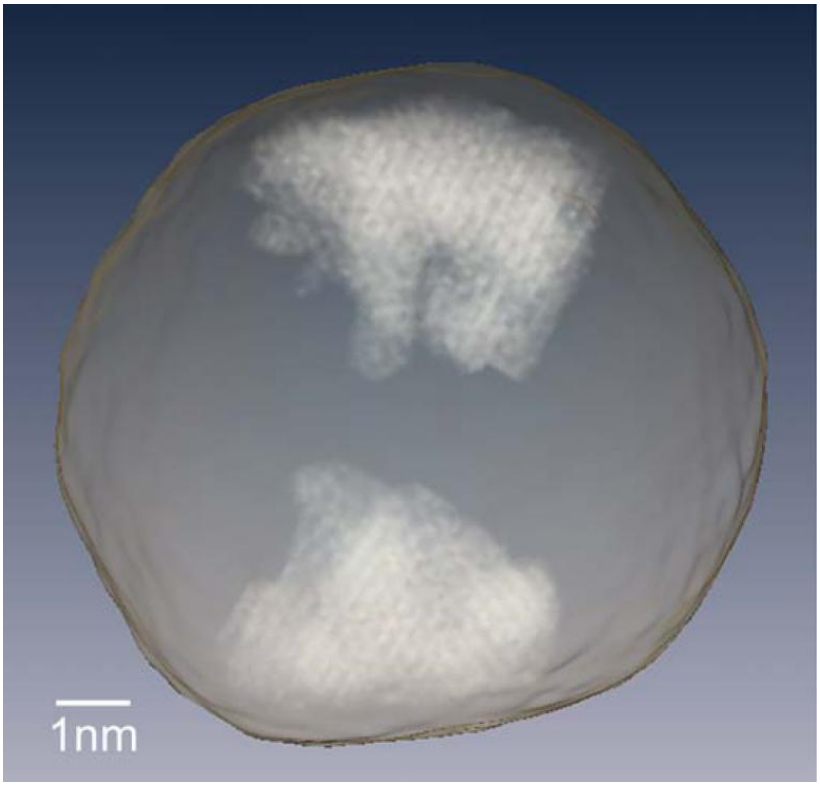

Figure 3.16. 3D grains were identified in the top and bottom parts of the reconstructed particle at the 3-fold symmetry orientation, whereas the particle at in the 2-fold symmetry orientation in Figure 3.15.

3.6 Conclusion

By combining the CM alignment technique and the EST reconstruction method with an ADF-STEM, we have determined the 3D structure of a ~10 nm gold nanoparticle at 2.4 Å resolution from a tilt series of 69 projections with a missing wedge. Several 3D grains are identified inside the nanoparticle at atomic scale resolution. While individual atoms are visible in some regions of the nanoparticle, we cannot determine all the atomic positions inside the particle. In order to identify all the atoms (estimated to be ~23800) without using atomicity and bond information, a

resolution higher than 2.4 Å is needed, which requires future developments. With aberration-corrected STEM[9, 10, 26], better 3D resolution and image quality should be achievable, but extended depth-of-field techniques may have to be applied to the tilt series before the EST reconstruction can be performed. Compared to atom-probe tomography[26], this non-destructive technique can not only handle isolated nanoparticles, but also provide 3D local structure of complex nanomaterials at atomic scale resolution. We anticipate that this general method can be applied to not only determine the 3D structure of nanomaterials at atomic scale resolution[7, 11, 12], but also improve the resolution and image quality in other tomography fields[1, 2, 17, 21, 28-30].

References

1. Frank, J. *Electron Tomography* (Plenum, New York, 1992).
2. Lučić, V., Förster, F. & Baumeister, W. Structural studies by electron tomography: from cells to molecules. *Annu. Rev. Biochem.* **74**, 833-865 (2005).
3. Midgley, P. A. & Weyland, M. 3D electron microscopy in the physical sciences: the development of Z-contrast and EFTEM tomography. *Ultramicroscopy* **96**, 413–431 (2003).
4. Midgley, P. A. & Dunin-Borkowski, R. E. Electron tomography and holography in materials science. *Nature Materials* **8**, 271-280 (2009).
5. Arslan, I., Yates, T. J. V., Browning, N. D. & Midgley, P. A. Embedded nanostructures revealed in three dimensions. *Science* **309**, 2195-2198 (2005).
6. Bar Sadan, M. *et al.* Toward atomic-scale bright-field electron tomography for the study of fullerene-like nanostructures. *Nano Lett.* **8**, 891-896 (2008).

7. Marks, L. D. Experimental studies of small particle structures. *Rep. Prog. Phys*. **57**, 603-649 (1994).
8. Bovin, J. -O., Wallenberg, R. & Smith, D. J. Imaging of atomic clouds outside the surfaces of gold crystals by electron microscopy. *Nature* **317**, 47-49 (1985).
9. D. A. Muller. Structure and bonding at the atomic scale by scanning transmission electron microscopy. *Nature Materials* **8**, 263-270 (2009).
10. Pennycook, S. J. & Nellist, P. D. *Scanning Transmission Electron Microscopy: Imaging and Analysis* 1st ed. (Springer, 2011).
11. Billinge, S. J. L. & Levin, I. The problem with determining atomic structure at the nanoscale. *Science* **316**, 561-565 (2007).
12. Yacaman, M. J., Ascencio, J. A., Liu, H. B. & Gardea-Torresdey, J. Structure shape and stability of nanometric sized particles. *J. Vac. Sci. Technol. B* **19**, 1071-1023 (2001).
13. Daniel, M. C. & Astruc, D. Gold nanoparticles: assembly, supramolecular chemistry, quantum-size-related properties, and applications toward biology, catalysis, and nanotechnology. *Chem. Rev*. **104**, 293-346 (2004).
14. Scott, C. M. *et al.* Electron tomography at 2.4-ångström resolution. *Nature* **483**, 444-447 (2012).
15. Kirkland, E. J. *Advanced Computing in Electron Microscopy* 2nd ed. (Springer, 2010).
16. Howie, A. Diffraction channelling of fast electrons and positrons in crystals. *Phil. Mag.* **14**, 223-237 (1966).
17. Lee, E. *et al*. Radiation dose reduction and image enhancement in biological imaging through equally sloped tomography. *J. Struct. Biol.* **164**, 221–227 (2008).

18. Miao, J., Föster, F. & Levi, O. Equally sloped tomography with oversampling reconstruction. *Phys. Rev. B* **72**, 052103 (2005).

19. Bailey, D. H. & Swarztrauber, P. N. The fractional Fourier transform and applications. *SIAM Rev.* 33, 389–404 (1991).

20. Miao, J., Sayre, D. & Chapman, H. N. Phase retrieval from the magnitude of the Fourier transform of non-periodic objects. *J. Opt. Soc. Am. A.* 15, 1662-1669 (1998).

21. Jiang, H. *et al*. Quantitative 3D imaging of whole, unstained cells by using X-ray diffraction microscopy. *Proc. Natl. Acad. Sci. USA* **107**, 11234–11239 (2010).

22. Miao, J., Charalambous, P, Kirz, J. & Sayre, D. Extending the methodology of X-ray crystallography to allow imaging of micrometre-sized non-crystalline specimens. *Nature* 400, 342-344 (1999).

23. Miao, J., Ohsuna, T., Terasaki, O., Hodgson, K. O. & O'Keefe, M. A. Atomic resolution three-dimensional electron diffraction microscopy. *Phys. Rev. Lett*. 89, 155502 (2002).

24. Zuo, J. M., Vartanyants, I., Gao, M., Zhang, R. & Nagahara, L. A. Atomic resolution imaging of a carbon nanotube from diffraction intensities. *Science* 300, 1419-1421 (2003).

25. Barnard, A. S., Young, N. P., Kirkland, A. I., van Huis, M. A. & Xu, H. Nanogold: a quantitative phase map. *ACS Nano* **3**, 1431–1436 (2009).

26. Batson, P. E., Dellby, N. & Krivanek, O. L. Sub-ångstrom resolution using aberration corrected electron optics. *Nature* **418**, 617-620 (2002).

27. Arslan, I., Marquis, E.A., Homer, M., Hekmaty, M. & Bartelt, N.C. Towards better 3-D reconstructions by combining electron tomography and atom-probe tomography. *Ultramicroscopy* **108**, 1579-1585 (2008).

28. Kak, A.C. & Slaney, M. *Principles of Computerized Tomographic Imaging* (SIAM, Philadelphia, 2001).

29. Fahimian, B. P., Mao, Y., Cloetens, P., & Miao, J. Low dose X-ray phase-contrast and absorption CT using equally-sloped tomograph. *Phys. Med. Bio.* **55**, 5383-5400 (2010).

30. Mao, Y., Fahimian, B. P., Osher, S. J., & Miao, J. Development and optimization of regularized tomographic reconstruction algorithms utilizing equally-sloped tomography. *IEEE Trans. Image Processing* **19**, 1259-1268 (2010).

CHAPTER 4

Imaging Three-dimensional dislocations in Platinum nanoparticles at atomic resolution by Electron Tomography

Dislocations and their interactions strongly influence many of the properties of materials, ranging from the strength of metals and alloys to the efficiency of light-emitting diodes and laser diodes[1-4]. Presently there are several experimental methods to visualize dislocations. Transmission electron microscopy (TEM) has long been used to image dislocations in materials[5-9], and high resolution electron microscopy can reveal dislocation core structures with increasing detail[10], particularly in annular dark field (ADF)[11]. A TEM image, however, represents a two-dimensional projection of a 3D object, although stereo TEM provides limited information about 3D dislocations[4]. X-ray topography can observe dislocations in three dimensions, but with a reduced resolution[12]. Using weak-beam dark-field[13] and scanning transmission electron microscopy (STEM)[14], electron tomography has been used to image 3D dislocations at a resolution of ~5 nm[15,16]. Atom probe tomography can offer higher-resolution 3D characterization of dislocations, but requires needle-shaped specimens and can detect only ~60% of the atoms in the sample[17].

In Chapter 3, it was shown that in a combination of ADF-STEM with the center of mass (CM) and equally sloped tomography (EST) methods, electron tomography has recently achieved a highest resolution of 2.4 Å[18]. However, due to dynamical scattering effects[19], the missing wedge problem[16,18,20] and Poisson noise in the tilt series, noise exists among the Bragg peaks in the 3D

Fourier transform of the EST reconstruction. As a result, while lattice structure and some individual atoms are visible in the reconstruction[18], electron tomography has not been able to reveal 3D dislocations in materials at atomic resolution. Here we overcome this obstacle by combining 3D Bragg peak filtering with high angle annular dark field (HAADF)-STEM tomography, and achieve 3D imaging of dislocations in a nanoparticle at atomic resolution[21].

4.1 Introduction to crystal defects

Perfect crystalline solids exhibit infinite periodicity along all three dimensions with atoms or molecules arranged in the repeating fixed positions. Practically such perfect crystals never exist, which however is not always a bad thing. Sometimes people intentionally introduce defects into crystals to manipulate physical properties of the material. Crystal defects can generally be divided into four basic classes: point defects, line defects, planar defects and bulk defects. Line defects are also called dislocations. Each of the four defects will be discussed in more details in the following pages.

4.1.1 Point defects – zero-dimensional imperfections

Point defects have the volume of atomic dimensions. In the lattice structure, point defects are where an atom is missing, or irregular placement of one atom. The most commonly observed point defects include self-interstitial atoms, interstitial impurity atoms, substitutional atoms and vacancies. Figure 4.1 indicates these four types of point defects. A self-interstitial atom is an extra atom of the same type with others in the crystal crowded itself into an interstitial void in the

lattice structure. An interstitial impurity atom is much smaller than the other regular atoms in the crystal, and always fit into the open space between lattice atoms. The substitution impurity atom, usually bigger than the bulk atoms, replaces one of the bulk atoms in the lattice. Vacancies are empty lattice sites where atoms should be, but are missing.

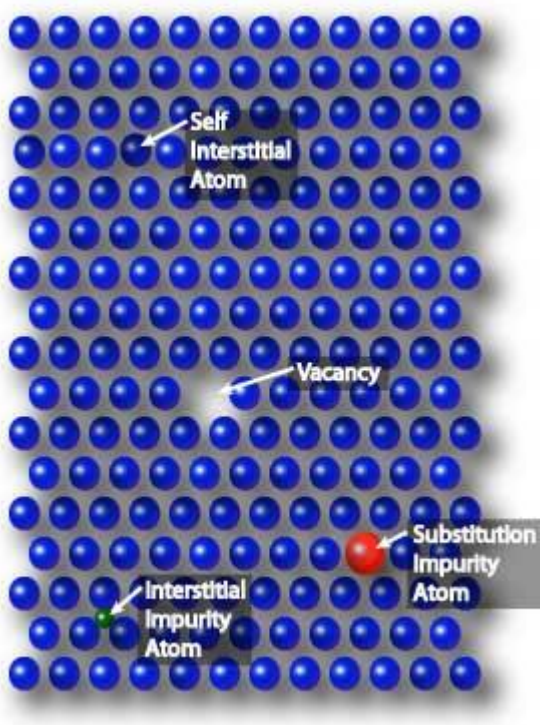

Figure 4.1 Four types of point defects in the lattice structure. Revised from Ref.[22].

4.1.2 Line defects (dislocations) – one-dimensional imperfections

The name of line defects comes from the fact that in this type of defects atoms are only misaligned along a line, which is known as the dislocation line. Dislocations are generally described by the direction of dislocation line **l** and the Burgers vector **b**[1]. The Burgers vector **b**

associated with a dislocation is a measure of the lattice distortion and usually determined from a Burgers circuit around the dislocation, which will later be illustrated in the edge and screw dislocations. There are two basic types of dislocations: the edge dislocation and the screw dislocation. These two are just the extreme cases of all possible dislocations. 'Mixed' dislocations – a hybrid of both edge and screw dislocations – and partial dislocations are most common in the real materials, but this discussion will be limited to only edge and screw dislocations.

- **Edge dislocations**

The easiest way to picture an edge dislocation is to insert an extra half-plane of atoms into the regular lattice structure, just as Figure 4.2a indicates in a cubic primitive lattice. To define the Burgers vector **b** in the edge dislocation, a Burgers circuit is drawn in Figure 4.2b. The Burgers circuit is a closed circuit that encloses the dislocation from lattice point to lattice point in a clockwise direction. This circuit is then transferred exactly to a perfect crystal lattice of the same type (Figure 4.2c). The circuit will not close because of the absence of the dislocation. The special vector needed to close the circuit in the perfect lattice is the Burgers vector, **b**=QM. From Figure 4.2, the Burgers vector **b** is perpendicular to the dislocation line in edge dislocations.

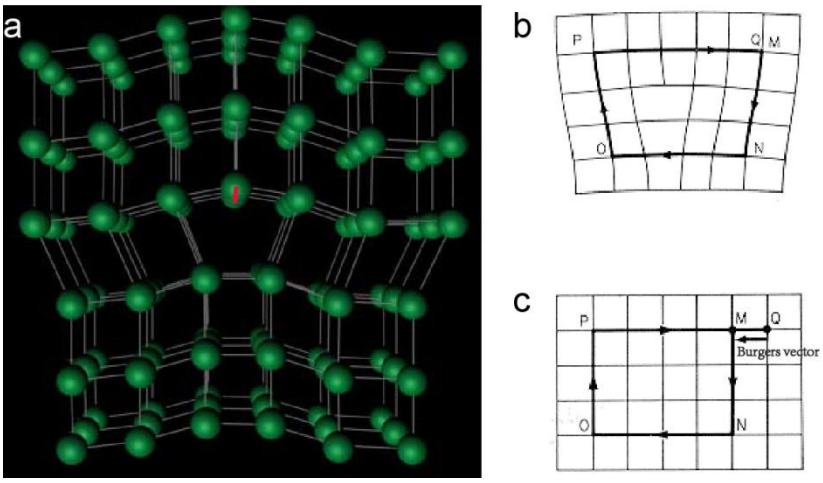

Figure 4.2. The edge dislocation in a cubic primitive lattice. **a**, 3D visualization of the edge dislocation. The red line indicates the dislocation line. **b**, The closed Burgers circuit M→N→O→P→Q(M) around the edge dislocation. **c**, The same circuit M→N→O→P→Q is transferred to the perfect lattice. Now the circuit is not closed as Q and M are not overlap. The Burgers vector QM is needed to close the circuit. Revised from Ref.[22, 23].

- **Screw dislocations**

Compared to the edge dislocation, the screw dislocation is somewhat more difficult to visualize. Shown in Figure 4.3a, the screw dislocation can be imagined as a block of metal with a shear force applied across one end and the metal begins to rip. If the two consecutive layers of atoms – one just above the rip and the other just beneath the rip – are viewed from the top, the characteristic zigzag pattern of the screw dislocation is visible (Figure 4.3b).

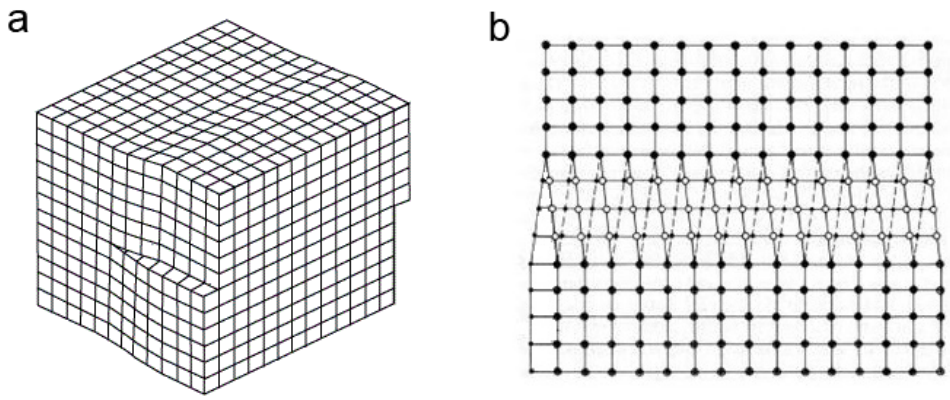

Figure 4.3. The screw dislocation in a cubic primitive lattice. **a**, 3D visualization of the screw dislocation. **b**, The characteristic zigzag pattern visible in the two consecutive layers of atoms. Revised from Ref. [24].

Similar to the edge dislocation, the Burgers vector **b** is also determined by the Burgers circuit. Figure 4.4a shows the Burgers circuit around the screw dislocation and the Burgers vector **b** is shown Figure 4.4b. Different from the edge dislocation, the Burgers vector **b** is parallel to the dislocation line in the screw dislocation.

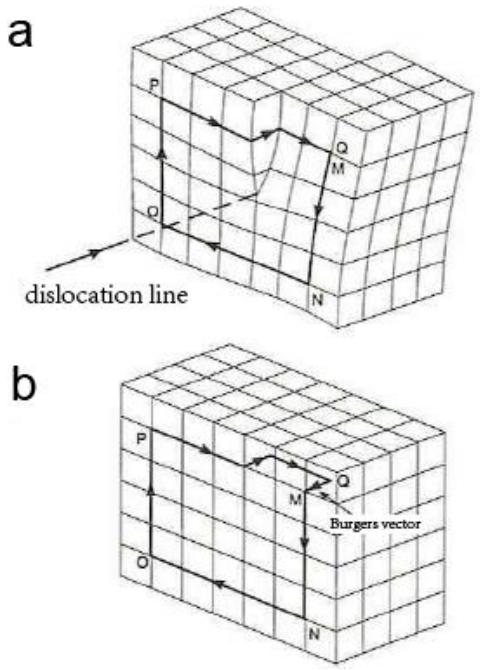

Figure 4.4. Burgers vector for the screw dislocation. **a**, The closed Burgers circuit M→N→O→P→Q(M) around the screw dislocation. **b**, The same circuit M→N→O→P→Q is transferred to the perfect lattice. Now the circuit is not closed as Q and M are not overlap. The Burgers vector QM is needed to close the circuit. The dislocation line, which is parallel to the Burgers vector, is also shown in **a**. Revised from Ref. [23].

4.1.3 Planar defects – two-dimensional imperfections

- **Stacking faults**

The stacking fault is another type of commonly observed crystal defects. It is one or two atomic layer interruption in the long-range stacking sequences of atom planes. Take face-centered cubic (fcc) lattice for example, the stacking sequence is visualized along <110> direction in Figure 4.5a with each row representing a {111} plane. It is obvious that the stacking sequence of the close-pack lattice is ABCABCABC… Here A, B and C represent {111} planes. If parts of a C-

plane are removed, then the neighboring A and B-planes should relax into the configuration shown in Figure 4.5b. Now the stacking sequence ABCABCABC… has been changed to the faulty sequence ABC***AB***ABC – A stacking fault called intrinsic stacking fault has been produced. The other kind of stacking fault is shown in Figure 4.5c. In this case the fault stacking sequence becomes ABCA***BAC***ABC… and it is called extrinsic stacking fault. Both stacking faults shown in Figure 4.5 are bordered by Frank partial dislocations[1].

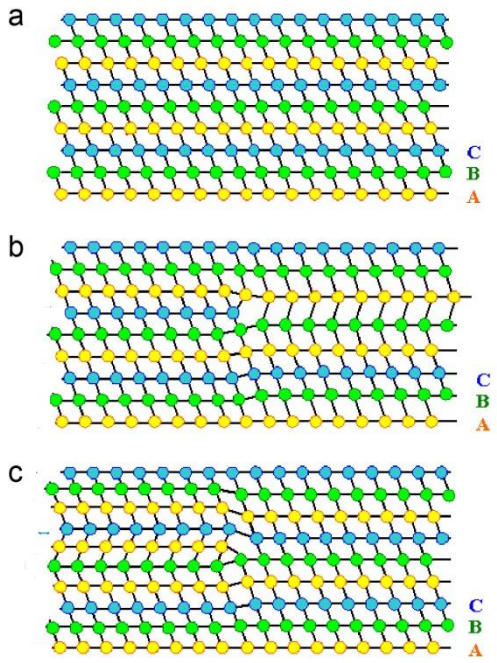

Figure 4.5. Stacking faults in the face-centered cubic (fcc) structure. **a**, The regular stacking sequence ABCABCABC shown in <110> direction. **b**, The intrinsic stacking fault in ABCABABC sequence. **c**, The extrinsic stacking fault in ABCABACABC sequence. Revised from Ref. [25].

- **Grain boundaries**

Another important type of planar defects is the grain boundary. Implied by the name, the grain boundary is the interface between two differently oriented crystallographic grains or crystallites, in a polycrystalline material. The crystallographic orientations of grains are usually rotated with the respect to neighboring grains. Grain boundaries limit the length and motion of dislocations through a material, so reducing the grain size helps to improve the strength of the material.

The twin boundary is a particular kind of grain boundaries, commonly observed in polycrystalline fcc metals. Shown in Figure 4.6, the twin boundary serves as the mirror plane where the lattices above and beneath the boundary have the mirror symmetry.

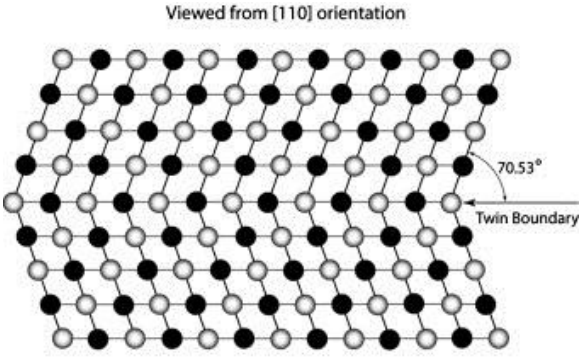

Figure 4.6. The twin boundary for an fcc structure. Each dark or light circle represents an atom column, while 'dark' columns are shifted for half an atomic distance below 'light' columns. The twin plane is the $(1\bar{1}1)$ close-packed plane, and it has a 70.53 °angle with other close-packed planes. Revised from Ref [26].

4.1.4 Bulk defects – three-dimensional imperfections

Compared to the other crystal defects discussed in this section, bulk defects occur on a much larger scale, ranging from 0.1 to 50 micron. Bulk defects include voids and precipitates. Voids are regions with no atoms inside, and can be thought of as clusters of vacancies. Precipitates are small regions of impurity atoms clustering together.

4.2 Experiments

4.2.1 Synthesis of Pt nanoparticles

The Pt nanoparticles were synthesized by peptides in aqueous solution at room temperature as reported previously[27]. All regents were dissolved in water before using. A pre-prepared vial containing precursor (chloroplatinic acid hydrate ($H_2Pt(IV)_{Cl6}.xH_2O$, 1 mM) and S7 peptide (Ser-Ser-Phe-Pro- Gln-Pro-Asn) solution (30 mg/ ml) were mixed with ascorbic acid (2 mM) immediately before injection of fresh $NaBH_4$ (0.8 mM) where $NaBH_4$ and ascorbic acid were used as reducing agents. The final volume of the reaction solution was 5 ml, and the reaction normally required more than 30 minutes.

4.2.2 Sample preparation

Pt nanoparticle solution was sonicated for ~10min to prevent aggregation. Five-nm-thick silicon nitride membranes (TEMwindows.com) were used as the particle substrates in the experiment. The thin membrane, with a size of $100 \times 1500\ \mu m$, is supported on a 100- μm-thick Si frame, allowing for a maximum tilt range of $\pm 83°$. To avoid breaking the membrane, a

micromanipulator was used to place a small drop of solution onto the outer frame of the silicon nitride grid. After gently moving the drop onto the membrane, it was removed and not allowed to dry and leave excessive Pt particles and contaminants. The silicon nitride grids were cleaned pre-deposition in a Gatan Solarus plasma cleaner (Model 950) for 20 s using a standard H_2/O_2 recipe.

To dissipate charge efficiently and make the nanoparticles more stable under an electron beam, a premium high-temperature ultrathin carbon coating (TEMwindows.com) was applied to the nanoparticles based on the following procedure. The silicon nitride membrane grid was first placed into a vacuum chamber with the temperature ramping up from 300 ℃ to 700 ℃ at a rate of 10 ℃/s. The carbon was coated during a 5 minute soak at 700 ℃. The chamber then naturally cooled to 450 ℃ over the next 5 minutes before the grid being removed. The silicon nitride membrane grid was finally loaded on a tomographic sample holder (Fischione Model 2020) for data acquisition.

4.2.3 Acquisition of tomographic tilt series using HAADF-STEM

STEM images of the Pt nanoparticles were acquired on a FEI Titan 80-300 microscope (energy: 200 keV; spherical aberration: 1.2 mm; illumination semi-angle, 10.7 mrad). The 100pA electron beam was focused to a probe with a 50 μm probe-forming aperture (C2) and rastered over the sample. The scattered electrons were captured by a Fischione Model 3000 HAADF detector with angles between 35.2 and 212.3 mrad from the optical axis. The use of HAADF angles was to reduce the nonlinear intensities and diffraction contrast in the images. The maximum tilt angles were limited by the holder to ±75°. To reduce vibration and drift during data acquisition, the sample holder was allowed to settle for one hour after insertion into the microscope and also for

several minutes after moving to each new angle. Tilt series were manually acquired by changing the angle with equal slope increments[18,28-31]. When focusing an image, a nearby nanoparticle (generally within 20nm along the rotation axis) was first viewed, thus reducing the unnecessary radiation dose to the particle under study[32]. Using this low exposure acquisition scheme, a tomographic tilt series of 104 projections with equal sloped increments and a tilt range of ±72.6 ° was acquired from a Pt nanoparticle. Figs. 4.7 and 4.8 show the tilt series of 104 projections and their corresponding Fourier transform. The probe current was ~100 pA with a dwell time of 48 μs per pixel, and the magnification of each projection was 3.6×10^6. The total electron dose of the tilt series was estimated to be ~2.5×10^7 e/Å^2. To monitor beam induced changes to the Pt nanoparticle, three 0 °projections were measured during the acquisition of the tilt series (Fig. 4.9). The consistency of these projections indicates that the lattice structure of the nanoparticle was stable throughout the experiment. Since the pixel size in STEM mode may vary, a calibration image of an oriented single crystal Au foil (Ted Pella) was taken in STEM mode under the same conditions, and the STEM pixel size was characterized to be 0.35 Å. To enhance the SNR in the projections of the tilt series, 1.5×1.5 pixel binning was performed for each projection. The pixel size of the binned projections is 0.53 Å.

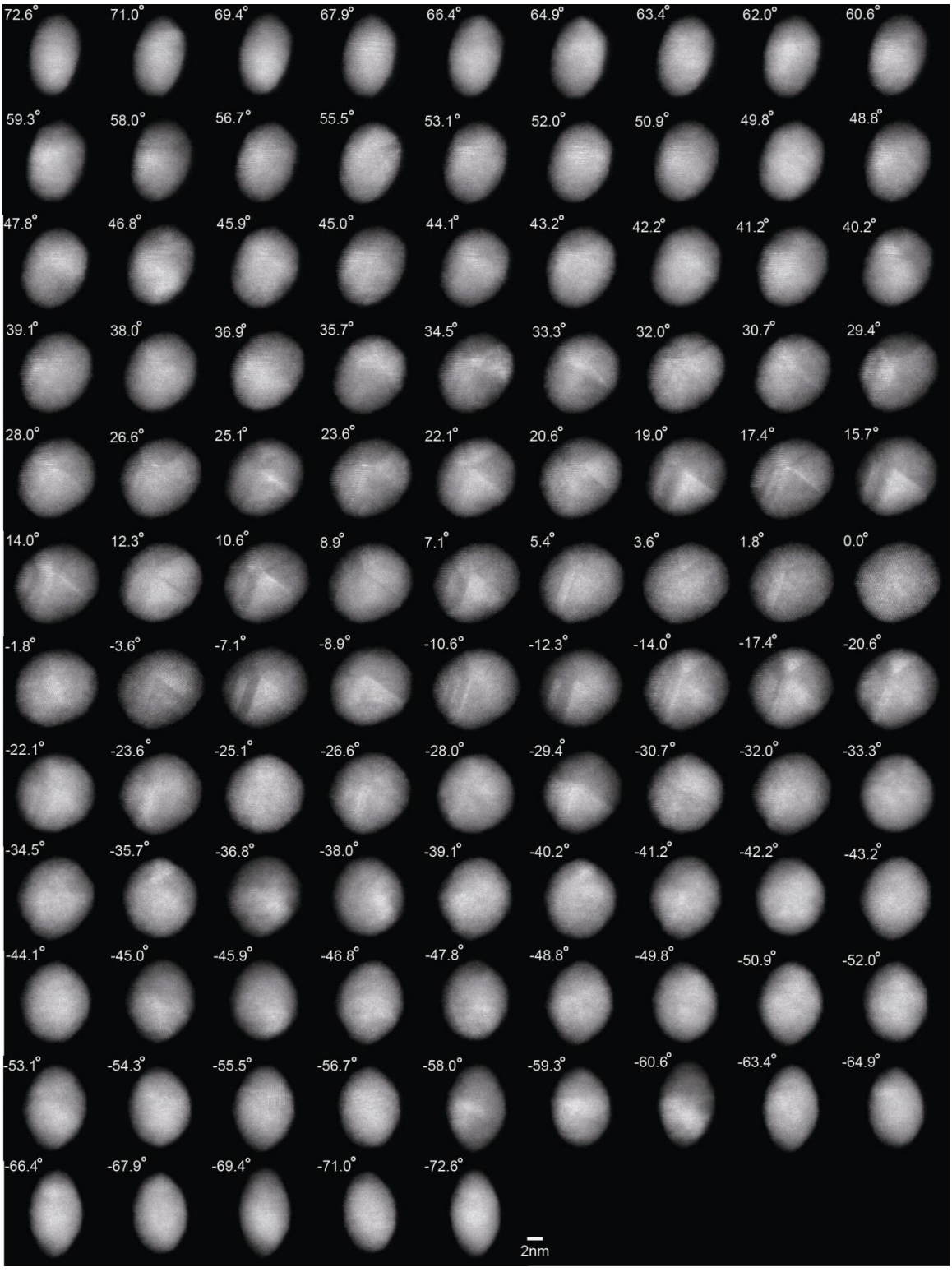
72.6° 71.0° 69.4° 67.9° 66.4° 64.9° 63.4° 62.0° 60.6°
59.3° 58.0° 56.7° 55.5° 53.1° 52.0° 50.9° 49.8° 48.8°
47.8° 46.8° 45.9° 45.0° 44.1° 43.2° 42.2° 41.2° 40.2°
39.1° 38.0° 36.9° 35.7° 34.5° 33.3° 32.0° 30.7° 29.4°
28.0° 26.6° 25.1° 23.6° 22.1° 20.6° 19.0° 17.4° 15.7°
14.0° 12.3° 10.6° 8.9° 7.1° 5.4° 3.6° 1.8° 0.0°
-1.8° -3.6° -7.1° -8.9° -10.6° -12.3° -14.0° -17.4° -20.6°
-22.1° -23.6° -25.1° -26.6° -28.0° -29.4° -30.7° -32.0° -33.3°
-34.5° -35.7° -36.8° -38.0° -39.1° -40.2° -41.2° -42.2° -43.2°
-44.1° -45.0° -45.9° -46.8° -47.8° -48.8° -49.8° -50.9° -52.0°
-53.1° -54.3° -55.5° -56.7° -58.0° -59.3° -60.6° -63.4° -64.9°
-66.4° -67.9° -69.4° -71.0° -72.6°
2nm

Figure 4.7. Experimental tilt series of 104 projections with a tilt range of $\pm 72.6\,^{\circ}$ and equal slope increments, acquired from a Pt nanoparticle using HAADF-STEM (energy: 200 keV; spherical aberration: 1.2 mm; illumination semi-angle: 10.7 mrad; detector inner and outer angles: 35.2 and 212.3 mrad; pixel size: 0.35 Å). The total electron dose of the tilt series was estimated to be $\sim 2.5 \times 10^{7}$ e/Å^{2}. Careful examination of the projections suggests that the facets of this nanoparticle are not sharply defined.

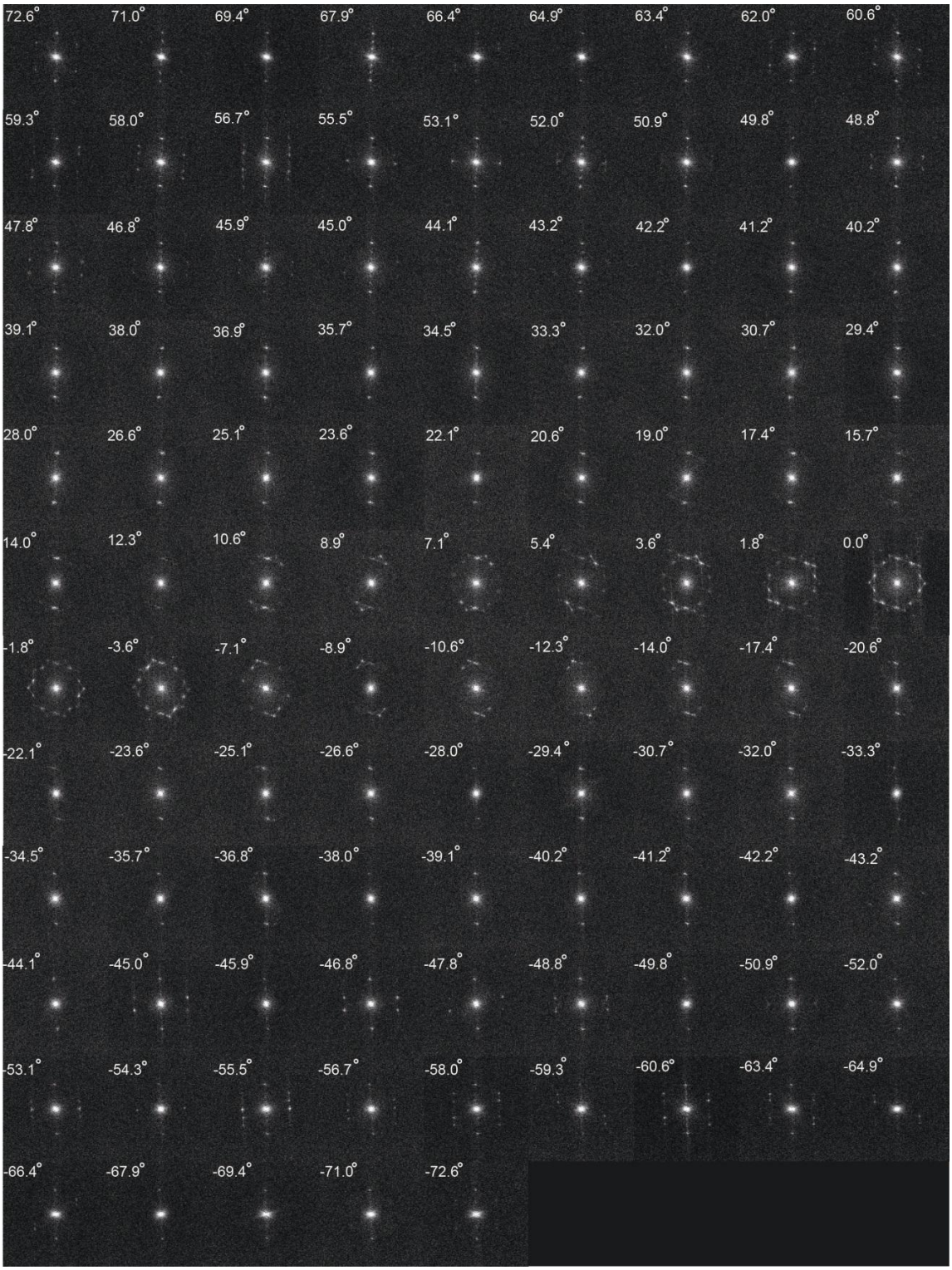

Figure 4.8. Fourier transforms of the 104 projections (Fig. 4.7), in which Bragg peaks are visible in most projections.

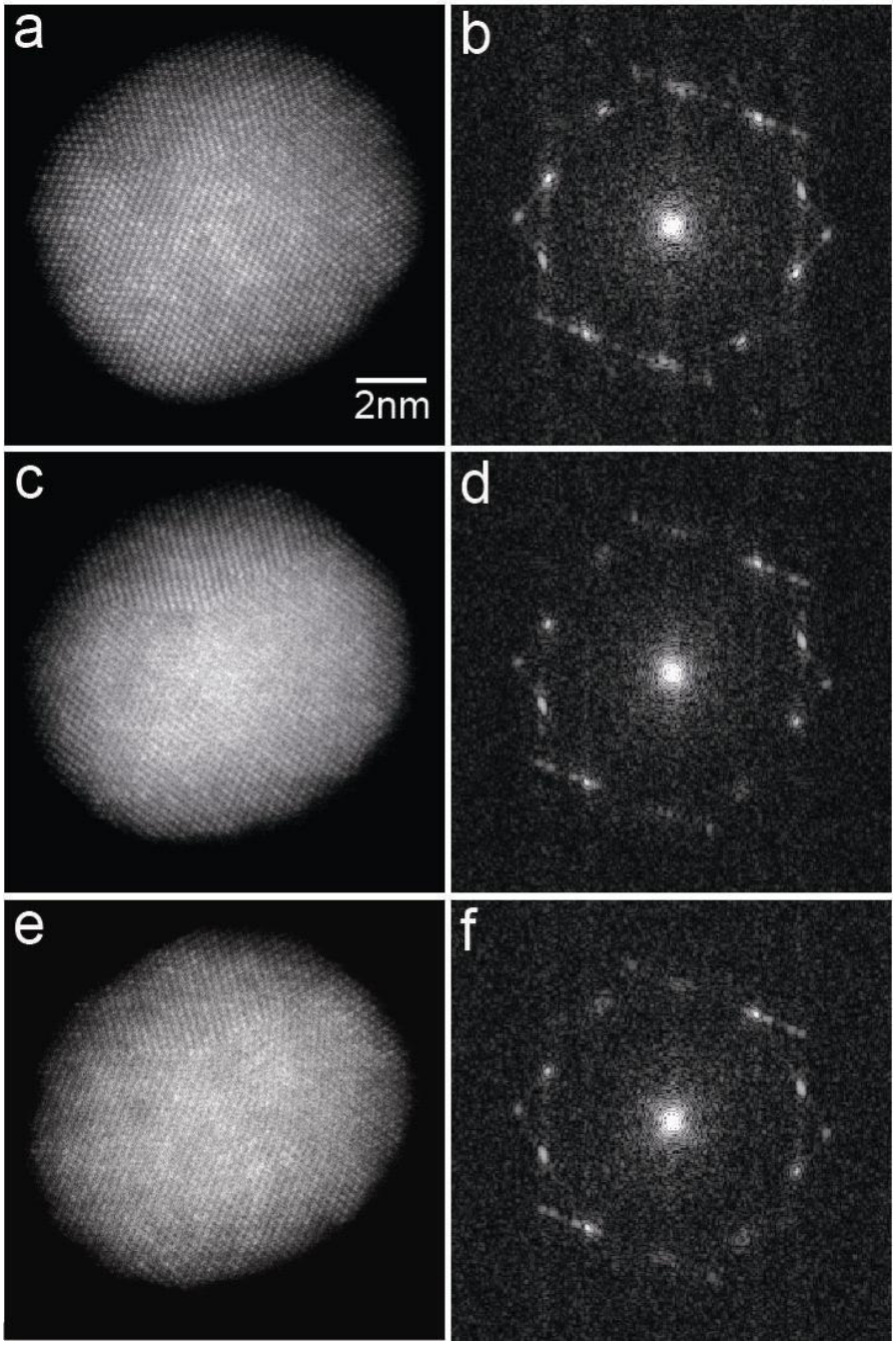

Figure 4.9. Three 0 °projections (**a**,**c**,**e**) and their Fourier transforms (**b**,**d**,**f**) measured during the acquisition of the tilt series (Fig. 4.7) to monitor beam induced changes to the Pt nanoparticle. While some minor structural changes occurred on the surface of the three projections, the lattice structure of the nanoparticle was consistent throughout the experiment.

4.3 EST reconstruction and 3D Fourier filtering

4.3.1 EST reconstruction

After performing background subtraction and CM alignment (Section 3.1), the tilt series was reconstructed by the EST method[18, 28-31]. The EST iterative algorithm started with converting the measured projections to Fourier slices by the fractional Fourier transform[33]. The algorithm then iterated alternately between real and reciprocal space through the use of the pseudopolar fast Fourier transform[34]. In real space, the voxel values outside a loose support (that is, a rectangular box larger than the true boundary of the structure to be reconstructed) and the negative voxel values inside the support were set to zero, whereas in reciprocal space the corresponding calculated Fourier slices were replaced with the measured ones and the remaining slices kept unchanged in each iteration. Each iteration was monitored by an error metric, defined as the difference between the measured and calculated Fourier slices, and the algorithm was terminated after reaching a maximum number of iterations. Using the iterative EST algorithm, a preliminary 3D reconstruction was obtained after 500 iterations. An updated 3D support was determined by convolving the reconstruction with a Gaussian window and selecting a suitable cut-off. The 3D shape of the support was also double checked by examining the reconstruction slice-by-slice to ensure the support does not crop the structure. Using the updated support, we performed another 500 iterations to obtain a new reconstruction. To further improve the 3D reconstruction, we also projected the reconstruction back to calculate projections at given angles. By computing the cross-correlation between the calculated and measured projections, we further adjusted the alignment of the projections to achieve maximum consistency in 3D reconstruction. Usually the shift should be one pixel or smaller in each dimension. Otherwise, the data analysis and CM

alignment procedure has to be re-done. We then repeated the procedure for improving the support and back-projection alignment. The final reconstruction was obtained when no further improvements can be made.

4.3.2 3D Fourier Filtering

Figure 4.10a shows the 3D Fourier transform of the reconstruction and Fig. 4.10c shows a 2.6-Å-thick central slice in the *x*-*y* plane, where the electron beam is along the z axis. However, owing to the low signal-to-noise ratio (SNR) in the EST reconstruction, 3D dislocations within the nanoparticle cannot be identified at atomic resolution. To enhance the SNR of the reconstruction, we developed a 3D Fourier filtering method to identify all the measurable 3D Bragg peaks and the 3D distribution around each peak by using the following procedure. First, the 3D Fourier transform of the raw reconstruction of the Pt nanoparticle consist of two sets of lattice planes {111} and {200}. The intensities of the {111} peaks were estimated to be several times higher than those of the {200} peaks. We calculated the average radial distance (d) between the {111} and {200} peaks. Two radii were then determined by Rin = R111 - d and Rout = R200 + d, where R111 and R200 are the average radial distance for the {111} and {200} peaks, respectively. By keeping those voxels in the 3D Fourier transform with their radii between Rin and Rout, and setting other voxels to zero, we obtained a 2-shell volume including all the measurable 3D Bragg peaks.

Next, we implemented a method to further reduce noise among the Bragg peaks within the 2-shell volume. We chose the highest intensity {111} Bragg peak as a reference peak and calculated thresholds based on the reference peak. We scanned through the thresholds from 1%

to 20% of the reference peak with 1% per step. For each threshold, we set those voxels with values larger than the threshold to one and the other voxels to zero, and obtained a 3D mask. The 3D mask was convolved with a 3 voxel diameter sphere to compute a new 3D mask where the convolution process was to retain the 3D distribution of each Bragg peak. By multiplying the new 3D mask with the Fourier transform of the raw reconstruction, we obtained a new 3D Fourier transform. By monitoring the change of noise among the Bragg peaks, we found that a threshold with 10% of the reference peak is large enough to remove noise among the 3D Bragg peaks, while retaining all the measurable {111} and {200} peaks and the 3D distribution around each peak (Fig. 4.11). Figure 4.10b shows the 3D Fourier transform of the reconstruction after 3D Fourier filtering, in which the red and black dots indicate the {111} and {200} peaks of the Pt nanoparticle, respectively. The optimized threshold of 10% of the reference peak obtained here may vary for different samples.

Finally, by applying the inverse Fourier transform to the Fig. 4.10b and multiplying it by a 3D shape (that is, a tight support) of the Pt nanoparticle determined from the EST reconstruction, we obtained the 3D structure of the Pt nanoparticle with a size ~$11.2 \times 10.7 \times 7.1\ nm^3$. Fig. 4.10d shows a 2.6-Å-thick central slice in the *x-y* plane of the Pt nanoparticle, in which nearly all the atoms are visible. To confirm the accuracy of the 3D Fourier filtering method we use two independent approaches: (1) multislice STEM simulations[35] of a decahedral Pt nanoparticle with edge and screw dislocations and (2) performing a comparison with a 3D Wiener filter[36] on the same experimental data. These two approaches will be explicitly explained in the next two sections.

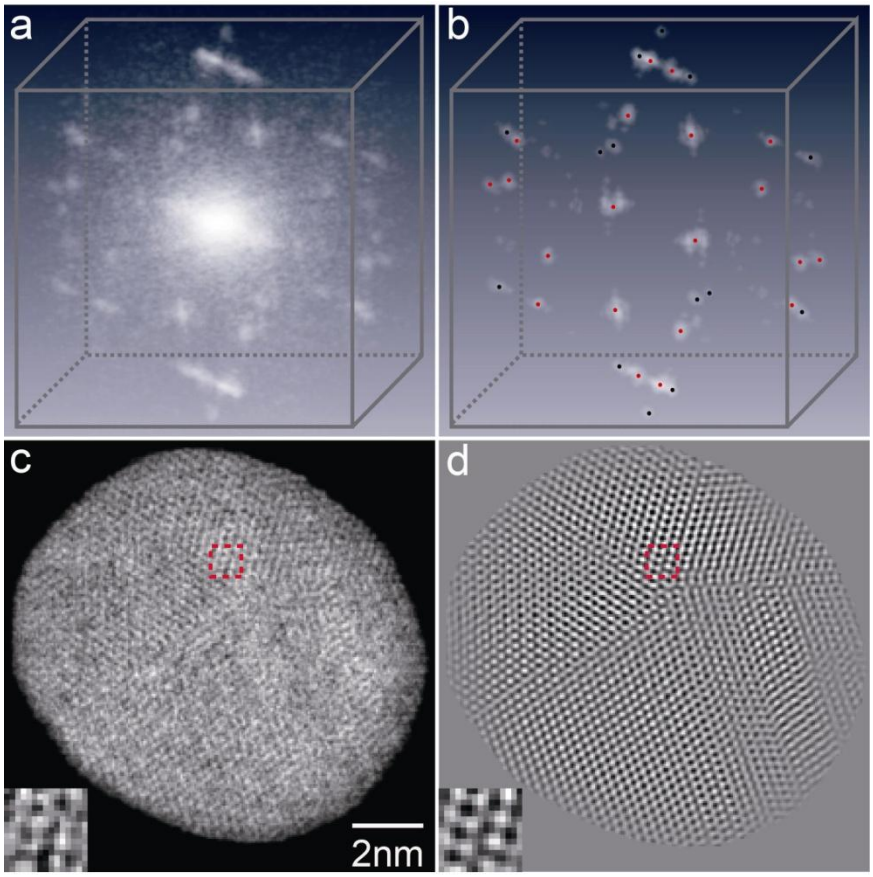

Figure 4.10. 3D reconstruction of a multiply twinned Pt nanoparticle before and after applying a 3D Fourier filter. **a**, 3D Fourier transform of the raw reconstruction of the nanoparticle. **b**, 3D Fourier transform of the reconstruction after 3D Fourier filtering where the {111} and {200} Bragg peaks are labelled with red and black dots, respectively. **c**, A 2.6-Å-thick central slice in the *x*-*y* plane of the raw reconstruction, where the z-axis is along the beam direction **d**, The same slice of the 3D structure after applying a 3D Fourier filter, in which nearly all the atoms (in white) are visible. The clear boundary of the nanoparticle is due to the multiplication of the 3D structure with a 3D shape obtained from the EST reconstruction. The insets show an enlarged region of the atomic positions before and after applying a 3D Fourier filter.

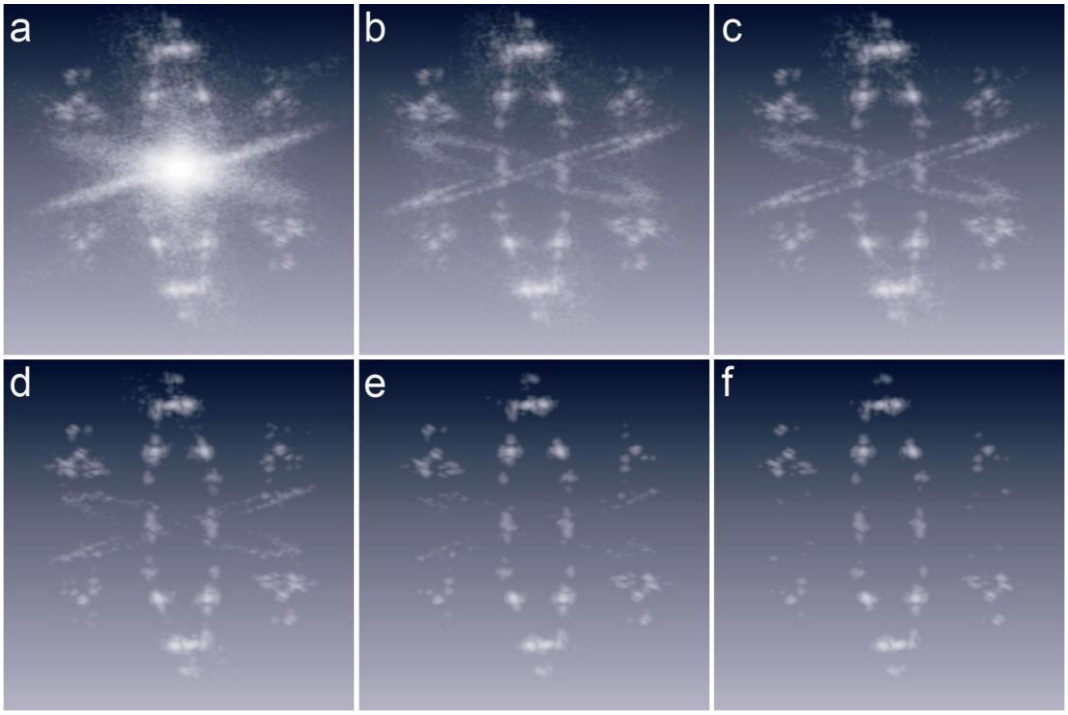

Figure 4.11. 3D Fourier filtering of the EST reconstruction of the Pt nanoparticle. **a-f**, 3D Fourier transforms of the reconstruction after applying a 3D Fourier filter with varying thresholds: (**a**) 5%, (**b**) 6%, (**c**) 7%, (**d**) 8%, (**e**) 9% and (**f**) 10% of the highest intensity {111} Bragg peak in which the central peak has been filtered out. For each threshold, we set those voxels with values larger than the threshold to one and the other voxels to zero, and obtained a 3D mask. After convolving the 3D mask with a 3 voxel diameter sphere, we obtained a new 3D mask to identify all the measurable Bragg peaks and the 3D distribution around each peak. In this experiment, we found that a threshold of 10% is large enough to remove noise among the 3D Bragg peaks (especially cross-streak noise in the images), while retaining all the measurable {111} and {200} peaks and the 3D distribution around each peak. Cross-streak noise is due to the missing wedge problem. Although the EST method can significantly alleviate the missing wedge problem, it cannot completely solve it[20]. We have also tried a 7% threshold for the experimental data and obtained consistent results as the 10% case (Fig. 4.18).

4.3.3 Numerical simulations and results

To further examine the 3D Fourier filtering method, we performed numerical simulations on a $7.3 \times 7.0 \times 4.5\ nm^3$ decahedral Pt nanoparticle with multislice calculations. The Pt particle consists of 4015 atoms with edge and screw dislocations (Figs 4.13a–c, 4.14a and b). A tilt series of 63 projections with a tilt range of $\pm 72.6°$ and equal-slope increments was calculated by performing multislice STEM simulations (Fig. 4.12). Two levels of Poisson noise were added to the projections of the tilt series with total electron doses of $2.52 \times 10^5 e\text{Å}^{-2}$ and $5.67 \times 10^4 e\text{Å}^{-2}$, corresponding to $R_{noise} = 10\%$ and 20%, respectively. Here R_{noise} is an R-factor used to define the level of Poisson noise,

$$R^{\theta}_{noise} = \frac{\sum_{x,y} \left| P^{\theta}_{noise}(x,y) - P^{\theta}_{simulated}(x,y) \right|}{\sum_{x,y} P^{\theta}_{simulated}(x,y)} \qquad \text{(Eq.4.1)}$$

Where $P^{\theta}_{simulated}(x,y)$ is the projection calculated from multislice STEM simulations at angle θ, and $P^{\theta}_{noise}(x,y)$ is the same projection with Poisson noise added. After computing R^{θ}_{noise} for each projection, we calculated R^{θ}_{noise} by averaging R^{θ}_{noise} for all the projections.

The two tilt series were aligned and reconstructed by the CM and EST methods[18, 28-31] (Fig. 4.13d-f, j-l). Because of the low SNR in the reconstructions, not all the atoms or dislocations are visible in the raw 3D reconstructions, especially with $R_{noise} = 20\%$ (Fig. 4.13j-l). After applying a 3D Fourier filter to the raw reconstructions, we obtained two 3D structures of the simulated Pt nanoparticle with all the atoms resolved (Fig. 4.13g-i, m-o). Furthermore, 3D grain boundaries, as well as the 3D core structures of edge and screw dislocations were determined at atomic resolution and are consistent with those in the model (Figs 4.13g-i, m-o and 4.14c-f).

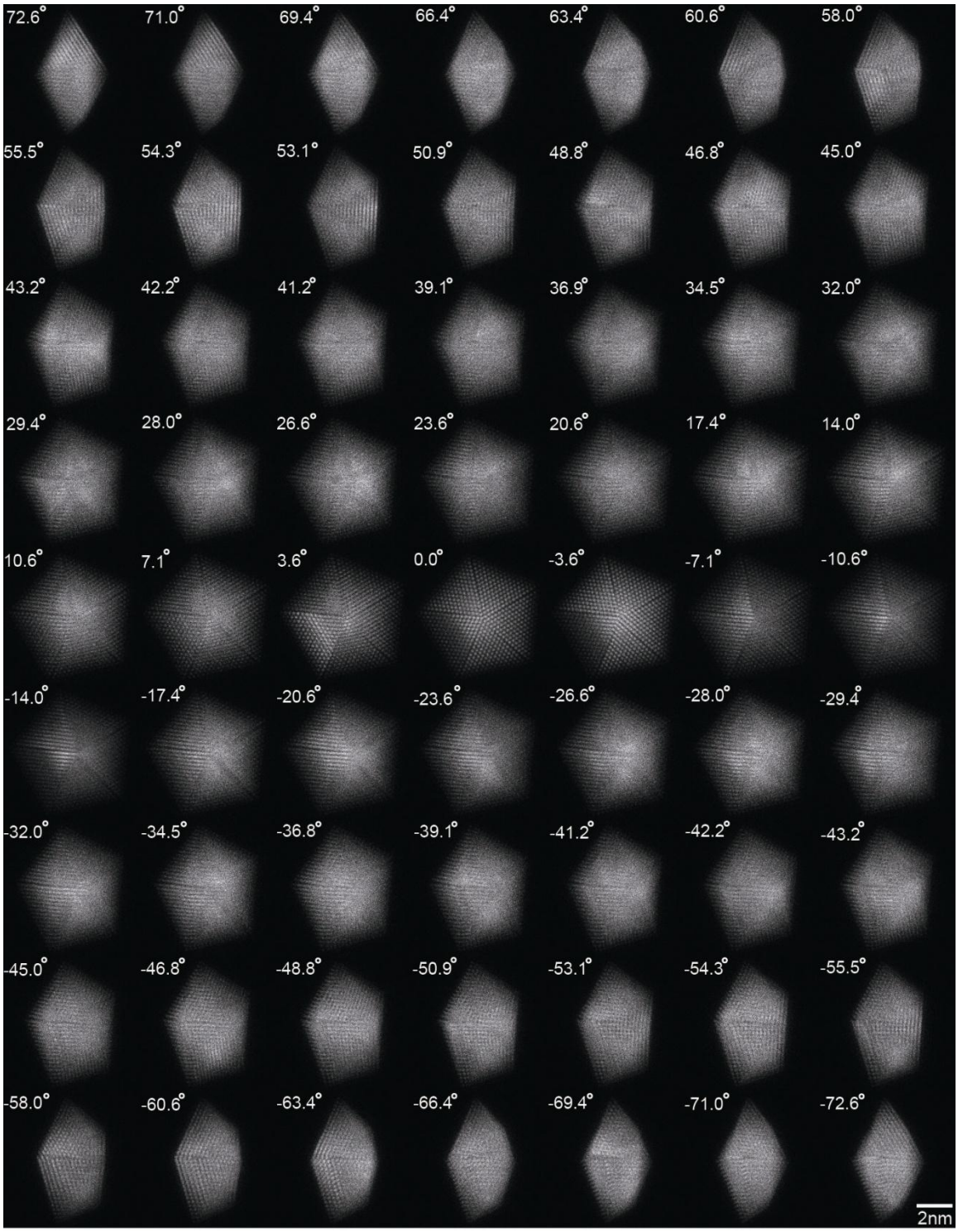

Figure 4.12. Multislice calculations of the simulated Pt nanoparticle (energy: 200 keV, spherical aberration: 1.2 mm, illumination semi-angle: 10.7 mrad, defocus: 54.86 nm, detector inner and

outer angles: 35.2 and 212.3 mrad, pixel size: 0.35 Å). A tilt series of 63 projections was calculated with a tilt range of ±72.6 °and equal slope increments. To avoid the zone axis orientations and reduce the non-linear effects, the nanoparticle was rotated by 1 °each around the horizontal (X) and tilt (Y) axes. Poisson noise was added to the tilt series with a total electron dose of 5.67×10^4 e/Å^2 and R_{noise} = 20%.

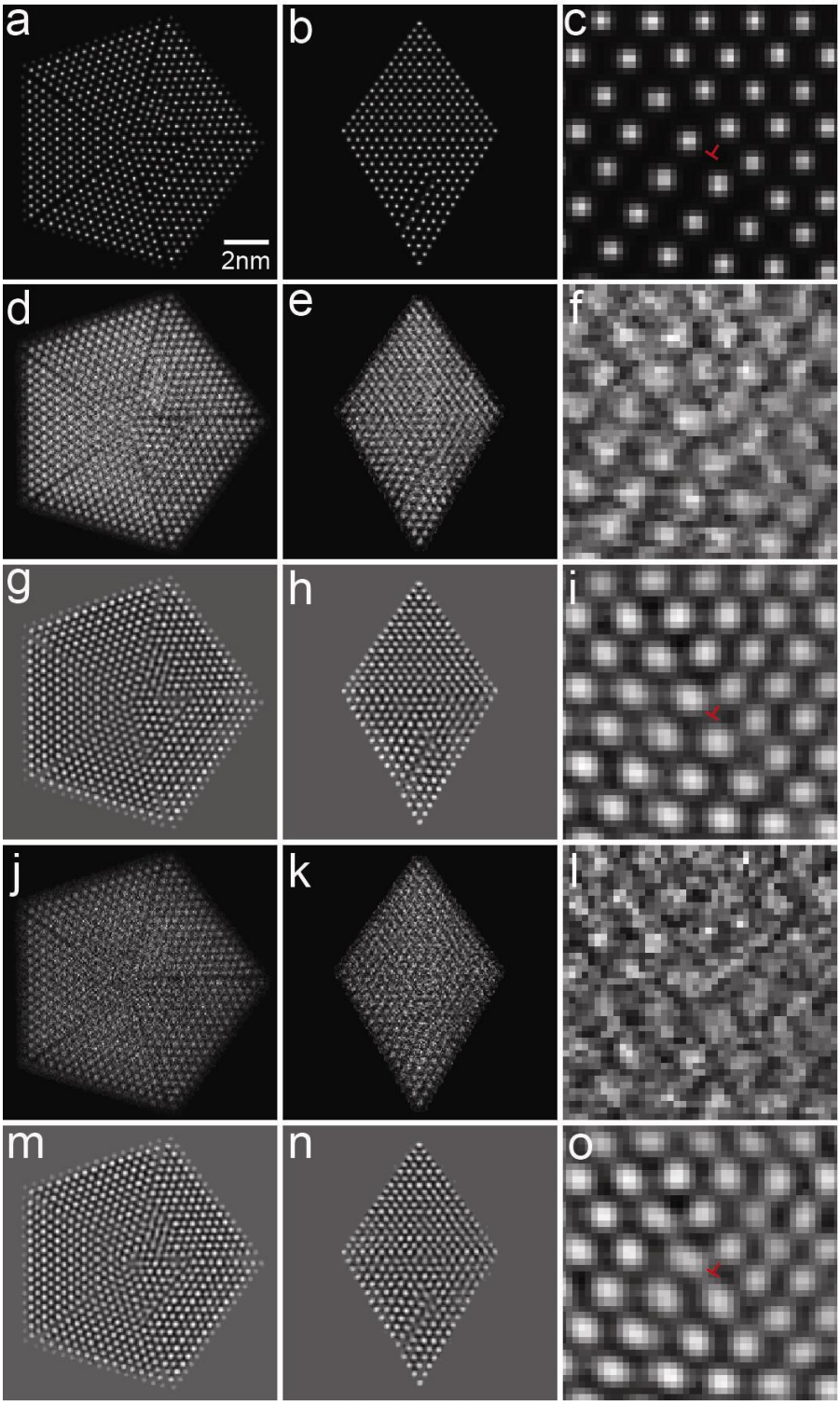

Figure 4.13. EST reconstruction of a simulated decahedral Pt nanoparticle using multislice STEM calculations. The 7.3×7.0×4.5 nm^3 Pt particle consists of a total of 4015 atoms with edge

and screw dislocations. A tilt series of 63 projections with a tilt range of $\pm 72.6°$ and equal slope increments was obtained using multislice STEM calculations[35] (Fig. 4.12). To simulate experimental conditions, the tilt angles were continuously shifted from $0°$ to $0.5°$ over the process of the tilt series. Two levels of Poisson noise were added to the projections of the tilt series with a total electron dose of $2.52 \times 10^5 e\text{Å}^{-2}$ and $5.67 \times 10^4 e\text{Å}^{-2}$, corresponding to R_{noise} of 10% and 20%, respectively. **a** nd **b**, Two 2.6 Å thick central slices of the Coulomb potential of the simulated nanoparticle in the XY and ZX planes, where the Z-axis is the beam direction. **c**, Zoomed view of an edge dislocation in a 2.6 Å thick slice, obtained after a $-90°$ rotation of the nanoparticle around the Y-axis and another $-35.3°$ rotation around the Z axis. **d**, **e** and **f**, The corresponding 2.6 Å thick slices and the edge dislocation reconstructed from 63 multislice STEM projections with R_{noise} = 10%. **g**, **h** and **i**, The corresponding 2.6 Å thick slices and the edge dislocation with R_{noise} = 10%, after applying a 3D Fourier filter with an optimized threshold of 5% of the highest intensity {111} Bragg peak. Compared to the threshold (10%) used for the experimental Pt nanoparticle, a smaller threshold (5%) here is because cross-streak noise in this reconstruction is lower than that in the experimental data (Fig. 4.11). The clear boundary of the reconstructed nanoparticle is due to the multiplication of the filtered structure with a 3D shape obtained from the EST reconstruction. **j**, **k** and **l**, The corresponding 2.6 Å thick slices and the edge dislocation from the raw reconstruction with R_{noise} = 20%. **m**, **n** and **o**, The corresponding 2.6 Å thick slices and the edge dislocation with R_{noise} = 20% after applying a 3D Fourier filter with a threshold of 5%. After applying the 3D Fourier filter, all the atoms in the 3D reconstructions (**g**, **h**, **m** and **n**) are visible. The 3D core structure of the edge dislocation is observed at atomic resolution (**i** and **o**) and consistent with the model (**c**). In our numerical simulations, we have also found that 3D Fourier filtering is more accurate than the 2D case.

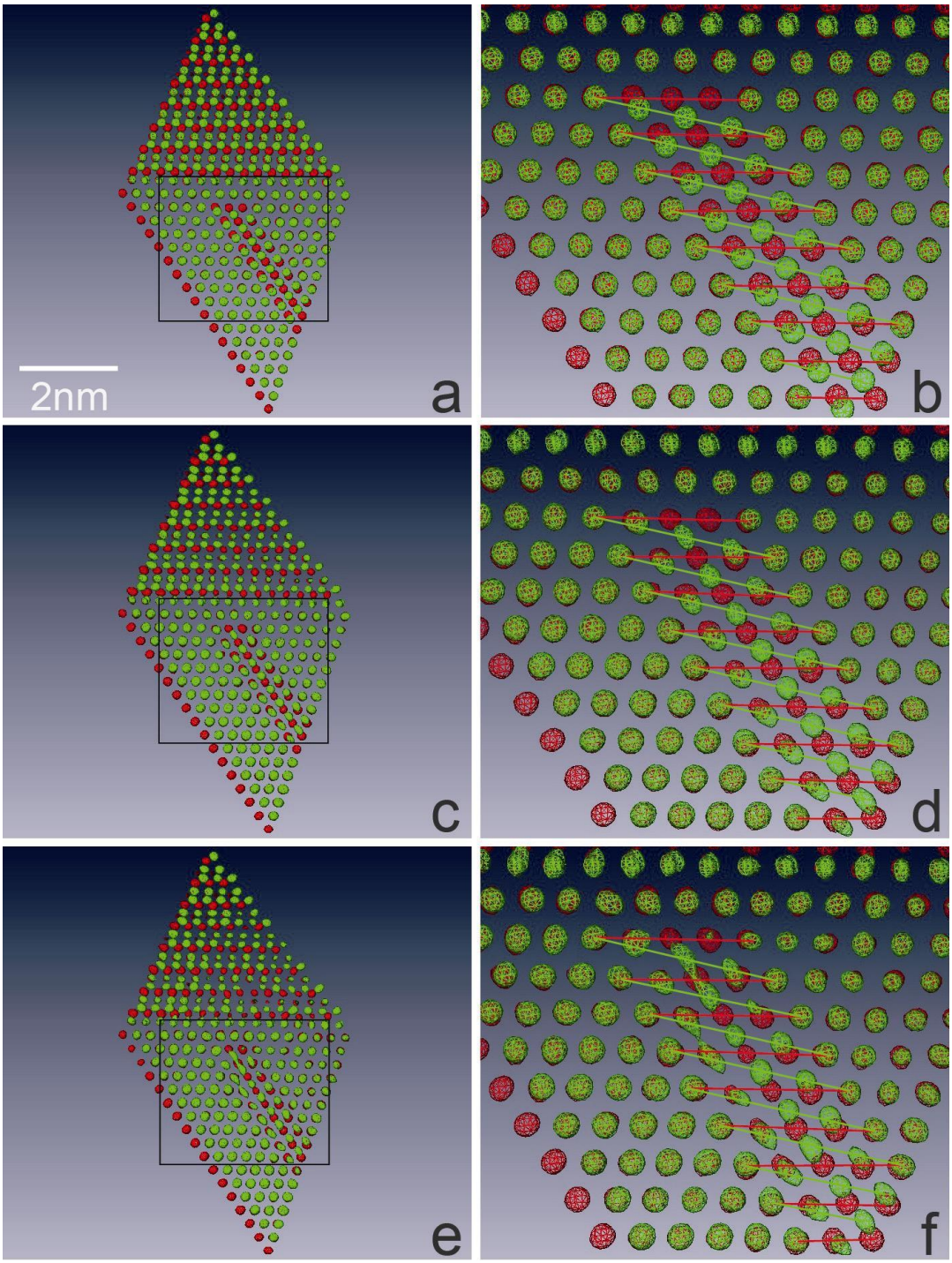

Figure 4.14. Multislice simulations on 3D imaging of a screw dislocation at atomic resolution. **a**, A 4.8 Å thick slice (about two atomic layers) of the simulated Pt nanoparticle. **b**, Zoomed view of a screw dislocation, in which the zigzag pattern, a characteristic feature of a screw dislocation,

is visible. **c** and **d**, The corresponding 4.8 Å thick slice and zoomed view of the screw dislocation after applying a 3D Fourier filter to the EST reconstruction with R_{noise} = 10%. **e** and **f**, The corresponding 4.8 Å thick slice and zoomed view of the screw dislocation after applying a 3D Fourier filter to the reconstruction with R_{noise} = 20%. In both reconstructions, the 3D core structure of the screw dislocation is visible (**d** and **f**) and consistent with the model (**b**).

In our numerical simulations, we also found that, compared to 2D Fourier filtering method[37-39], 3D Fourier filtering is more accurate. This is because in 3D Fourier filtering, each voxel in 3D reciprocal space is correlated to all voxels in 3D real space, and vice versa. But in 2D Fourier filtering, the correlated information only exists in two dimensions. Thus, for a given object, there is more correlated information (voxels) in 3D Fourier filtering than in the 2D case.

4.3.4 3D Fourier filtering method verified by 3D Wiener filter

To verify the 3D Fourier filtering method, we performed a comparison with a 3D Wiener filter using the same experimental data. The Wiener filter is well established for reducing the noise in a signal, and it is applied to TEMimages[40]. Fig. 4.15b-d shows the 2.6-Å-thick central slice in the *x-y* plane of the reconstruction after applying the 3D Wiener filter $S^2/(S^2 + \lambda n^2)$, where S is an estimate of the signal, n is the noise and λ = 1, 2 and 3. Fig. 4.15f-j shows enlarged views of four regions for the raw reconstruction, and the reconstructions with the 3D Wiener filter (λ = 1, 2 and 3) and the 3D Fourier filter. Although the result with the λ = 1 Wiener filter is nosier, the atomic positions in the reconstructions using the λ = 2 and 3 Wiener filters and the 3D Fourier filter are consistent.

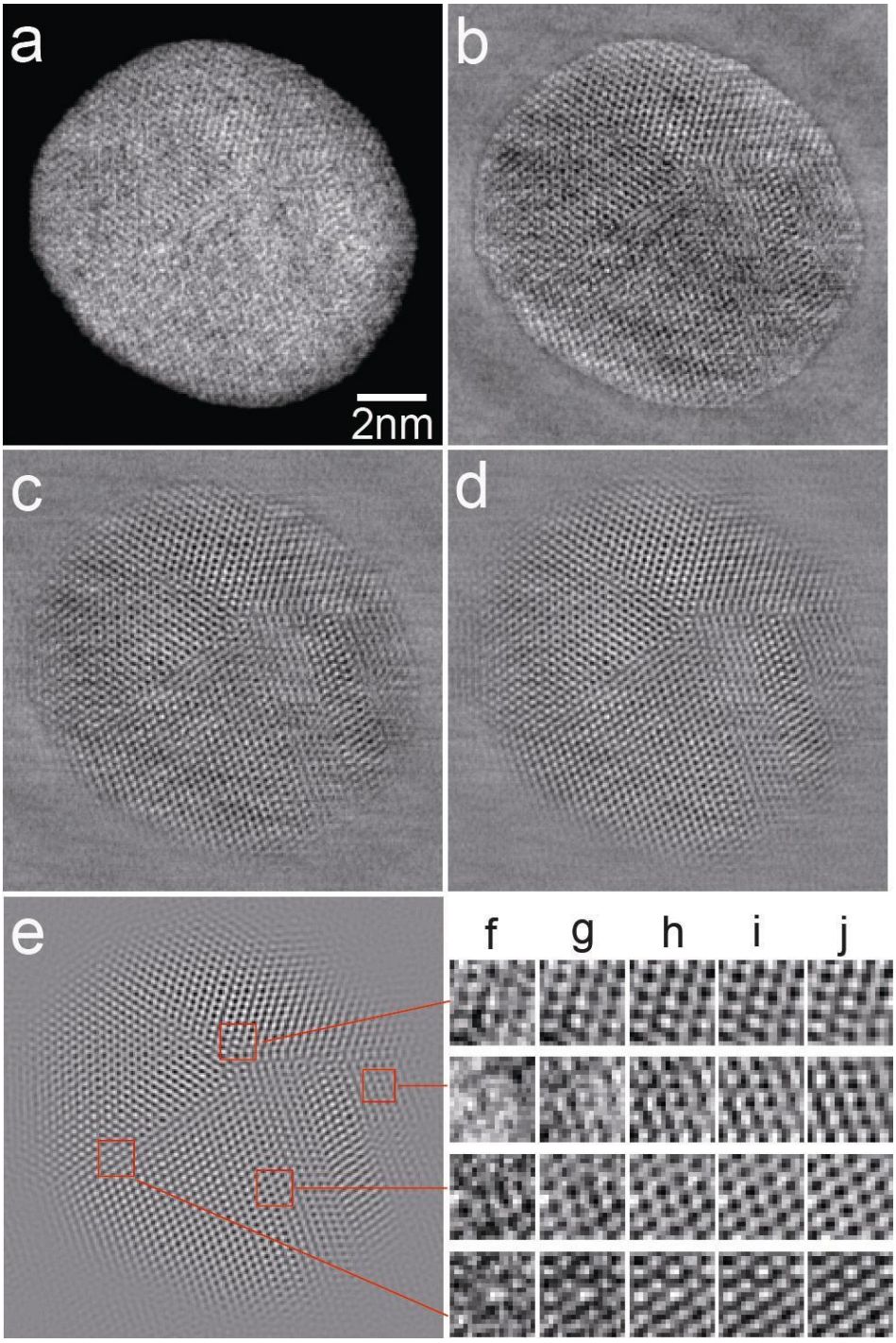

Figure 4.15. Comparison between 3D Wiener and 3D Fourier filtering. **a**,2.6 Å thick central slices in the XY plane of the raw reconstruction. **b-d**, The same slice of the reconstruction with a 3D Wiener filter (λ = 1, 2 and 3). **e**, The same slice of the reconstruction with a 3D Fourier filter

(threshold = 10%). **f-j**, Zoomed views of four regions in (**a-e**), respectively. While the result with the $\lambda = 1$ Wiener filter is nosier, the atomic positions with the $\lambda = 2$ and 3 Wiener filter and the 3D Fourier filter are consistent. Due to the convolution effect in applying the 3D Wiener and 3D Fourier filters, the boundary of the images in (**c-e**), especially in (**e**), is not well defined. After multiplying the filtered 3D structure with a 3D shape determined from the EST reconstruction, a clear 3D boundary of the Pt nanoparticle can be obtained (see Fig. 4.10d).

4.4 Results and discussions

After verifying 3D Fourier filtering with a 3D Wiener filter and multislice simulation data, we analysed 3D dislocations of the Pt nanoparticle obtained fromthe experimental tilt series. Figure 4.16 shows grain boundary comparisons between a 2D experimental projection and 2.6-Å-thick internal slices of the reconstructed particle. The experimental projection in the x–y plane suggests that this is a decahedral multiply twinned nanoparticle[41] with flat twin boundaries (Fig. 4.16a and Fig. 4.17). However, a 2.6-Å-thick internal slice in the x–y plane and an enlarged view indicate the existence of atomic steps at the twin boundaries (Fig. 4.16b, c) that are hidden in the projection (Fig. 4.16a). Figure 4.16d and e shows enlarged views of a twin boundary in a 2.6-Å-thick slice above and below the slice of Fig. 4.16b, revealing that the atomic steps vary in consecutive atomic layers. These atomic steps are also independently verified by applying 3D Wiener filtering to the same experimental data (Fig. 4.18). In addition, subgrain boundaries in the 2.6-Å-thick internal slice (Fig. 4.16b) are two lattice spacings wider than those in the projection (Fig. 4.16a). Figure 4.16f shows an enlarged view of a stacking fault in the 2.6-Å-thick internal slice ending at a twin boundary, which agrees well with the classical model for a face-centred-cubic extrinsic stacking fault[1] (inset in Fig. 4.16f).

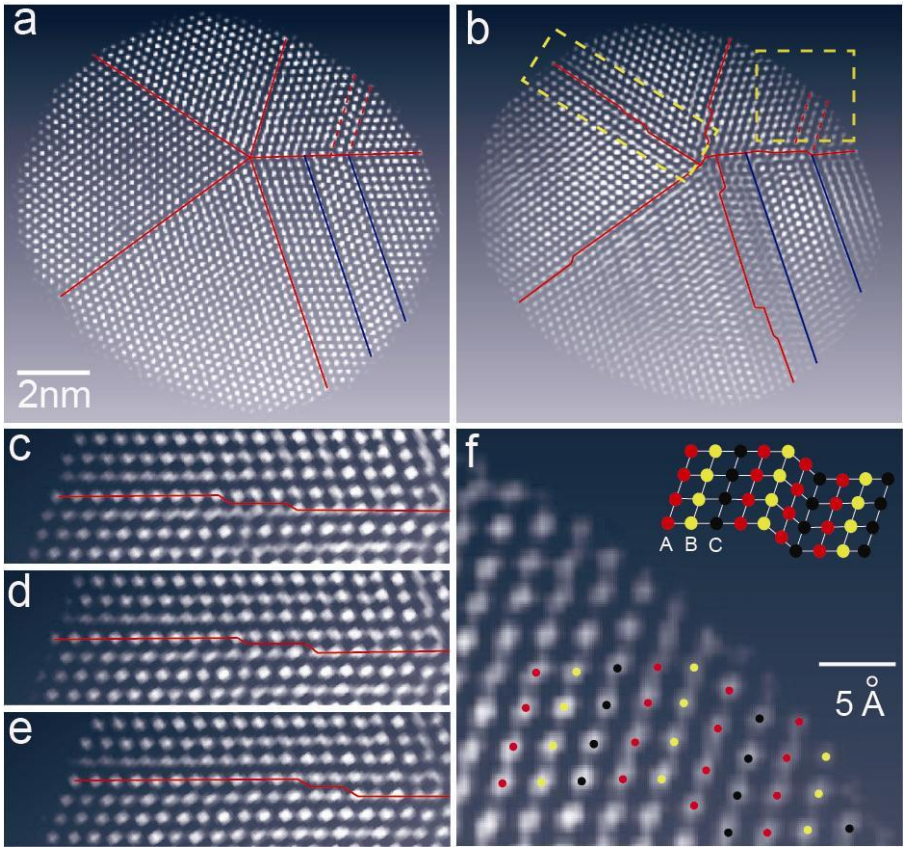

Figure 4.16. Grain boundary comparisons between a 2D experimental projection and several 2.6-Å-thick internal slices of the reconstructed Pt nanoparticle. **a**, Experimental projection in the *x-y* plane suggesting that this is a decahedral multiply twinned nanoparticle and that the twin boundaries (red lines) are flat. Blue lines show two subgrain boundaries. To enhance the image contrast, a 2D Fourier filter was applied to the projection. **b**, A 2.6-Å -thick internal slice indicating the existence of atomic steps at the twin boundaries (red lines). The subgrain boundaries (blue lines) are two lattice spacings wider than those in **a**. **c**, Enlarged view of a twin boundary in **b**. **d** and **e**, a 2.6-Å-thick slice above and below the slice of **c**, revealing that the atomic steps vary in consecutive atomic layers. **f**, Enlarged view of a stacking fault in the 2.6-Å-thick internal slice, which is in good agreement with the classical model for a face-centered-cubic extrinsic stacking fault (inset). These images are displayed with Amira.

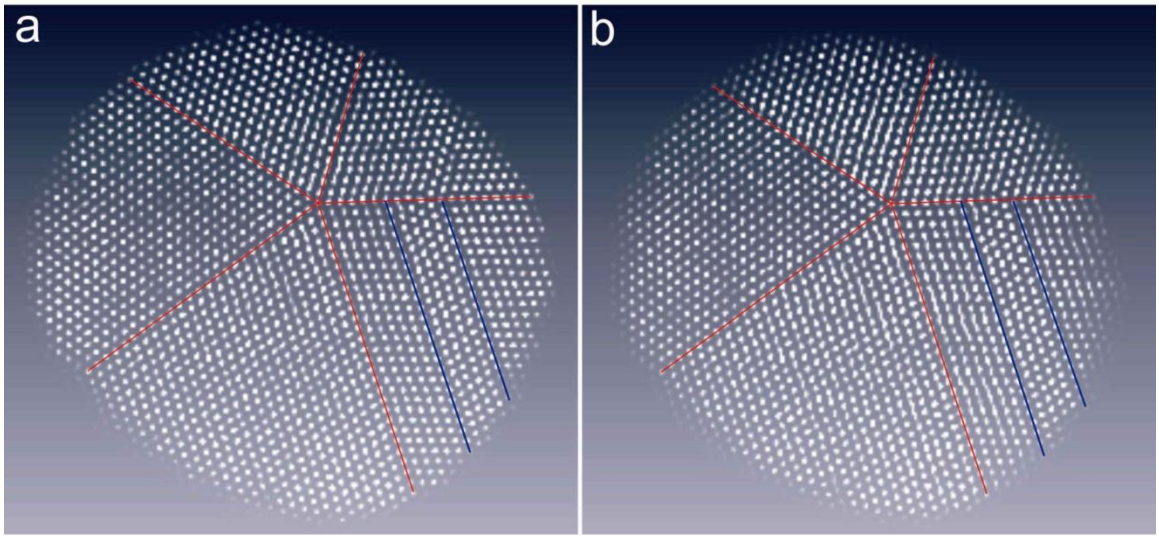

Figure 4.17. Grain boundary comparison between experimental (**a**) and calculated (**b**) projections in the XY plane, in which the twin boundaries (red lines) and subgrain boundaries (blue lines) are consistent. (**a**) is the same as Fig. 2a, and (**b**) was calculated by reprojecting the EST reconstruction to the XY plane. 2D Fourier filtering was applied to the projections to better show the twin and subgrain boundaries. Some of the differences between (**a**) and (**b**) are mainly caused by 2D Fourier filtering, which, according to our numerical simulations, is not as accurate as the 3D case.

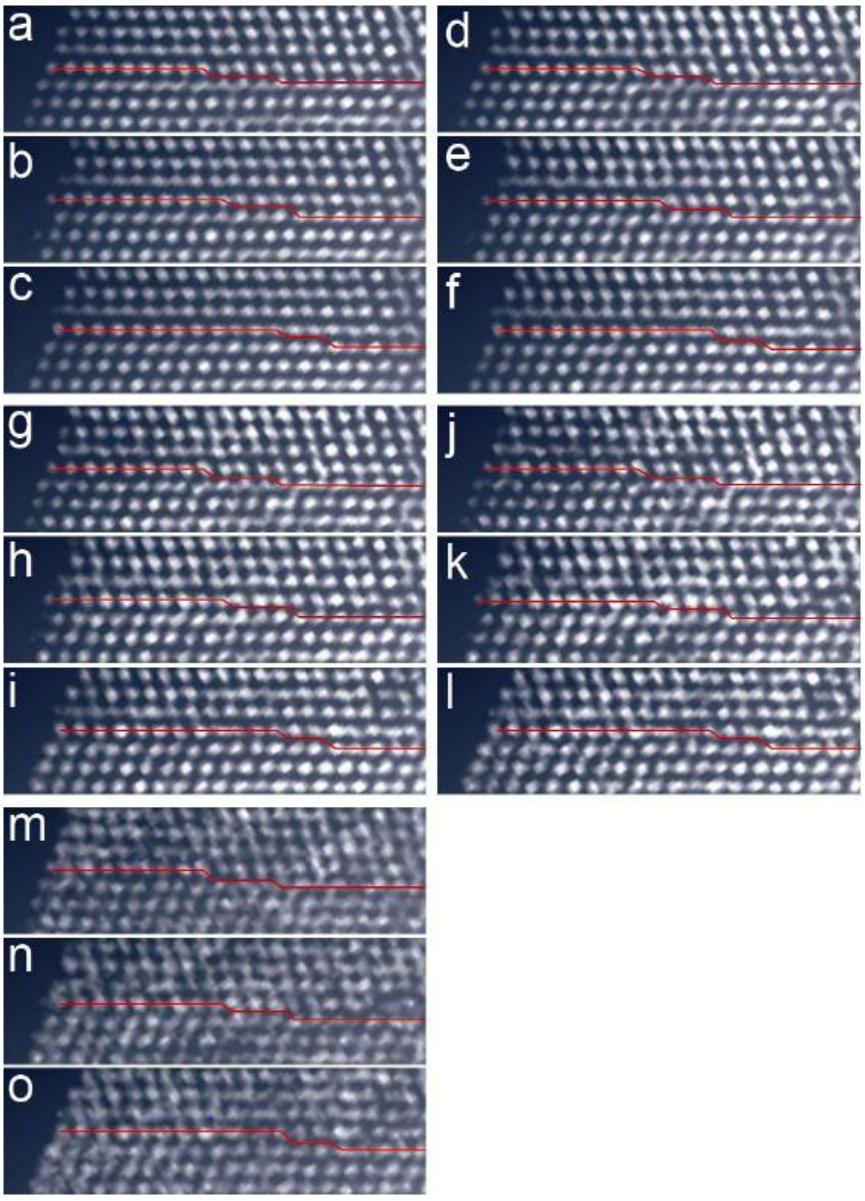

Figure 4.18. **a-c**, Three consecutive 2.6 Å thick slices across a twin boundary after 3D Fourier filtering with a threshold of 10% (i.e. the same as Fig. 4.16c-e). The same three consecutive slices after 3D Fourier filtering with a threshold of 7% (**d-f**),and 3D Wiener filtering with $\lambda = 3$ (**g-i**), $\lambda = 2$ (**j-l**) and $\lambda = 1$ (**m-o**). The atomic steps at the twin boundary (red lines) are consistent in all five cases.

In addition to twin boundaries, subgrain boundaries and stacking faults, we observed the 3D core structure of edge and screw dislocations at atomic resolution in the Pt nanoparticle. Figure 4.19a and b shows a 7.9-Å-thick internal slice of the nanoparticle and an enlarged view of an edge dislocation, where the red dots indicate the atomic positions. By computationally 'sectioning' the 7.9-Å-thick slice, we obtained three consecutive atomic layers, each 2.6Å thick (Fig. 4.19c-e). The three consecutive atomic layers indicate that the dislocation line is in the $[10\bar{1}]$ direction, and the Burgers vector of the edge dislocation was determined to be $\frac{1}{2}[101]$ (Fig. 4.19c). To visualize a screw dislocation, a 5.3-Å-thick slice (two atomic layers) in the $(\bar{1}11)$ plane was selected (Fig. 4.21b) and then tilted to the [011] direction (Fig. 4.20a). Figure 4.20b shows an enlarged view of the slice where the zigzag pattern, a characteristic feature of a screw dislocation, is visible. To better visualize the screw dislocation, we display surface renderings of the enlarged region (Fig. 4.20c), where the atoms indicated by green dots are in the top layer and those indicated by red dots are in the bottom layer. The zigzag pattern is more clearly visualized in the surface renderings, in which the green line connects the atoms in the top layer and the red line connects the atoms in the bottom layer. The Burgers vector of the screw dislocation was determined to be $\frac{1}{2}[01\bar{1}]$, and the width of the screw dislocation was estimated to be ~8.9 Å, which is consistent with the results obtained by combining high-resolution TEM with image simulations for Au and Ir (ref. 42).

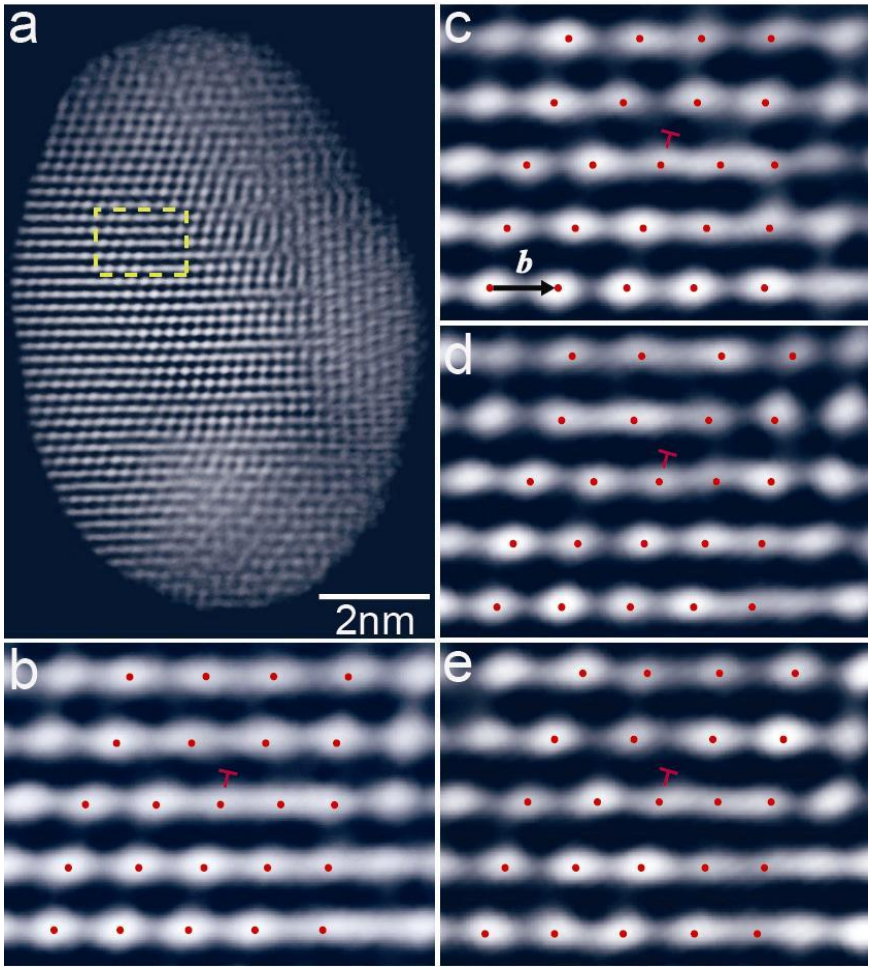

Figure 4.19. Observation of the 3D core structure of an edge dislocation at atomic resolution. **a**, A 7.9-Å-thick internal slice of the nanoparticle. The lattice structure on the left and at the bottom parts of the slice is not well defined, mainly because this decahedral multiply twinned nanoparticle consists of five grains with different orientations. **b**, An enlarged view of an edge dislocation in a where red dots represent the position of the atoms. **c**, **d** and **e**, 2.6-Å-thick atomic layers sectioning through the slice of **b**. The three consecutive atomic layers indicate the dislocation line is in the direction of $[10\bar{1}]$.The Burgers vector (b) of the edge dislocation was determined to be $\frac{1}{2}[101]$.

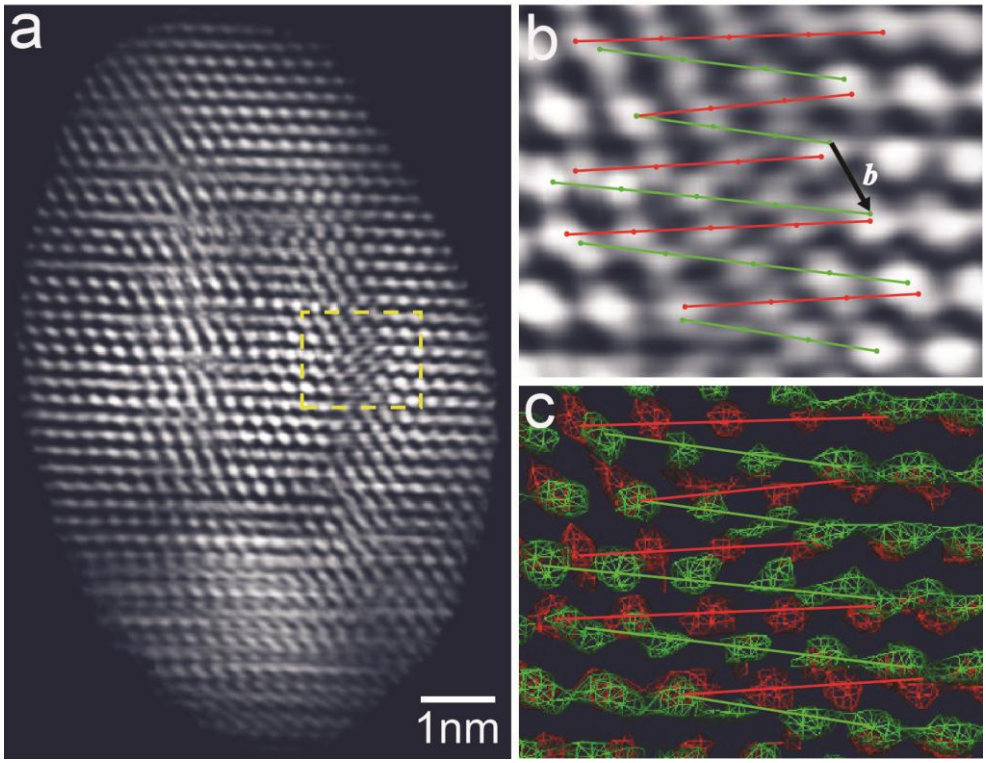

Figure 4.20. Observation of the 3D core structure of a screw dislocation at atomic resolution. **a**, Volume renderings of a 5.3-Å-thick slice (two atomic layers) in the $(\bar{1}11)$ plane (Fig. 4.21b), tilted to the [011] direction to visualize the zigzag pattern, a characteristic feature of a screw dislocation. **b**, Enlarged view of a screw dislocation showing the zigzag pattern. **c**, Surface renderings of the screw dislocation where the atoms represented by green dots are in the top layer and those by red dots are in the bottom layer. The zigzag pattern is more clearly visualized, the Burgers vector (b) of the screw dislocation was determined to be $\frac{1}{2}[01\bar{1}]$, and the width of the screw dislocation was estimated to be ~8.9 Å.

Careful analysis of the position of the screw dislocation inside the Pt nanoparticle suggests that the screw dislocation is associated with atomic steps at a twin boundary (Fig. 4.21). Although it

is often thought that nanoparticles cannot support dislocations, this is not the case for multiply twinned particles such as the decahedral one imaged here. These contain a ~2% angular strain and a disclination; at larger sizes this can in principle be relieved by dislocations[41]. A recent analysis implied that about one-third of this strain is accommodated at the twin boundaries[43], but as a 2D projection method was used in this analysis, it did not provide further insight. Our results strongly suggest that the twin boundaries are not flat and that dislocations associated with atomic steps at the boundaries account for the strain relaxation (Fig. 4.21).

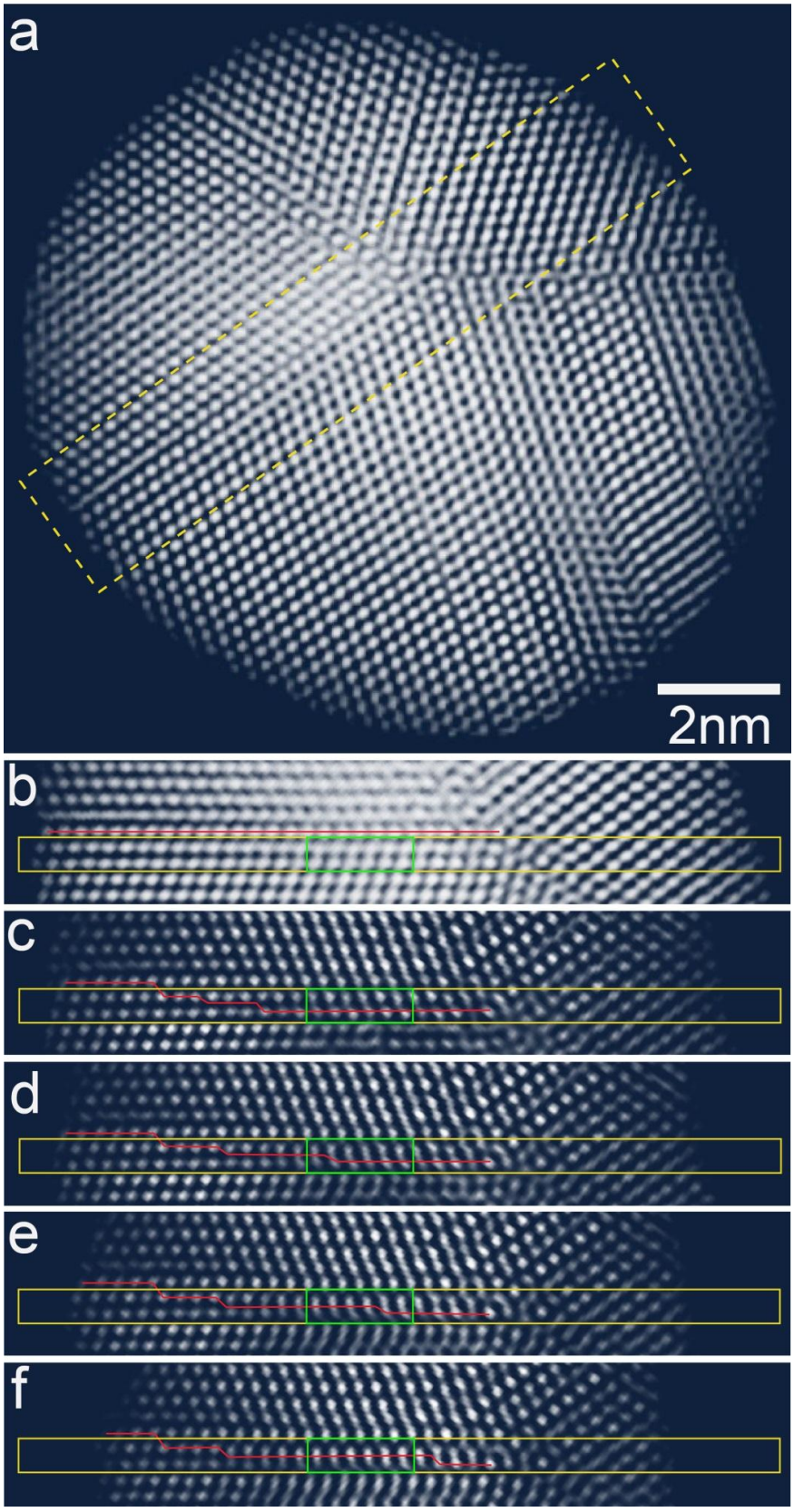
a
2nm
b
c
d
e
f

Figure 4.21. Association of a screw dislocation with atomic steps at a twin boundary. **a**, 3D volume rendering of the reconstructed Pt nanoparticle viewed along the [110] (Z-axis) direction. **b**, Zoomed view of the screw dislocation and twin boundary. The yellow rectangle shows a 5.3 Å thick slice in the $(\bar{1}11)$ plane (left grain) used for generating Fig. 4.20. The green rectangle indicates the location of the screw dislocation in the [110] direction and the twin boundary is labeled with a red line. **c-f**, Four consecutive internal slices each with 2.6 Å thick. The positions of the atoms inside the green rectangles gradually change in (**c-f**) suggesting that the screw dislocation is associated with atomic steps at the twin boundary. The association of the dislocations with the atomic steps at the boundary accounts for the strain relaxation for the multiply-twinned particle. Note that the twin boundary inside the green rectangles is not well defined.

4.5 Conclusion

In this Chapter we report 3D imaging of dislocations in materials at atomic resolution by electron tomography. By applying 3D Fourier filtering together with equal-slope tomographic reconstruction, we observe nearly all the atoms in a multiply twinned platinum nanoparticle. We observed atomic steps at 3D twin boundaries and imaged the 3Dcore structure of edge and screw dislocations at atomic resolution. These dislocations and the atomic steps at the twin boundaries, which appear to be stress-relief mechanisms, are not visible in conventional two-dimensional projections. The ability to image 3D disordered structures such as dislocations at atomic resolution is expected to find applications in materials science, nanoscience, solid-state physics and chemistry.

The significance of the present work is twofold. First, 3D atomic resolution imaging of dislocations allows us to observe new structures that are not visible in conventional 2D projections; this is expected to advance our fundamental understanding of dislocations in materials. Second, although discrete tomography through the use of a priori information has been applied to reconstruct 3D surface morphology of a small crystalline nanoparticle at atomic resolution[44] , EST-based electron tomography in combination with 3D Fourier filtering represents a general method for 3D atomic resolution imaging of the local structure in nanomaterials. Although nanoparticles are used in this study, this method could, in principle, be applied to 3D imaging of thin materials at high resolution; the sample thickness is limited only by dynamical electron scattering.

References

1. Hull, D. & Bacon, D. J. *Introduction to Dislocations* 5th ed. (Butterworth-Heinemann, 2011).
2. Smith, W. F. & Hashemi, J. *Foundations of Materials Science and Engineering* 4th ed. (McGraw-Hill Science, 2005).
3. Nakamura, S. The Roles of Structural Imperfections in InGaN-Based Blue Light-Emitting Diodes and Laser Diodes. *Science* **281**, 956-961 (1998).
4. Hua, G. C. *et al*. Microstructure study of a degraded pseudomorphic separate confinement heterostructure blue-green laser diode. *Appl. Phys. Lett.* **65**, 1331-1333 (1994).
5. Hirsch, P. B., Horne, R. W. & Whelan, M. J. LXVIII. Direct observations of the arrangement and motion of dislocations in aluminium. *Philos. Mag.* **1**, 677-684 (1956).

6. Bollmann, W. Interference Effects in the Electron Microscopy of Thin Crystal Foils. *Phys. Rev*. **103**, 1588–1589 (1956).
7. Menter, J. W. The Direct Study by Electron Microscopy of Crystal Lattices and their Imperfections. *Proc. R. Soc. Lond.* A **236**, 119-135 (1956).
8. Howie, A. & Whelan, M. J. Diffraction Contrast of Electron Microscope Images of Crystal Lattice Defects. III. Results and Experimental Confirmation of the Dynamical Theory of Dislocation Image Contrast. *Proc. R. Soc. Lond. A* **267**, 206-230 (1962).
9. Hirsch, P. B., Cockayne, D. J. H., Spence, J. C. H. & Whelan, M. J. 50 Years of TEM of Dislocations: Past, Present and Future. *Philos. Mag*. **86**, 4519–28 (2006).
10. Spence, J. C. H. *Experimental High-Resolution Electron Microscopy* 3rd ed. (Oxford University Press, New York, 2003).
11. Chisholm, M. F. & Pennycook, S. J. Structural origin of reduced critical currents at $YBa_2Cu_3O_{7-\delta}$ grain boundaries. *Nature* **351**, 47-49 (1991)
12. Ludwig, W. *et al*. Three-dimensional imaging of crystal defects by `topo-tomography'. *J. Appl. Crystallogr*. **34**, 602-607 (2001).
13. Cockayne, D. J. H., Ray, I. L. F. & Whelan, M. J. Investigations of dislocation strain fields using weak beams. *Philos. Mag*. **20**, 1265-1270 (1969).
14. Pennycook, S. J. & Nellist, P. D. *Scanning Transmission Electron Microscopy: Imaging and Analysis* 1st ed. (Springer, 2011).
15. Barnard, J. S., Sharp, J., Tong, J. R. & Midgley, P. A. High-Resolution Three-Dimensional Imaging of Dislocations. *Science* **313**, 319 (2006).

16. Midgley, P. A. & Weyland, M. STEM Tomography. In *Scanning Transmission Electron Microscopy: Imaging and Analysis*. ed. Pennycook, S. J. & Nellist, P. D. pp. 353-392 (Springer, 2011).

17. Kelly, T. F. & Miller, M. K. Atom probe tomography. *Rev. Sci. Instrum.* **78**, 031101 (2007).

18. Scott, M. C. *et al.* Electron tomography at 2.4 Å resolution. *Nature* **483**, 444–447 (2012).

19. Howie, A. Diffraction channelling of fast electrons and positrons in crystals. *Phil. Mag.* **14**, 223-237 (1966).

20. Xin, H. L., Ercius, P., Hughes, K. J., Engstrom, J. R. & Muller, D. A. Three-dimensional imaging of pore structures inside low-κ dielectrics. *Appl. Phys. Lett.* **96**, 223108 (2010).

21. Chen, C.C. et al. Three-dimensional imaging of dislocations in a nanoparticle at atomic resolution. *Nature* **496**, 74–77 (2013).

22. http://www.ndt-ed.org/ EducationResources/ CommunityCollege/Materials/ Structure/ crystal_defects.htm

23. http://eng.sut.ac.th/metal/images/stories/pdf/05_Dislocation_theory.pdf

24. http://chemistry.tutorvista.com/inorganic-chemistry/crystal-defects.html

25. http://www.tf.uni-kiel.de/matwis/amat/def_en/kap_5/backbone/r5_4_1.html

26. Zhu, Y. T., Liao, X. Z. & Wu, X. L. Deformation twinning in nanocrystalline materials. *Progress in Materials Science* **57**, 1-62 (2012).

27. Chiu, C. Y. *et al*. Platinum nanocrystals selectively shaped using facet-specific peptide sequences. *Nature Chem.* **3**, 393-399 (2011).

28. Miao, J., Föster, F. & Levi, O. Equally sloped tomography with oversampling reconstruction. *Phys. Rev. B* **72**, 052103 (2005).

29. Lee, E. *et al*. Radiation dose reduction and image enhancement in biological imaging through equally sloped tomography. *J. Struct. Biol.* **164**, 221–227 (2008).

30. Fahimian, B. P., Mao, Y., Cloetens, P., & Miao, J. Low dose X-ray phase-contrast and absorption CT using equally-sloped tomography. *Phys. Med. Biol.* **55**, 5383-5400 (2010).

31. Zhao, Y. *et al.* High resolution, low dose phase contrast x-ray tomography for 3D diagnosis of human breast cancers. *Proc. Natl. Acad. Sci. USA* **109**, 18290-18294 (2012).

32. Bar Sadan, M. *et al.* Toward atomic-scale bright-field electron tomography for the study of fullerene-like nanostructures. *Nano Lett*. **8**, 891-896 (2008).

33. Bailey, D. H. & Swarztrauber, P. N. The fractional Fourier transform and applications. *SIAM Rev*. **33**, 389–404 (1991)

34. Averbuch, A.,Coifman, R. R.,Donoho, D. L., Israeli,M.&Shkolnisky, Y.Aframework for discrete integral transformations I —the pseudopolar Fourier transform. *SIAM J. Sci. Comput.* **30**, 785–803 (2008).

35. Kirkland, E. J. *Advanced Computing in Electron Microscopy* 2nd ed. (Springer, 2010).

36. Brown, R. G. & Hwang, P. Y. C. *Introduction to Random Signals and Applied Kalman Filtering* 3rd ed. (Wiley, 1996).

37. Saxton, W. O. *Computer Techniques for Image Processing in Electron Microscopy* (Academic, 1978).

38. Hawkes P. W. *Computer Processing of Electron Microscope Images* (Springer, 1980).

39. Möbus, G., Necker, G. & Rühle, M. Adaptive Fourier-filtering technique for quantitative evaluation of high-resolution electron micrographs of interfaces. *Ultramicroscopy* **49**, 46-65 (1993).

40. Marks, L. D. Wiener-filter enhancement of noisy HREM images. *Ultramicroscopy* **62**, 43-52 (1996).

41. Howie, A. & Marks, L. D. Elastic strains and the energy balance for multiply twinned particles, *Philos. Mag.* A **49**, 95-109 (1984).

42. Balk, T. J. & Hemker, K. J. High resolution transmission electron microscopy of dislocation core dissociations in gold and iridium. *Philos. Mag.* A **81**, 1507-1531 (2001).

43. Johnson, C. L. J. *et al.* Effects of elastic anisotropy on strain distributions in decahedral gold nanoparticles. *Nature Materials* **7**, 120-124 (2008).

44. Van Aert, S., Batenburg, K. J., Rossell, M. D., Erni, R. & Van Tendeloo, G. Three-dimensional atomic imaging of crystalline nanoparticles. *Nature* **470**, 374–377 (2011).

CHAPTER 5

Towards Three-Dimensional Structural Determination of Amorphous Materials at Atomic Resolution by Electron Tomography

Disordered materials such as glasses are ubiquitous in our daily life. Although the history of glassmaking can be traced back to 3,500 BC in Mesopotamia, the 3D atomic structure of glasses and other disordered materials has thus far defied any direct experimental determination due to its lack of long-range translational and orientational order. Nobel Laureate Philip Anderson wrote in *Science* in 1995, "The deepest and most interesting unsolved problem in solid state theory is probably the theory of the nature of glass and the glass transition." This theoretical difficulty stems from the lack of experimental techniques that directly probe the three-dimensional (3D) atomic arrangement in glasses. In addition, the 3D atomic structures of amorphous materials, such as glasses, are key to understanding the origin of glass transitions and associated phenomena[1]. Previous studies of amorphous structures have relied on conventional diffraction, scattering, Raman, and nuclear magnetic resonance spectroscopy, coupled with computational methods, such as molecular-dynamics and *ab initio* calculations[2–9]. Recently, atomic resolution transmission electron microscopy has been used to directly image a two-dimensional (2D) silica glass supported on graphene[10]. However, presently, there are no experimental methods available to directly image the atomic structure of amorphous materials in three dimensions. A very promising technique to overcome this barrier is electron tomography[11–17]. The combination of annular dark-field (ADF) scanning transmission electron microscopy[18]

(STEM) and a novel data acquisition and image reconstruction method known as equally sloped tomography[19–27](EST) has recently achieved a 3D reconstruction of a Au nanoparticle at 2.4-Å resolution from a tilt series of 69 projections[16], as shown in Chapter 3. The center of mass (c.m.) approach has been used to align the projections of the tilt series at atomic precision[16]. EST has been shown to partially recover missing information in the reconstruction better than other tomographic reconstruction algorithms[21]. This missing information arises from the need to limit the number of total projections due to radiation damage as well as the missing wedge problem (i.e., specimens cannot usually be tilted beyond $\pm 79°$). More recently, electron tomography has been applied to image nearly all the atoms in a Pt nanoparticle, and the atomic core structure of edge and screw dislocations in the nanoparticle have been observed in three dimensions[17], as shown in Chapter 4. Here, we make another significant advance in electron tomography and demonstrate, through numerical experiments, a general method for 3D structural determination of amorphous materials at atomic resolution. By combining multislice STEM simulations[28] with EST[16,17,19–27], we have shown the feasibility of determining the 3D atomic structure of a ($24.7 \times 24.7 \times 24.7$) – $Å^3$ amorphous silica particle.

5.1 Numerical Simulations

5.1.1 Molecular-dynamic simulations

The atomic structure of the amorphous silica particle was generated by molecular-dynamics simulations. Presently, there are several methods available for the simulation of amorphous structures, such as reverse Monte Carlo[5] and molecular dynamics[6]. Here a simulated melt and quench approach was used to generate an amorphous silica structure with a cooling rate of 2.5

K/ps. A set of partial charge Buckingham potentials was employed in the molecular-dynamics simulations[7]. The amorphous silica structure obtained by this approach has few coordination defects[29] and is in good agreement with neutron-diffraction data[30]. The glass structure, consisting of 334 Si atoms and 668 O atoms (Fig. 5.1),was used to calculate a tomographic tilt series by multislice STEM simulations[28].

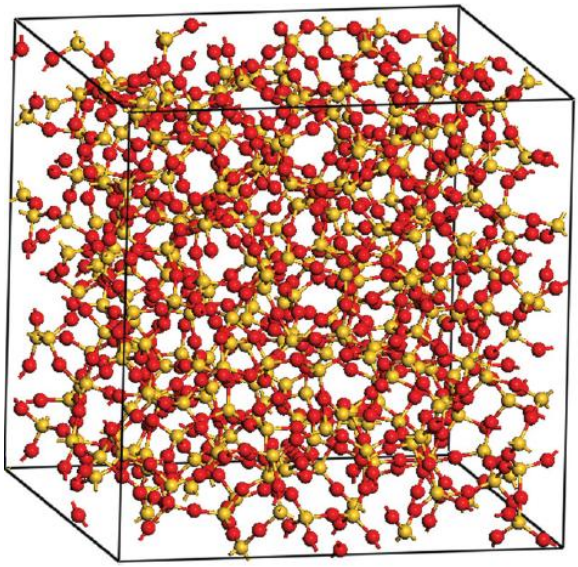

Figure 5.1. Three-dimensional atomic structure of an amorphous silica particle generated by molecular-dynamics simulations. The simulation cell is $24.7 \times 24.7 \times 24.7$ Å^3, and the total number of atoms is 1002 where the yellow balls represent the Si atoms and the red balls represent the O atoms. No coordination defects are observed in the structure.

5.1.2 Multislice simulations

An aberration-corrected STEM with an electron energy of 80 keV was employed in the multislice STEM calculation (spherical aberration: 0; fifth order spherical aberration: 2.5 mm; probe FWHM: 0.8 Å; pixel size: 0.5 Å). In our multislice simulations, we first determined the optimal illumination semiangle and detector inner and outer angles by calculating a number of tilt series. Each tilt series consists of 55 projections with a tilt range of $\pm 72.6^{\circ}$ and equal slope tilt increments between projections[16, 17, 19–27]. To simulate potential errors in experimental conditions, the ideal EST tilt angles were continuously shifted by 0° to 0.5° throughout the process of the tilt series which was randomly shifted in the image plane. Each tilt series was quantified by R_{tilt}, defined as

$$R_{tilt}^{\theta} = \frac{\sum \left\| P_l^{\theta}(x,y) \right| - \left| P_m^{\theta}(x,y) \right\|}{\sum \left| P_l^{\theta}(x,y) \right|} \qquad (Eq.\ 5.1)$$

where $P_l^{\theta}(x,y)$ represents the linear projection of the Coulomb potential of the glass particle and $P_m^{\theta}(x,y)$ the multislice simulated projection at tilt angle θ. By averaging R_{tilt}^{θ} for 55 projections, we calculated R_{tilt} for each tilt series. Table 5.1 shows R_{tilt} as a function of the illumination semi-angle and detector inner and outer angles. R_{tilt} is smallest when the illumination semi-angle is 27 mrad and the detector inner and outer angles are 80 and 400 mrad, respectively.

Semiangle	Detector inner and outer angles (mrad)			
(mrad)	50–250	60–300	70–350	80–400
25	0.263	0.256	0.253	0.252
26	0.260	0.253	0.250	0.249
27	0.259	0.252	0.249	0.248
28	0.260	0.253	0.250	0.249
29	0.264	0.256	0.252	0.251
30	0.269	0.260	0.256	0.255
31	0.276	0.267	0.262	0.260
32	0.289	0.276	0.270	0.268
33	0.299	0.288	0.280	0.278
34	0.316	0.304	0.294	0.291
35	0.335	0.323	0.312	0.308

Table 5.1. R_{tilt} as a function of the illumination semi-angle and the detector inner and outer angles. R_{tilt} is smallest when the illumination semi-angle is 27 mrad and the detector inner and outer angles are 80 and 400 mrad.

Poisson noise was added to the optimal tilt series with a total electron dose of $2.2\text{x}10^6$, $1.43\text{x}10^6$, $5.5\text{x}10^5$ and $3.0\text{x}10^5$ e/Å^2, respectively. An R_{noise} was used to quantify the noise level for each tilt series, defined as

$$R_{noise}^{\theta} = \frac{\sum_{x,y} \left| P_{noise}^{\theta}(x,y) - P_{m}^{\theta}(x,y) \right|}{\sum_{x,y} P_{m}^{\theta}(x,y)} \qquad (Eq.\ 5.2)$$

where $P_{noise}^{\theta}(x, y)$ is the projection calculated from multislice STEM simulations at angle θ with Poisson noise added. By averaging R_{noise}^{θ} for 55 projections, we obtained R_{noise} for each tilt series. With the dose level of 2.2×10^{6}, 1.43×10^{6}, 5.5×10^{5} and 3.0×10^{5} e/Å^2, R_{noise} was calculated to be 10%, 12%, 20% and 25%, respectively. Figure 1a shows a representative multislice projection at $0\,°$ with R_{noise} = 25%. To examine the experimental feasibility, we acquired a $0\,°$ projection of a SiO_2 structure by using TEAM 1, an aberration-corrected STEM at the National Center of Electron Microscopy, under similar conditions as the multislice STEM simulations. Figure 5.2b shows the experimental projection of the SiO2 structure. Figure 5.2c and d show the 2D Fourier modulus of Figs. 5.2a and b, respectively. The horizontal and vertical line scans across the origin of the 2D Fourier modulus (Figs. 2e and f) indicate that the overall features of the two projections are consistent.

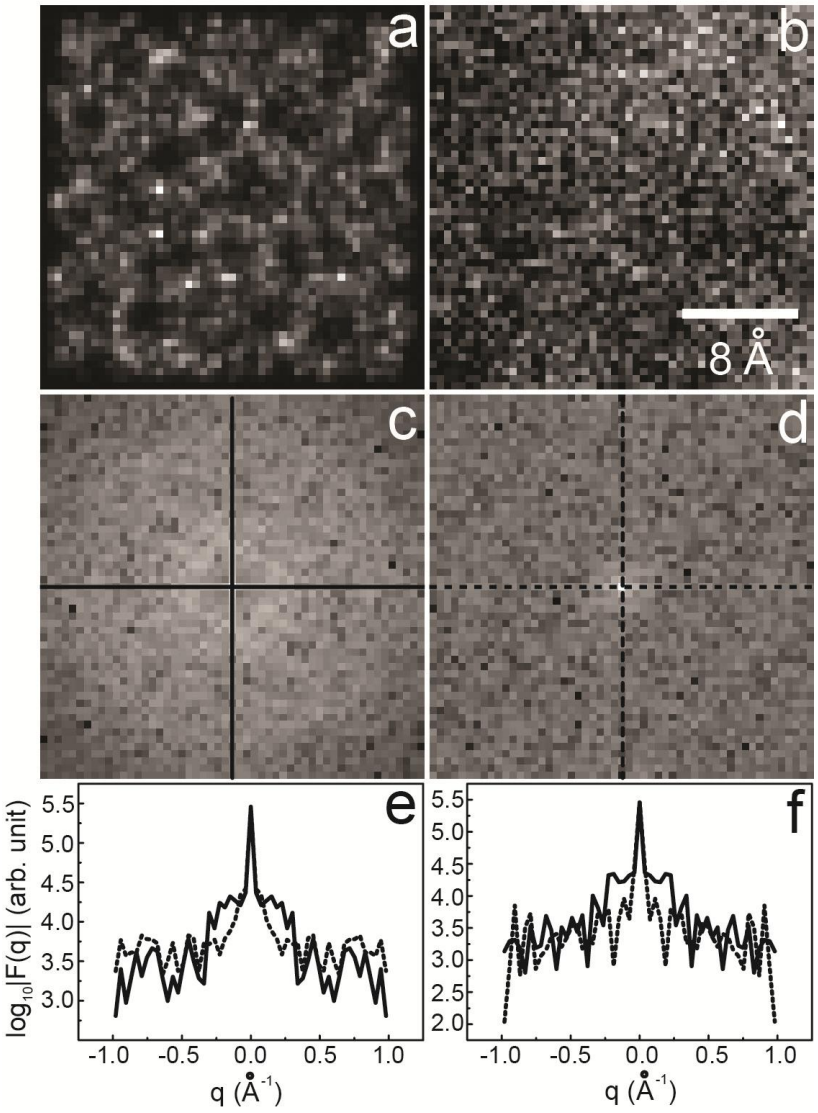

Figure 5.2. **a**, Representative multislice STEM projection at 0 °with R_{noise} = 25%. **b**, Experimental projection of a SiO_2 structure, acquired by an aberration-corrected STEM under the similar conditions as the multislice STEM simulations. **c**, The 2D Fourier modulus of **a**. **d**, The 2D Fourier modulus of **b**. **e**, Horizontal line scans across the origin of the 2D Fourier modulus where the spatial frequency (q) is defined as the inverse of the spatial resolution. **f**, Vertical line scans across the origin of the 2D Fourier modulus. The overall features of the two projections are consistent, and the differences between the two projections are partially because the experimental SiO_2 structure is thicker than the simulation.

5.1.3 Projection alignment and EST reconstruction

In order to achieve an atomic resolution reconstruction, the projections of the tilt series have to be aligned along both the *X* and the *Y* axes with atomic precision where the *Y* axis is the rotation axis and the *Z* axis is the beam direction. To align the tilt series along the *Y* axis, we projected each projection to the *Y* axis to obtain a one-dimensional (1D) curve. By using the 1D curve of the 0◦ projection as a reference, we aligned the remaining 54 1D curves to the reference based on cross correlation. To align the tilt series along the *X* axis, we used the c.m. method mentioned in Chapter 3[16, 17]. First, each projection was projected to the *X* axis to obtain 55 1D curves. We then calculated the center of mass ($X_{\text{c.m.}}$) for each 1D curve and set $X_{\text{c.m}}$ as the origin of the 1D curve. By repeating the procedure for all 1D curves, we aligned the projections along the *X* axis. The accuracy of the c.m. alignment method is a fraction of a pixel where the pixel size is 0.5 Å.

After aligning the tilt series, the 3D structure of the glass particle was reconstructed using the EST algorithm[16, 17, 19–27]. EST first converted the 55 projections to Fourier slices by the fractional Fourier transform[31]. The algorithm then iterated back and forth between real and reciprocal spaces through the use of the pseudopolar fast Fourier transform[32]. In real space, the values outside an estimated loose support (i.e., a rectangular box larger than the particle) and any negative values inside the support were set to zero. In reciprocal space, the corresponding 55 Fourier slices were replaced with the known ones, and the remaining slices were kept unchanged. The convergence of the algorithm was monitored by an error metric, defined as the difference between the 55 known and the calculated Fourier slices. After 200 iterations, the error metric did not improve any further, and a 3D image was obtained. A tighter 3D support was determined from the image. Using the tighter support, we ran the EST algorithm for 200 additional iterations

and obtained a final 3D reconstruction. We repeated the same reconstruction procedure for all four tilt series with different noise levels. Compared to phase retrieval in coherent diffraction imaging[33, 34], the EST algorithm is designed to recover the missing information and, thus, converges more quickly to a final solution.

5.1.4 Atom tracing

To locate the Si and O atoms in the EST reconstructions, we implemented an atomic model refinement method based on the Collaborative Computational Project Number 4 (CCP4). CCP4 was first established in 1979 and has assembled a comprehensive collection of programs for phase determination and model refinement in macromolecular crystallography[35]. Here we used a CCP4 program called PEAKMAX to trace Si and O atoms in the EST reconstructions. Three constraints have been used in the atom tracing procedure: (i) The voxels with atoms should have larger values than those without atoms, (ii) the voxels with Si atoms should have larger values than those with O atoms, and (iii) each atom has a finite size. After searching for peaks in each 3D reconstruction, PEAKMAX listed the peak positions and peak intensity in descending order. Figure 5.3 shows the peak intensity (σ) as a function of the number of peaks (atoms) for the reconstructions with different noise levels where σ represents the peak intensity in PEAKMAX. A threshold peak intensity is observed, which is due to the image contrast difference between Si and O atoms. In high-angle ADF (HAADF)-STEM, the diffraction and phase contrast effects are significantly reduced, and the image contrast of atoms is roughly proportional to $Z1.8$ where Z is the atomic number[11, 13, 18, 36]. The peak intensity difference between Si and O atoms is obvious with R_{noise} = 10% (Fig. 5.3a) and remains distinguishable with R_{noise} = 12%, 20%, and 25% (Figs.

5.3b–d). These results indicate that Si atoms are above the threshold peak intensity and the O atoms are below the threshold. The number of Si and O atoms traced is 334 and 668, respectively, which are in good agreement with the model.

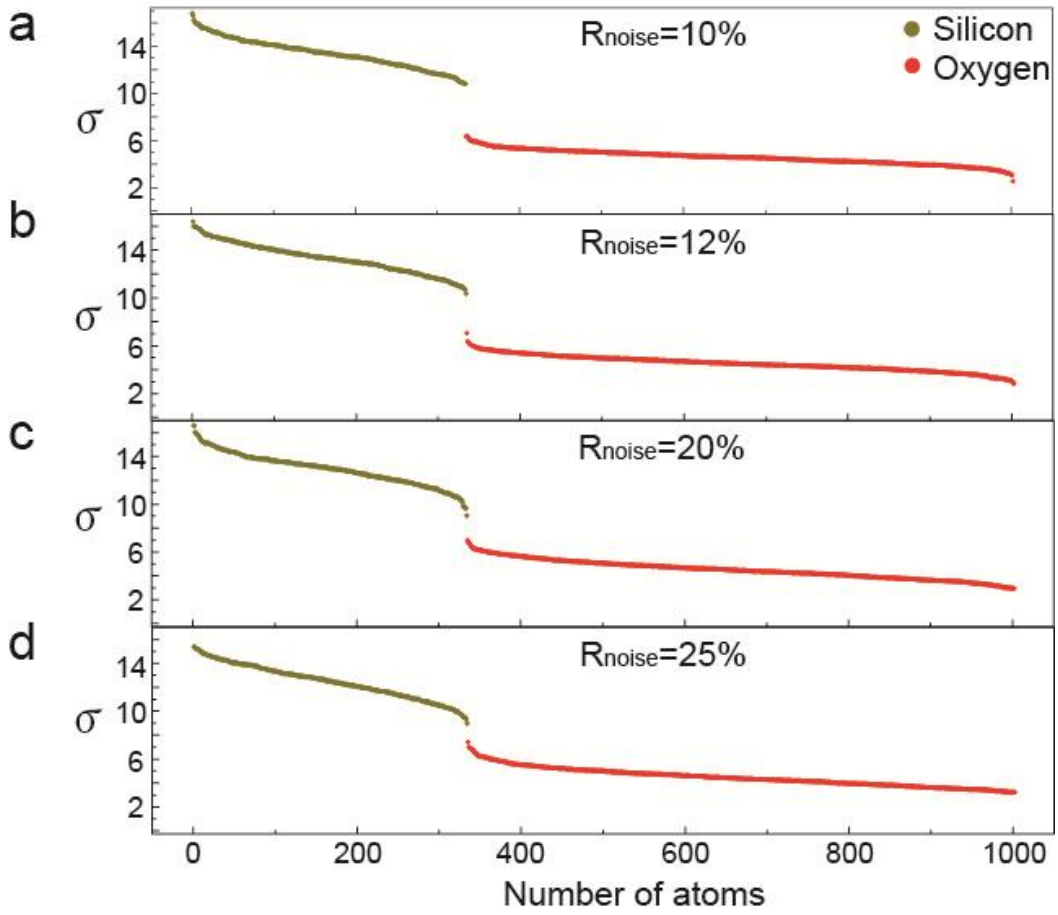

Figure 5.3. Peak intensity (σ) as a function of the number of peaks (atoms) for the reconstructions with a noise level of **a**, R_{noise} = 10%, **b**, 12%, **c**, 20%, and **d** 25%, where σ represents the peak intensity in PEAKMAX. A threshold peak intensity is observed in the curves, which is due to the image contrast difference between Si and O atoms.

5.2 Results and discussions

After tracing the atoms in the EST reconstructions, we examined the 3D atomic structure of the glass particle. Figures 5.4a–c show three 3-Å-thick central slices in the *YZ*, *XZ*, and *XY* planes, respectively, of the original glass particle in which the yellow spheres represent the Si atoms and the red spheres represent the O atoms (hardball model). The corresponding three slices of the EST reconstruction with R_{noise} = 10% are shown in Figs. 5.4d–f where the traced atomic positions are in excellent agreement with those in the original structure. With the increase in the noise level, the 3D atomic structure of the reconstruction is slightly degraded. Figures 5.4g–i show the corresponding three slices of the reconstruction with R_{noise} = 25%. Whereas the positions of all Si atoms and most O atoms are correctly located, several O atoms deviate from their correct positions as indicated by arrows in Figs. 5.4g–i.

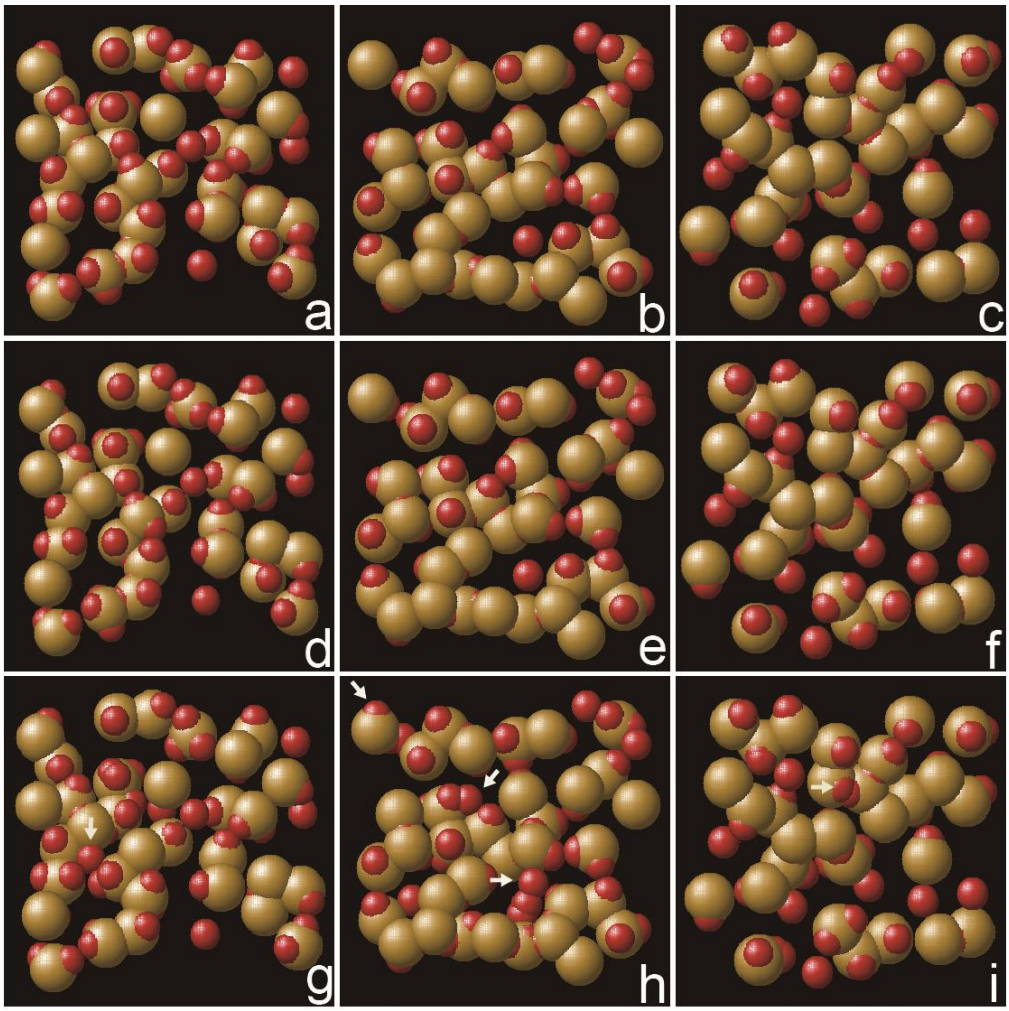

Figure 5.4. **a**–**c** Three 3-Å thick central slices in the *YZ*, *XZ*, and *XY* planes of the original glass particle in which the yellow spheres represent the Si atoms and the red spheres represent the O atoms (hardball model). **d**–**f** Corresponding slices of the EST reconstruction with R_{noise} = 10% where the atomic positions are in excellent agreement with those in the original structure. **g**–**i** Corresponding slices of the reconstruction with R_{noise} = 25%. While the positions of all Si atoms and most O atoms are correctly located, several O atoms are misplaced as indicated by arrows.

To quantify the traced atoms, we calculated the deviation of the atomic positions relative to the original glass structure model. Figure 5.5 shows the deviation as a function of the traced atoms for four different noise levels. With R_{noise} = 10%, all Si and O atoms are correctly located from the EST reconstruction. In this case, the deviation of all atomic positions is within the resolution of the reconstruction [Fig. 5.5a]. When R_{noise} is increased to 12%, one O atom deviates about 2.2 Å from its correct position [Fig. 5.5b]. With R_{noise} = 20%, 12 O atoms are misplaced, and the deviations of all other atoms are within 0.6 Å [Fig. 5.5c].With R_{noise} = 25%, 38 O atoms deviate from their correct positions with an average deviation of 2.5 Å, and the positions of all other atoms are correctly located [Fig. 5.5d]. These results suggest that, with an electron dose above 1.43×10^6 $e/Å^2$ per tilt series (approximately 14-μs dwell time for an image with 70 pA of probe beam current), the positions of all Si and O atoms of the glass particle can be accurately located from the EST reconstruction. Finally, we want to point out that our numerical experiments did not take into account the contribution from a support film, which would reduce the signal-to-noise ratio of the projections especially at high angles. We expect to solve this problem by making needle-shaped SiO_2 samples and avoiding the use of a support film.

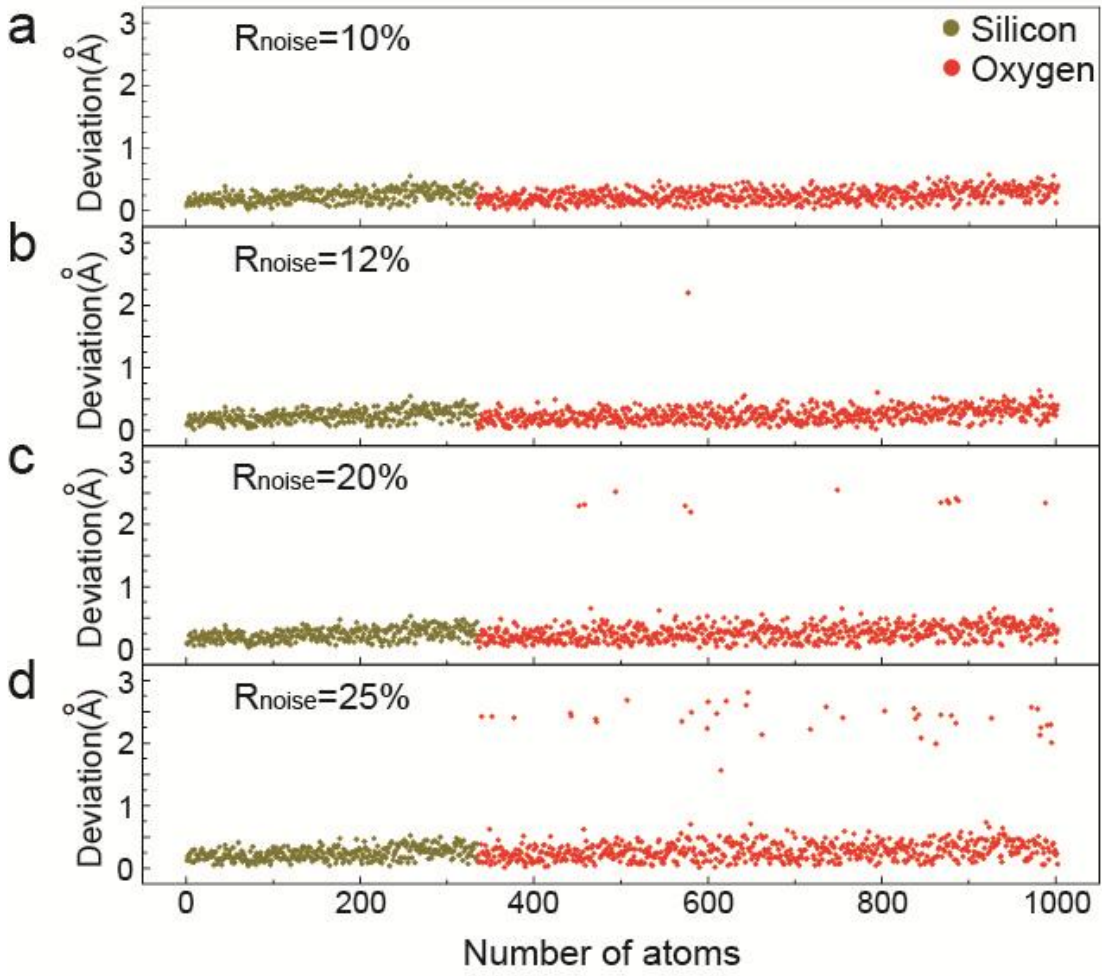

Figure 5.5. Deviation of the atomic positions as a function of the traced atoms for the four different noise levels. **a**, The positions of all Si and O atoms are correctly located from the EST reconstruction with R_{noise} = 10%. **b**, One O atom is misplaced with R_{noise} = 12%. **c**, Twelve O atoms are misplaced, and the positions of all other atoms are correctly identified with R_{noise} =20%. **d**, Thirty-eight O atoms are misplaced, and the positions of all other atoms are correctly located with R_{noise} = 25%.

5.3 Conclusions

In conclusion, by using multislice STEM simulations[28], we calculated a tomographic tilt series of 55 projections from a $(24.7 \times 24.7 \times 24.7) - Å^3$ glass particle, consisting of 334 Si and 668 O atoms. After adding different levels of Poisson noise to the projections, we aligned the tilt series with the c.m. method[16, 17] and performed tomographic reconstructions with the EST algorithm[16, 17, 19–27]. The atomic positions in the reconstructed glass particle were identified by PEAKMAX, a program originally developed for macromolecular crystallography. We found that, with a low noise level (R_{noise} =10%), the positions of all 1002 Si and O atoms can be correctly located from the EST reconstruction. With an increase in the noise level (R_{noise} = 12%, 20%, and 25%), all the Si atoms and most of the O atoms can be accurately traced, whereas, several O atoms deviate from their correct positions. This study demonstrates the feasibility of determining the 3D atomic structure of amorphous materials through the combination of aberration-corrected HAADF-STEM and the EST method. To confirm our numerical simulations, we have acquired an experimental projection from a SiO_2 structure with an aberration-corrected STEM under similar conditions as the multislice simulations. The overall features of the experimental projection agree with the multislice STEM simulation. We expect that the development of this general method will find applications across several disciplines in the physical sciences.

Reference

1. Debenedetti, P. G. & Stillinger, F. H. Supercooled liquids and the glass transition. *Nature* **410**, 259-267 (2001).

2. Zachariasen, W. H. The atomic arrangement in glass. *J. Am. Chem. Soc.* **54**, 3841-3851 (1932).
3. Elliott, S. R. Medium-range structural order in covalent amorphous solids. *Nature* **354**, 445-452 (1991).
4. Klug, H. P. & Alexander, L. E. *X-Ray Diffraction Procedures: For Polycrystalline and Amorphous Materials* (John Wiley & Sons, Inc., 1974).
5. McGreevya, R. L. & Pusztaib, L. A new technique for the determination of disordered structures. *Mol. Simul.* **1**, 359-367 (1988).
6. Kresse, G. & Hafner, J. Ab initio molecular-dynamics simulation of the liquid-metal–amorphous-semiconductor transition in germanium. *Phys. Rev. B* **49**, 14251 (1994).
7. Du, J. & Corrales, L. R. Compositional dependence of the first sharp diffraction peaks in alkali silicate glasses: A molecular dynamics study. *J. Non-Cryst. Solids* **352**, 3255-3269 (2006).
8. Hwang, J. *et al.* Nanoscale structure and structural relaxation in $Zr_{50}Cu_{45}Al_5$ bulk metallic glass. *Phys. Rev. Lett.* **108**, 195505 (2012).
9. Treacy, M. M. J. & Borisenko, K. B. The local structure of amorphous silicon. *Science* **335**, 950-953 (2012).
10. Huang, P. Y. *et al.* Direct imaging of a two-dimensional silica glass on graphene. *Nano Lett.* **12**, 1081-1086 (2012).
11. Midgley, P. A. & Weyland, M. 3D electron microscopy in the physical sciences: the development of Z-contrast and EFTEM tomography. *Ultramicroscopy* **96**, 413-431 (2003).

12. Van Dyck, D., Van Aert, S., den Dekker, A. J. & van den Bos, A. Is atomic resolution transmission electron microscopy able to resolve and refine amorphous structures? *Ultramicroscopy* **98**, 27-42 (2003).
13. Barnard, J. S., Sharp, J., Tong, J. R. & Midgley, P. A. High-resolution three-dimensional imaging of dislocations. *Science* **313**, 319 (2006).
14. Sadan, M. B. *et al.* Toward atomic-scale bright-field electron tomography for the study of fullerene-like nanostructures. *Nano Lett.* **8**, 891-896 (2008).
15. Xin, H. L., Ercius, P., Hughes, K. J., Engstrom, J. R. & Muller, D. A. Three-dimensional imaging of pore structures inside low-κ dielectrics. *Appl. Phys. Lett.* **96**, 223108 (2010).
16. Scott, C. M. *et al.* Electron tomography at 2.4-ångström. *Nature* **483**, 444-447 (2012).
17. Chen, C. C. *et al.* Three-dimensional imaging of dislocations in a nanoparticle at atomic resolution. *Nature* **496**, 74-77 (2013).
18. Pennycook, S. J. & Nellist, P. D. *Scanning Transmission Electron Microscopy: Imaging and Analysis* (Springer, New York, 2011).
19. Miao, J., Förster, F. & Levi, O. Equally sloped tomography with oversampling reconstruction. *Phys. Rev. B.* **72**, 052103 (2005).
20. Miao, J. *et al.* Three-dimensional GaN-Ga_2O_3 core shell structure revealed by X-ray diffraction microscopy. *Phys. Rev. Lett.* **97**, 215503 (2006).
21. Lee, E. *et al.* Radiation dose reduction and image enhancement in biological imaging through equally sloped tomography. *J. Struct. Biol.* **164**, 221-227 (2008).
22. Fahimian, B. P., Mao, Y., Cloetens, P. & Miao, J. Low dose X-ray phase-contrast and absorption CT using equally-sloped tomograph. *Phys. Med. Biol.* **55**, 5383-5400 (2010).

23. Mao, Y., Fahimian, B. P., Osher, S. J. & Miao, J. Development and optimization of regularized tomographic reconstruction algorithms utilizing equally-sloped tomography. *IEEE Trans. Image Processing* **19**, 1259-1268 (2010).
24. Jiang, H. *et al.* Quantitative 3D imaging of whole, unstained cells by using X-ray diffraction microscopy. *Proc. Natl Acad. Sci. USA* **107**, 11234–11239 (2010).
25. Zhao, Y. *et al.* High-resolution, low-dose phase contrast X-ray tomography for 3D diagnosis of human breast cancers. *Proc. Natl. Acad. Sci. USA* **109**, 18290-18294 (2012).
26. Jiang, H. *et al.* Three-dimensional coherent X-ray diffraction imaging of molten iron in mantle olivine at nanoscale resolution. *Phys. Rev. Lett.* **110**, 205501 (2013).
27. The MATLAB source code and a user-friendly software package for EST are freely available at www.physics.ucla.edu/research/imaging/EST. For more detailed information about EST, please refer to Refs. 16 and 17.
28. Kirkland, E. J. *Advanced Computing in Electron Microscopy* (Springer, New York, 2010).
29. Du, J. & Cormack, A. N. Molecular Dynamics Simulation of the Structure and Hydroxylation of Silica Glass Surface. *J. Am Ceram. Soc.* **88**, 2532-2539 (2005).
30. Du, J. & Corrales, L. R. The first sharp diffraction peaks in silicate glasses: structure and scattering length dependence. *Phys. Rev. B* **72**, 092201 (2005).
31. Bailey, D. H. & Swarztrauber, P. N. The fractional Fourier Transform and applications. *SIAM Rev.* **33**, 389-404 (1991).
32. Averbuch, A. *et al.* A framework for discrete integral transformations II—the 2d discrete radon transform. *SIAM J. Sci. Comput.* **30**, 785-803 (2008).

33. Miao, J., Charalambous, P., Kirz, J. & Sayre, D. Extending the methodology of X-ray crystallography to allow imaging of micrometre-sized non-crystalline specimens. *Nature* **400**, 342-344 (1999).

34. Miao, J., Sandberg, R. L. & Song, C. Coherent Diffraction Imaging with X-rays (invited review). *IEEE J. Sel. Top. Quantum Electron.* **18**, 399-410 (2012).

35. http://www.ccp4.ac.uk/.

36. LeBeau, J. M., Findlay, S. D., Allen, L. J. & Stemmer, S. Quantitative atomic resolution Scanning Transmission Electron Microscopy. *Phys. Rev. Lett.* **100**, 206101 (2008).